This is to certify that the

dissertation entitled

THE ELECTROMAGNETIC EXCITATION OF ^{6}HE AND
NEUTRON CROSS-TALK IN A MULTIPLE-DETECTOR SYSTEM

presented by

Jing Wang

has been accepted towards fulfillment
of the requirements for

Ph.D degree in Physics

Aaron Galonsky
Major professor

Date 1-20-99

THE ELECTROMAGNETIC EXCITATION OF ^{6}HE AND NEUTRON CROSS-TALK IN A MULTIPLE-DETECTOR SYSTEM

By

Jing Wang

A DISSERTATION

Submitted to
Michigan State University
in partial fulfillment of the requirements
for the degree of

DOCTOR OF PHILOSOPHY

Department of Physics and Astronomy

1999

Abstract

Part I: The Electromagnetic Excitation of ^{6}He

by

Jing Wang

In the past, ^{11}Li was the focus of physicists who were fascinated by its halo structure formed by the two valence neutrons extending far from the nuclear core. Even after intensive studies of ^{11}Li, it remained unclear whether some properties found in the ^{11}Li nucleus exist in other weakly bound nuclei near the neutron dripline. To further study neutron halo nuclei, a kinematically complete measurement of coulomb dissociation of ^{6}He was performed. In the experiment, a 25 MeV/u ^{6}He beam was delivered to strike six targets—U, Pb, Sn, Cu, Al and C. The momenta of the fragments were measured for the ^{6}He dissociation in the six targets.

The 2-n removal cross sections for the six targets were determined. The coulomb part of the cross sections was extracted using a linear extrapolation and a fitting model. We found, for example, the coulomb dissociation cross section for U accounts for more than half of the total 2-n removal cross section. The measured width of the ^{4}He parallel momentum distribution (σ = 40.2 $\pm$ 2.3 MeV/c) corresponds to a rms radius of 2.95 $\pm$ 0.17 fm for the ^{6}He nucleus. A target dependence of the momentum spread was observed in both neutron and ^{4}He parallel momentum distributions. From the 2n-^{4}He coincidence data, the ^{6}He decay energy spectra were constructed for the six targets. Based on the

decay energy spectrum for the U target, the dipole strength function $\frac{dB(E1)}{dE}$ was determined. The strength function with a Breit-Wigner shape peaks at E_d = 1.9 MeV with a width Γ = 1.5 MeV, which resembles a soft dipole resonance. However, post-breakup acceleration was found in the high-Z targets, which does not support the soft dipole resonance model. The data also suggest that there is little correlation between the halo neutrons in ^{6}He, and a sequential decay mechanism may come to dominate the ^{6}He breakup in light targets.

Part II: Neutron Cross-talk in a Multiple-detector System

by

Jing Wang

Two 2m × 2m neutron "walls" were built for experiments with two neutrons in the final state. Each wall consists of 25 rectangular cells filled with NE-213 liquid scintillator. The close-packed design of the array makes cross-talk an inevitable contributor to distortion of measurements with this system. For $E_n \leq 25$ MeV almost all the detection efficiency comes from n-p scattering, and the simple two-body kinematics can be used as the basis for identifying cross-talk events. A Monte-Carlo code was developed to simulate the detection process. We found that most cross-talk events could be distinguished from real two-neutron events. A test experiment for comparison with the code was performed with neutrons from the ^{7}Li(p, n)^{7}Be reaction at E_p = 30 MeV. With this reaction all two-detector coincidences are cross-talk events. Consistency between the experimental data and the simulation results was obtained.

To my wife and my grandmother, the two most important women in my life.

Acknowledgements

I would like to thank my advisor, Aaron Galonsky. The truth is that without his help, I could not reach where I am today. Even If I were a native English speaker, words could not express my gratitude to him. For more than six years, he has constantly provided me guidance, and passed knowledge to me so unselfishly. It was he who made me become a PHYSICIST, which I will cherish in my entire life. I learned from him not just about Physics but also about genuinely great American people. The treasure I am going to take from him will be with me forever. I would also like to thank Marion for her warmth and kindness.

I want to thank the other members in my guidance committee: Professor Tim Beers, Professor Alex Brown, Professor Gregers Hansen, Professor Brad Sherrill, Professor Dan Stump for sitting in my committee and giving me valuable advise.

I don't think I could have completed my thesis experiment without the help from my colleagues: Jon Kruse, Phil Zecher, Ferenc Deak, Akos Horwarth, Adam Kiss, Zoltan Seres, Kazuo Ieki, Yoshiyuki Iwata. It was a unique experience working with each every one of them. I may forget how they look like one day, but I will never forget their stories.

It would have been hard for me to work at the lab days and nights without the lively conversations with my officemates. By the way, my office was probably the only place where I did not feel that I was a foreigner because it was truly international. Starting

from Brian Young, the "Rush Linbaugh" guy, then came Mathias Steiner, the "car" guy, Mike Fauerbach, the "Jing, that is your fault and I am going to tell your wife" guy, Marcus Chromik, the only German I know wearing a yellow sweater of the Brazilian National Soccer Team, Sally Gaff, the nicest graduate student ever worked in the office, Don Anthony, the "Jing, your wife has called" guy. Thanks, guys!

It will make me very uncomfortable if I forget to thank the Cyclotron people. To the people I worked with or not worked with, I want to say "Thank you!" To me, you are indispensable for Cyclotron's every bit of glory.

Special thanks go to my friendship Family, Fred and Charlotte, for their love, their encouragement and the candles they lighted at my birthdays. In the past six years, they made every holiday so desirable and so enjoyable. If I haven't been home sick, it is because of their care. I will never forget the four days I stayed with them before my oral defense, the defense that I would like to entirely dedicate to them. Thanks, Fred and Charlotte, for the past six years and for the many years to come!

I want to thank my parents, Shizhong Wang and Liqiong Peng, for giving us the freedom to go on with my personal life and for the sacrifice they have made in order for me to chase my dreams.

I dedicate part of my thesis to my grandmother because she is one of the greatest women in my life. Not only did she bring me up, but also showed me that love is the single most beautiful thing in the world. Thank you, grandma! May happiness forever with you in

heaven!

I cannot imagine working through the past six years without my wife, Lei. It is her support, encouragement that made this thesis possible. I want so much to thank her for never letting me give up, for never letting me lose my confidence, for staying with me during my ups and downs, for the delicious dishes and most importantly, for being my lovely wife. I sometimes wonder why I am the luckiest one in the world. For you, dear Lei!

TABLE OF CONTENTS

PART II

APPENDICES

LIST OF TABLES

LIST OF FIGURES

PART I - The Electromagnetic Excitation of ^{6}He

1 Introduction

1.1 Neutron Halo

The development of radioactive nuclear beams (RNB) around the world has brought much attention to nuclei far from stability. A series of experiments with RNB led to the discovery of the neutron halo structure in light nuclei near the neutron dripline. It started with two experiments performed at the Bevalac of the Lawrence Berkeley Laboratory to measure the interaction cross sections of He isotopes-^{3,4,6,8}He [1] and Li isotopes-^{6,7,8,9,11}Li [2] at 790 MeV/u. From these experiments, the interaction radii of those He isotopes and Li isotopes were deduced. The remarkably large radii of ^{6}He, ^{8}He and ^{11}Li suggested a long tail in the matter distribution of these nuclei. Later, Kobayashi et al. [3] found that the transverse momentum distribution of the ^{9}Li fragment from ^{11}Li breakup is extremely narrow. The narrow transverse momentum distribution suggested a large spatial distribution of the nuclear matter. These observations became the central evidences of the neutron halo [4,5,6] as a special property of light nuclei on the neutron dripline.

In a neutron halo nucleus, a low-density tail of the neutron distribution is extended out to a large distance from the center of the nucleus. The long tail is caused by the small separation energy of the neutrons (~ 1 MeV) compared to 6-8 MeV for stable nuclei. If we assume that a neutron is loosely bound to an inert core, and the interaction potential between the neutron and the core is a square well, the s-wave function of the

neutron outside the potential is expressed as

$$\psi(r) = \left(\frac{2\pi}{\kappa}\right)^{-1/2} \frac{e^{-\kappa r}}{r}\left[\frac{e^{\kappa R}}{(1+\kappa R)^{1/2}}\right], \qquad (1.1.1)$$

where R is the width of the potential; κ, which determines the steepness of the density tail, is related to the neutron separation energy ε by

$$(\hbar\kappa)^2 = 2\mu\varepsilon, \qquad (1.1.2)$$

where μ is the reduced mass of the system. The density distribution of the neutron is written as

$$\rho(r) = |\Psi(r)|^2 \propto \frac{e^{-2\kappa r}}{r^2}. \qquad (1.1.3)$$

As κ decreases with the decrease of the separation energy ε, the tail of the neutron density distribution extends further. To understand the narrow momentum distribution of the fragment from a neutron halo nucleus, we take the Fourier transformation of the wave function:

$$f(p) = \frac{C}{p^2 + (\hbar\kappa)^2} \qquad (1.1.4)$$

which is the momentum distribution function of the valence neutron. As shown by the equation, the width of the momentum distribution is related to κ. The smaller the separation energy ε, the smaller the parameter κ, therefore the narrower the distribution. This can be understood from Heisenberg's uncertainty principle-the wider the distribution in coordinate space, the narrower the distribution in momentum space.

The large coulomb dissociation cross section in experiments of halo nuclei impinging on high-Z targets led to a proposition of a low-lying excitation mode called the

soft dipole mode (SDM) [4]. In the SDM of ^{11}Li, for example, the ^{9}Li core oscillates against the neutron halo at a low frequency. So far, whether or not there is a SDM in ^{11}Li is still under investigation. The large electromagnetic dissociation cross section for ^{11}Li [7,8,9] seems to favor the existence of a SDM. The experiment by Sackett et al.[10] suggests a direct coulomb breakup because the deduced mean lifetime of the excited ^{11}Li is too small compared to the lifetime of a resonance determined from the ^{11}Li dipole strength function. Since the early experiments, many more experiments have been done to study these properties of neutron halo nuclei, especially those of ^{11}Li. At the same time, theoretical models, from the early simple dineutron model to complex three-body microscopic models, were made to explain the experimental results. Although the models successfully reproduced either the reaction cross sections, the nuclear radii or the fragment momentum distributions of some neutron halo nuclei such as ^{6}He and ^{11}Li, the results about SDM is inconclusive. These models will be discussed in a later section.

1.2 ^{6}He Nucleus

Theoretically, one may expect similar exotic structure and properties for all nuclei near the driplines. The ^{6}He nucleus is one of the lightest and simplest such nuclei. The study of the ^{6}He nucleus can contribute to the understanding of the properties of dripline nuclei. Even though both ^{6}He and ^{11}Li are typical examples of the so called borromean nuclei [11], where none of the binary systems have bound states, compared to ^{11}Li, ^{6}He is a more ideal system to study the exotic phenomena of dripline nuclei, because the α-core is more inert than the ^{9}Li-core and the underlying α-n interaction is well known. The ^{6}He nucleus has no bound excited states [12]. When ^{6}He is excited to a state above the 2-n

separation energy of 0.975 MeV, a three-body decay may occur ($^6He \rightarrow {}^4He + n + n$). If ^6He is excited to the continuum above 1.87 MeV, another decay channel is open. The ^6He nucleus can split into a ^5He and a neutron. Because ^5He is unbound to neutron decay, it further splits into a ^4He and a neutron. This decay mode is called sequential decay, which may play an important role in the dissociation of ^6He [9,13,14].

1.3 Experiments

Although ^{11}Li has been studied intensively at many different beam energies and through the interaction with many kinds of targets, only a very small number of experiments have been performed on ^6He. Tanihata et al. [1] measured the interaction cross sections of ^6He at 0.79 GeV/u on Be, C and Al targets, from which the nuclear interaction radius was deduced. Then, Kobayashi et al. [8,15] measured the interaction cross sections of ^6He around 1 GeV/u and the transverse momentum distribution of ^4He from the fragmentation of ^6He. Later, the transverse momentum distributions of neutrons from ^6He at 0.8 GeV/u on Pb and C targets were measured by the same group [9]. The momentum distribution of ^4He from ^6He fragmentation, detected at 5° in the laboratory for beam energies near 65 MeV/u, was measured [16]. Not until 1996 were the total reaction cross sections of ^6He at intermediate energies (20-40 MeV/u) reported [17]. An experiment was performed recently to study the one-neutron stripping mechanism of ^6He at 240 MeV/u [14].

1.4 Theoretical models

To understand the properties of ^{11}Li, several models were developed. The dineutron and cluster models [4, 18] were introduced first. In these models, ^{11}Li is treated as a cluster in which two neutrons are weakly coupled to a ^{9}Li core. The shell model by Bertsch et al. went a little further, taking into account the weak binding of the last neutron in ^{11}Li. As ^{6}He drew more attention of theorists, more elaborate models were applied to explain the properties of ^{6}He. The cluster-orbital shell model (COSM) [12,19,20] assumes a 3-body structure of ^{4}He + n+ n in which the ^{4}He core is treated as being inert, the valence neutrons are allowed to occupy any high single-particle orbits and the weak binding of the valence neutrons is also taken into account. Because COSM does not reproduce the binding energy of ^{11}Li and ^{6}He, a hybrid model combining COSM and the microscopically extended cluster model [22] was introduced. One of the interesting results of the hybrid model is that the two valence neutrons stay in shell model orbits when they are close to the core, but form a cluster (dineutron) when they are far from the core. In addition to the COSM and the hybrid models, there are other three-body calculations to study the structure of ^{6}He [13,23-30]. The results of these calculations will be discussed when the experimental results are presented in chapter 3.

1.5 Coulomb Excitation

Fragmentation of a nucleus is the result of either nuclear or electromagnetic interaction between a projectile nucleus and a target nucleus. Due to the short range of the nuclear force, the electromagnetic interaction comes to dominate the fragmentation as the distance between the projectile and the target increases. Electromagnetic collision

has become a popular way to study nuclear matter since the reaction mechanism is very well understood compared to a nuclear collision. The reaction mechanism in a relativistic collision is described by the equivalent photon method, called the Weizsäcker-Williams method. Bertulani et al. [31] provided a detailed review of this method. The key features relevant to the experiment are presented here.

Let's consider a target nucleus with a fixed position and a projectile nucleus passing by with an impact parameter larger than the strong interaction radius. The projectile can be excited by absorbing one of the equivalent photons surrounding the target nucleus. For a halo nucleus such as ^{6}He, the absorption of the photon may displace the neutrons while the nuclear force tries to pull the neutrons back toward the core. If the motion is repeated, a resonance may be formed, and the oscillation may last for a long time (long enough for the projectile to be far away from the target nucleus) before the projectile breaks up. The probability of coulomb excitation at energy E_γ depends on the number of photons of energy E_γ and the probability that the projectile nucleus absorbs such a photon. For an E1 transition the differential coulomb excitation cross section is expressed as

$$\frac{d\sigma_{E1}}{dE_\gamma} = \frac{1}{E_\gamma} n_{E1}(E_\gamma)\sigma_\gamma^{E1}(E_\gamma), \qquad (1.5.1)$$

where $n_{E1}(E_\gamma)$ is the number of equivalent photons with energy E_γ surrounding the target and σ_γ^{E1} is the photonuclear cross section for the photon energy E_γ. The equivalent photon number $n_{E1}(E_\gamma)$ can be expressed as

$$n_{E1} = \frac{2}{\pi} Z_1^{\,2} \alpha \eta^2 e^{-\pi\eta} \left(\frac{c}{v}\right)^2 \int_{\varepsilon_0}^{\infty} \varepsilon d\varepsilon \left\{ \frac{1}{\gamma^2} \frac{\varepsilon^2 - 1}{\varepsilon^2} [K_{i\eta}(\varepsilon\eta)]^2 + [K_{i\eta}'(\varepsilon\eta)]^2 \right\}, \quad (1.5.2)$$

where Z_1 is the charge of the projectile, $\alpha = \frac{e^2}{\hbar c}$ is the fine structure constant, v is the velocity of the projectile, $\varepsilon = (\sin(\theta/2))^{-1}$ is the eccentricity parameter used to account for the Rutherford bending of the projectile, $K_{i\eta}$ is the modified Bessel function with imaginary index ($i\eta$), $K_{i\eta}'$ is the derivative of $K_{i\eta}$ and

$$\eta = \omega a / \gamma v, \quad (1.5.3)$$

where ω is the frequency of the photon ($E_\gamma = \hbar\omega$), $\gamma = (1 - \frac{v^2}{c^2})^{-\frac{1}{2}}$ is the Lorentz factor, $a = \frac{Z_1 Z_2 e^2}{m_0 v^2}$ is half the distance of closest approach in a head-on collision and m_0 is the reduced mass of the ions. The photon distributions for the six targets used in our experiment are shown in Fig.1.1. Furthermore, the photonuclear cross section is related to the electric dipole strength function $\frac{dB_{E1}}{dE_\gamma}$ by

$$\sigma_{E1}(E_\gamma) = \frac{16\pi^3 E_\gamma}{9\hbar c} \frac{dB_{E1}}{dE_\gamma} \quad (1.5.4)$$

One of the nice features of the equivalent photon method is that it ties the dipole strength function $\frac{dB_{E1}}{dE_\gamma}$ to the differential coulomb cross section $\frac{d\sigma_{E1}}{dE_\gamma}$ through the photon spectrum $n_{E1}(E_\gamma)$.

$$\frac{dB_{E1}}{dE_\gamma} = \frac{9\hbar c}{16\pi^3} \frac{1}{n_{E1}(E_\gamma)} \frac{d\sigma_{E1}}{dE^\gamma} \quad (1.5.5)$$

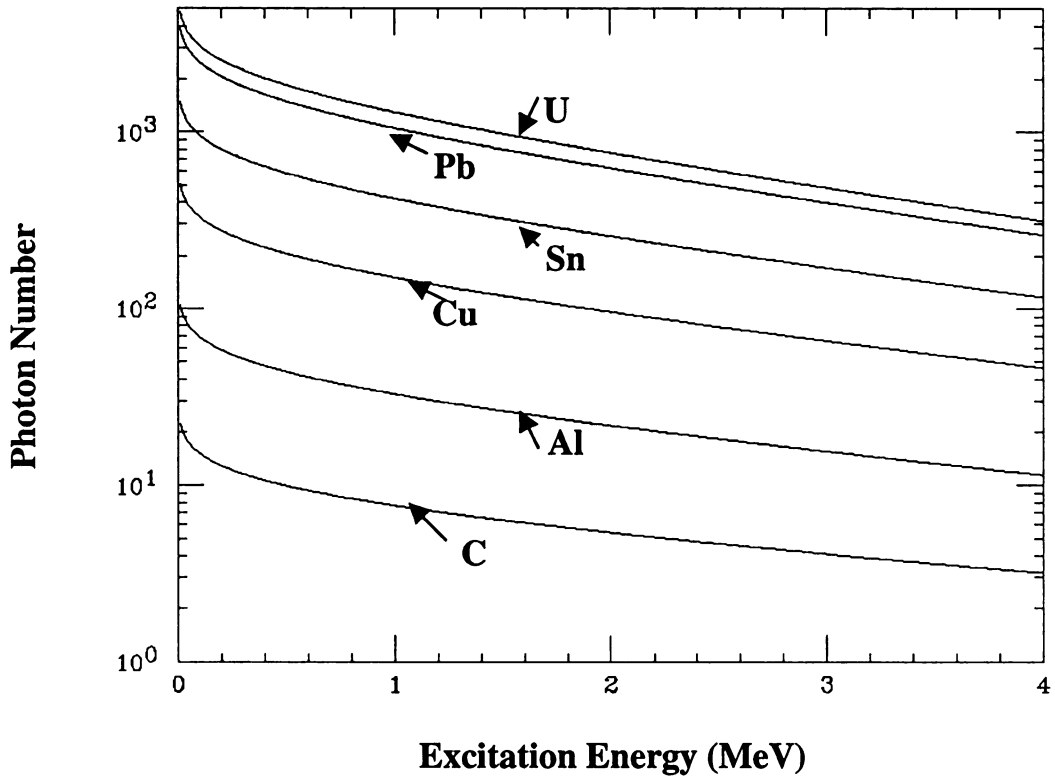

Figure 1.5. 1 Photon distributions $n_{E1}(E_\gamma)$ for the six targets used in the experiment.

With $\frac{d\sigma_{E1}}{dE_\gamma}$ measured in an experiment and $n_{E1}(E_\gamma)$ calculated for the target nucleus, $\frac{dB_{E1}}{dE_\gamma}$ can be determined. Other multipole excitations, such as M1 and E2 excitations, are neglected in the energy region we are interested in since their contribution is much smaller.

2 Experimental Setup

The schematics of the experimental setup are shown in Fig. 2.1.1. I would like to describe the ^{6}He beam and the three major components of the detection system—the neutron wall detectors, the deflecting magnet and the fragment detectors.

2.1 The ^{6}He Beam

The average energy of the ^{6}He beam striking the experiment targets was 25.2 MeV/u. The primary reason for choosing this beam energy is that good neutron cross-talk identification can be achieved in the neighborhood of this energy, which will be discussed in Part II. Even though lower energy is desirable for cross-talk identification, it would also significantly reduce the ^{6}He beam intensity and make the quality of the beam worse. Furthermore, we wanted the ^{6}He projectile to travel fast enough so that its contact with the target nucleus is "sudden". This will be explained later in section 3.2.

The ^{6}He beam in the experiment was produced by bombarding a 2.0 g/cm^{2} Be production target with an 80 MeV/u $^{18}O^{6+}$ beam from the K1200 cyclotron at the National Superconducting Cyclotron Laboratory at Michigan State University. The ^{6}He particles had an average energy of about 60 MeV/u after exiting the production target. They were later degraded to a beam with an average energy at 25.2 MeV/u by a thick plastic wedge. The ^{6}He particles were then separated from the other particles at the A1200 Fragment separator before it was sent into the N4 vault, as shown in Fig. 2.1.1, where our experiment

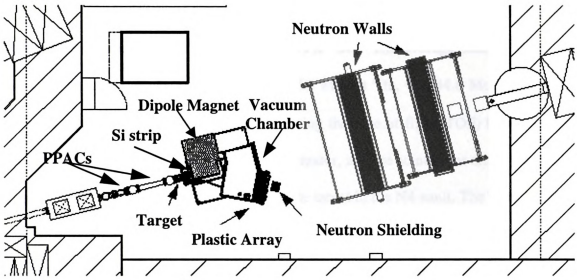

Figure 2.1. 1 The experimental setup (not to scale). This is the top view of the N4 vault at the NSCL. The neutron walls, one behind the other, were placed 5.00 and 5.84 meters from the target. The plastic scintillator array was mounted inside the vacuum chamber about 1.8 meters from the target. The silicon strip detectors were located at the entrance of the magnet, 15.24 cm downstream from the target. The two PPACs were mounted 38.64 cm and 130.08 cm upstream from the target.

was performed.

The beam which was delivered to the targets has a rate of about 10,000 particles per second. It consisted of 81% ^{6}He and 19% ^{9}Be. The average energy of the ^{9}Be particles, under the same Bρ = 2.16976 as 25.2 MeV/u ^{6}He, was 44.8 MeV/u. The ^{9}Be particles were separated from ^{6}He particles using the time of fight (TOF) between a thin plastic scintillator placed after the A1200 Separator, and the scintillator array mounted in a vacuum chamber at about 1.8 meters from the target in the N4 vault. The TOF spectrum is shown in Fig. 2.1.2. For each particle passing through, the scintillator array gave the start signal and the delayed pulse from the plastic wedge gave the stop signal. The travel distance was 41.5 meters. The left peak in Fig. 2.1.2 is ^{6}He and the right one is ^{9}Be.

The experiment was performed with six targets --- U, Pb, Sn, Cu, Al and C, whose values of thickness are 344 mg/cm^2, 384 mg/cm^2, 373 mg/cm^2, 274 mg/cm^2, 237 mg/cm^2 and 94 mg/cm^2, respectively . We ran the beam about 100 minutes with the U target, about 40 minutes each for the other targets. We also took a 100-minute run with a blank target in order to exclude the reactions from anything other than the targets. During the runs with the blank target, the beam energy was reduced to 22.6 MeV/u to account for the energy loss in the targets.

The ^{6}He beam was focused by a quadruple about 5 meters upstream from the target. The size of the beam spot on the target was about 1cm x 1cm. In order to

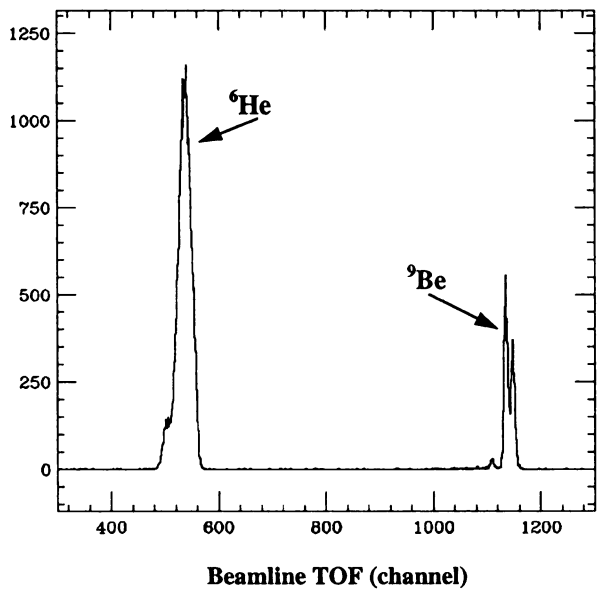

Figure 2.1. 2 The beamline time. The start was given by the scintillator array, and the stop was given by a plastic scintillator 41.5 meters upstream from the scintillator array.

the momenta of the fragments (^{4}He + 2n) from the dissociation of ^{6}He, the incident direction and position on the target of each ^{6}He have to be accurately measured. This was achieved by placing two position-sensitive parallel plate avalanche counters (PPACs) upstream from the targets. The PPACs were mounted to the beamline, 38.64 cm and 130.08 cm from the target. The signals in the PPACs were divided into up, down, top and bottom. From the pulse heights, the particle position in each PPAC was calculated with a resolution about 1 mm. The detection efficiency of one PPAC for the ^{6}He at 25 MeV/u was about 86%, which is the ratio between the number of ^{6}He detected by a PPAC and that detected by the Si strip detectors. The detection efficiency of the Si detectors should be 100% for the ^{6}He beam.

2.2 The Neutron Wall Detectors

Neutrons in the experiment were detected by the neutron wall facility at the NSCL. The facility was originally built as an improvement over an old neutron detection system [10] in a similar experiment performed in 1991 to measure the coulomb excitation of ^{11}Li. In that experiment, two arrays consisting of 54 cylindrical scintillation detectors, each about 7.6 cm thick and 12.7 cm in diameter, were made to detect the two neutrons from the ^{11}Li breakup. A few drawbacks of the arrays made us decide to build a new detection system — a pair of neutron walls. These walls are described in Ref. [32] in detail. A brief description is given in the following paragraph.

The new facility is composed of a pair of large-area, position-sensitive neutron walls, one of which is shown in Fig. 2.2.1. Compared to the arrays used in 1991, the

walls are larger and use fewer photomultiplier tubes (PMT) per liter of scintillator. The walls have less dead space and inactive mass to scatter neutrons. The position resolution is somewhat improved. Each wall consists of 25 rectangular Pyrex cells filled with NE-213 liquid scintillator. Each cell is two meters long, with an internal cross section of 7.62 cm by 6.35 cm. PMTs are attached to the ends of a cell. The neutron time-of-flight (TOF) is obtained from the mean time of the PMT signals. The position of a neutron detected in a cell is determined from the time difference of these signals. Both time and position resolution [32] vary with the light output caused by the neutron's interaction in the scintillator. For a light output equal to that produced by a 1-MeV electron (defined as 1 MeVee), the time resolution (σ_t) is 0.8 ns. It reduces to 0.4 ns for a light output over 4 MeVee. The position resolutions (σ_p) for these light outputs are 6 cm and 3 cm, respectively. The neutron detection efficiency for one wall is 11% for 25 MeV neutrons if a threshold of 1 MeVee is set for the two phototubes at the ends of a cell. In experiments with the neutron walls, many of the neutrons produce less than or the same amount of light as γ rays. Therefore, the walls were built with the capability of pulse-shape-discrimination to distinguish neutron events from γ-ray events.

In most experiments, the two walls have been used with one wall behind the other as shown in 2.2.2. There are two advantages of using this configuration: (1) It enhances the detection efficiency. (2) It has the capability of detecting a pair of neutrons emitted with a small relative angle. In order to explain the second advantage, consider the

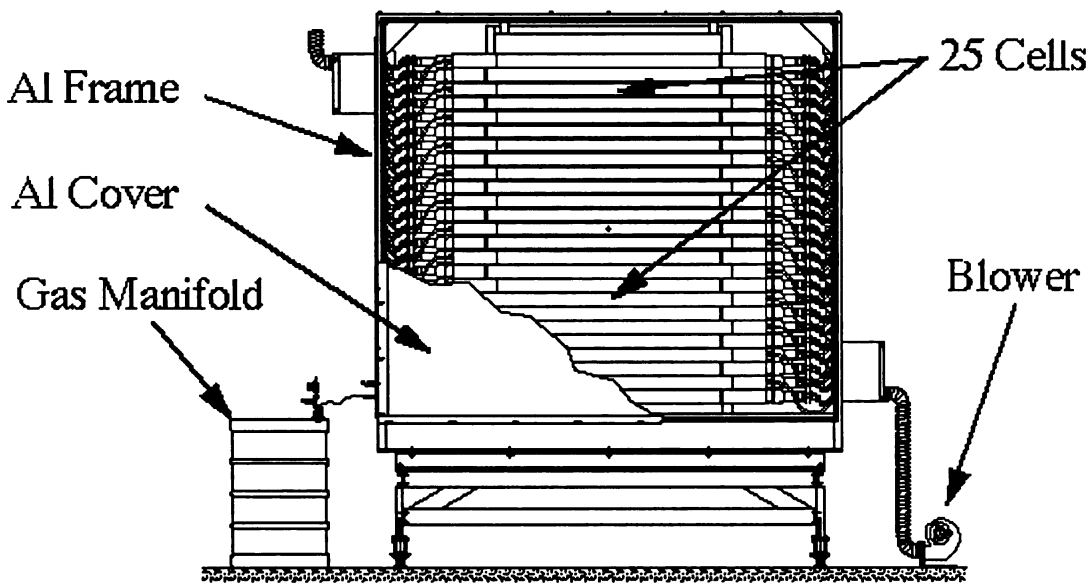

Figure 2.2. 1 The schematics of a neutron wall. Each of the two Neutron Walls is a 2m x 2m array of 25 individual cells. The cells are 2m long, have rectangular cross sections, and are stacked vertically to fill the entire 4 m^2 area with very little dead space between elements. Custom-made of Pyrex, the cells are filled with NE America's NE-213 liquid scintillator and are read out at each end by a Philips Photonics 3-inch photomultiplier tube.

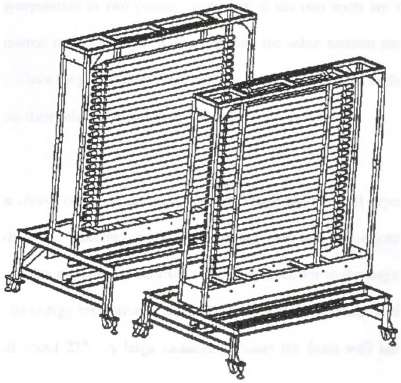

Figure 2.2. 2 The setup of the neutron walls in the experiment. This is a simplified picture of the walls without the aluminum cover and the other accessories.

extreme case — two neutrons emitted from a source with zero relative angle. If only one wall is used, the two neutrons will be detected in the same cell at the same time with a certain probability. Unfortunately, we cannot distinguish them because what we detect is just the superposition of two pulses. However, if the two walls are used, it is possible that one neutron makes a pulse in one wall and the other neutron makes a pulse in the other wall. Since they are detected in different cells, it is not hard to distinguish them and to determine their relative angle, even if it is 0°.

The choice of the distance between the target and the wall depends on the neutron energy, which is measured by TOF, counting rate and the requirement of angular coverage. In this experiment the front wall, the one closer to the target, is 5 meters from the target, its energy resolution is about 3% for 25-MeV neutrons, and the wall subtends an angle of about 23°. A large distance between the front wall and the back wall is advantageous for good cross-talk identification. The back wall was placed 84 cm from the front wall.

2.3 The Deflecting Magnet

In the ^{11}Li experiment performed in 1991, a very different experimental setup was used, as shown in Fig. 2.3.1. The remaining energy of ^{11}Li and ^{9}Li after the silicon ΔE detectors were measured with a 6 cm × 6 cm × 1.2 cm CsI(Tl) crystal which was placed between the target and the neutron detectors. Because all ^{11}Li and ^{9}Li particles stopped in

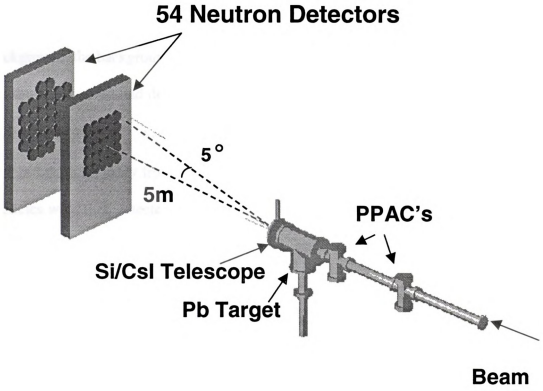

Figure 2.3. 1 The experimental setup for the ^{11}Li experiment. The Si-CsI was placed between the target and the neutron detector arrays.

the CsI(Tl), lots of background neutrons were produced there. The CsI(Tl) was much thicker than the 0.52-mm Pb target so that there were more neutrons from the CsI(Tl) than from the target. Even though data were taken with a blank target to subtract the background, the background from the CsI(Tl) was a major concern. In order to overcome the drawback of the old detection system, a magnetic dipole with a pole gap of 7.5″ and pole area of 13″×24″ was installed between the target and the neutron walls to deflect charged particles away from the beamline. The deflected fragments and remaining beam particles were then detected in a scintillator array somewhat far from the beamline. The position of the magnet in the detection system can be found in Fig. 2.1.1.

In order to figure out where to position the scintillator array, we calculated the trajectories of the beam particles with different energies. To make the calculation accurate, the field of the magnet was mapped with a Hall probe. Because the field was expected to be non-uniform along the direction perpendicular to the pole surface at the area close the pole edge, the magnetic field was measured in five planes—the middle plane, and the planes which are 1, 2, 3 inches above and 1 inch below the middle plane. Fig. 2.3.2a shows the magnet poles and its middle plane. The distribution of the magnetic field in the middle plane is shown in Fig. 2.3.2b. The maximum intensity of the field is about 1.5 Tesla. The mapped field extends to the area about 15 inches beyond the edges of the magnet. At the edge of the poles, the field quickly drops to an insignificant level. The magnet field can be regulated from 0 to 1.5 Tesla in principle. This enabled us to deflect one charged particle beam into different parts of the fragment array for energy calibration.

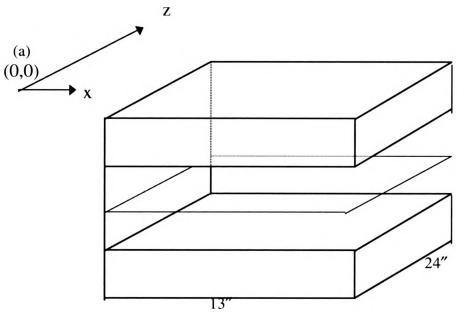

(b)

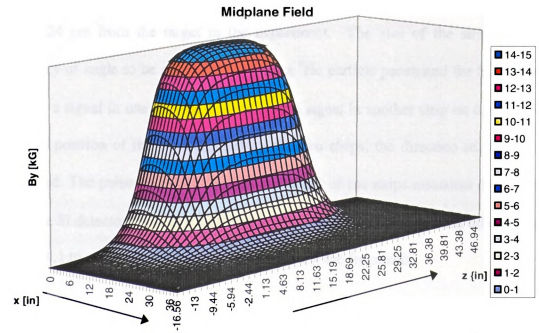

Figure 2.3. 2 (a) The deflecting magnet and the mapped middle plane. The poles cover a dimension of 13 inch × 24 inch. (b) The magnetic field at the middle plane. The maximum intensity is 1.5 Tesla. Refer to (a) for the coordinates.

2.4 The Fragment Detectors

2.4.1 Si Strip Detectors

In order to identify the reaction fragments, two silicon ΔE detectors and sixteen plastic E detectors were used. A big vacuum chamber was built to accommodate the fragment detectors and the target. The ΔE detectors were mounted onto an aluminum flange through which electronic cables were connected to provide bias and to pick up signals. Each ΔE detector, 5cm x 5cm x 250μm, in Fig. 2.4.1, was a MICRON position sensitive silicon strip detector, consisting of 16 horizontal strips on one side and 16 vertical strips on the other. Each strip is 3.125 mm wide. The gap between the strips is about 0.1mm. The 32 strips together form a grid consisting of 256 square pixels, as shown in Fig. 2.4.1, each of which has an area of 3.125 x 3.125 mm^2. The strip detectors were 15.24 cm from the target in the experiment. The size of the strip causes the uncertainty of angle to be about 1.2°. When a ^{4}He particle penetrated the Si detector, it produced a signal in one strip on one side and a signal in another strip on the other side. From the position of the pixel defined by the two strips, the direction of the ^{4}He was determined. The pulse height of the signal in either of the strips measures the ΔE of the ^{4}He in the Si detector. The two Si detectors were positioned next to each other as shown in Fig. 2.4.1 to achieve large angular acceptance for the fragments.

Besides the slow signal used for ΔE measurement, a fast signal was picked up from the vertical strip for TOF measurement. However, the fast signal was distorted due to interference from the power supply of the magnet. Signals from the scintillator

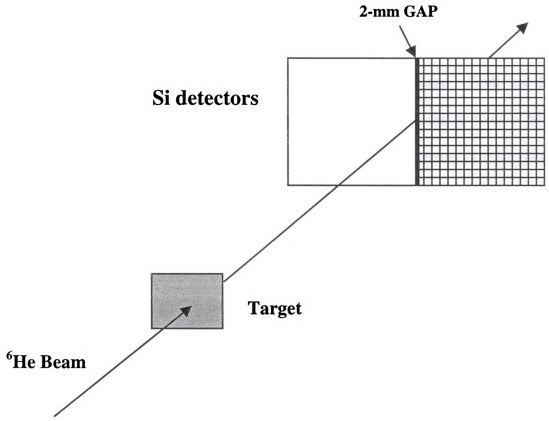

Figure 2.4. 1 The setup of the 250μm Si strip detectors. The 16 horizontal strips and 16 vertical strips are shown in detector #2. The 32 strips form 256 pixels, each with an area of 3.125×3.125 mm^2. The strip detectors are 15.24 cm from the target. There is a 2mm gap between the two detectors.

array were used instead for TOF measurement.

2.4.2 The Scintillator Array

The scintillator array consists of 16 BC408 plastic bars. Each bar has a dimension of 40.64 cm × 4 cm × 2 cm. The 16 bars cover an area of 40.64 × 64 cm^2. The top and side views of the array are shown in Fig. 2.4.2. As shown in the figure, two photomultipliers (PMTs) were attached to the ends of each bar. These PMTs are 8575 Burle tubes [33] and R317 Hamamatsu tubes [34]. All the PMTs have 12 dynodes and an anode. Because the phototube is wider than the scintillator, a zigzag positioning of the detectors was chosen to ensure no dead splace between the scintillator bars. The PMTs were covered with magnetic shields. High voltage was put on a tube through a PMT base made for the experiment at the NSCL. The base was a modified version of E934 Hamamatsu bases. The design of the base is shown in Figs. 2.4.3 and 2.4.4. The two major modifications:

(1) The resistors of the E934 bases were replaced with those with half the resistance. This was to ensure that the bleeder current ----the current flowing through the resistors, is much larger than the anode current. The larger the bleeder current relative to the anode current, the more linear the signals.

(2) Unlike conventional bases, the base for the experiment is divided into two parts---a divider board and a socket. A divider board includes the resistors of the base

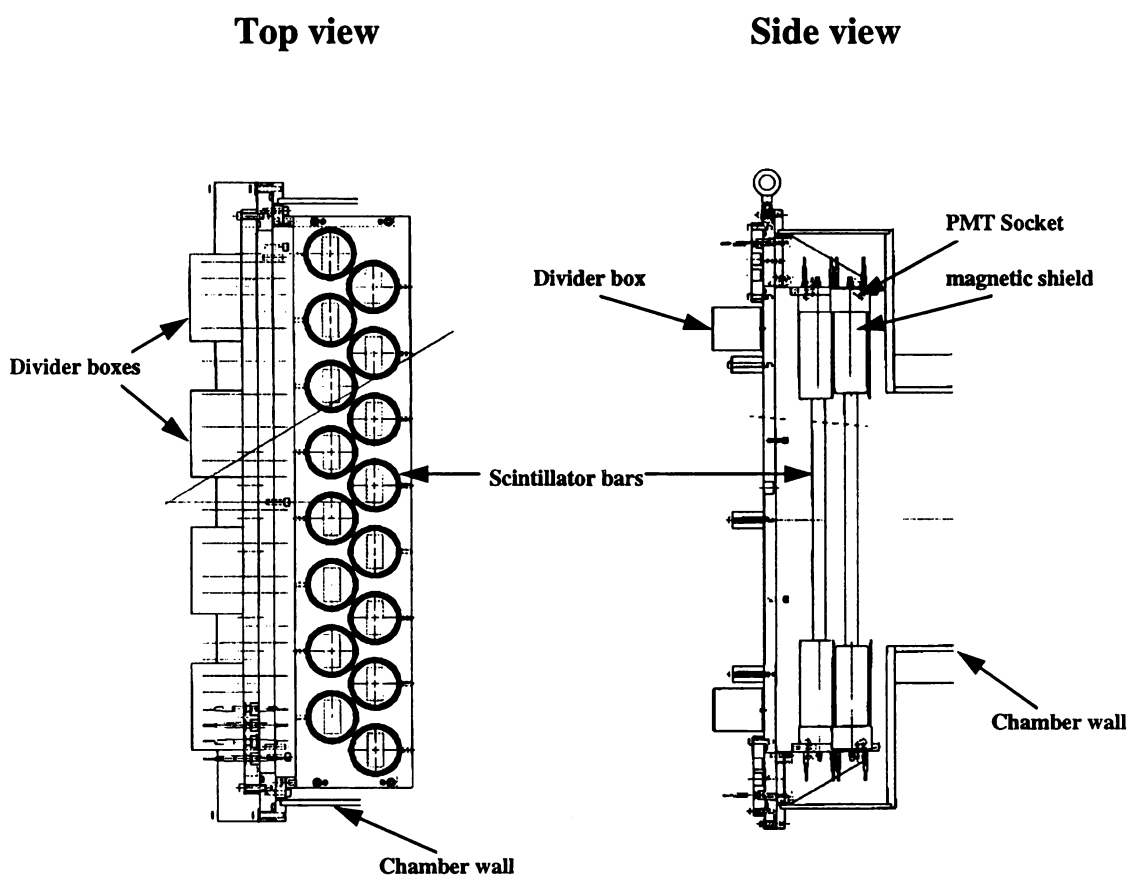

Figure 2.4. 2 The top and side view of the scintillator array. The array consists 16 BC408 plastic bars. Each of these rectangular bars has dimensions $40.64 \times 4 \times 2$ cm^3. Two photomultiplier tubes (PMT) are attached to the ends of each bar. The PMTs are covered with magnetic shields.

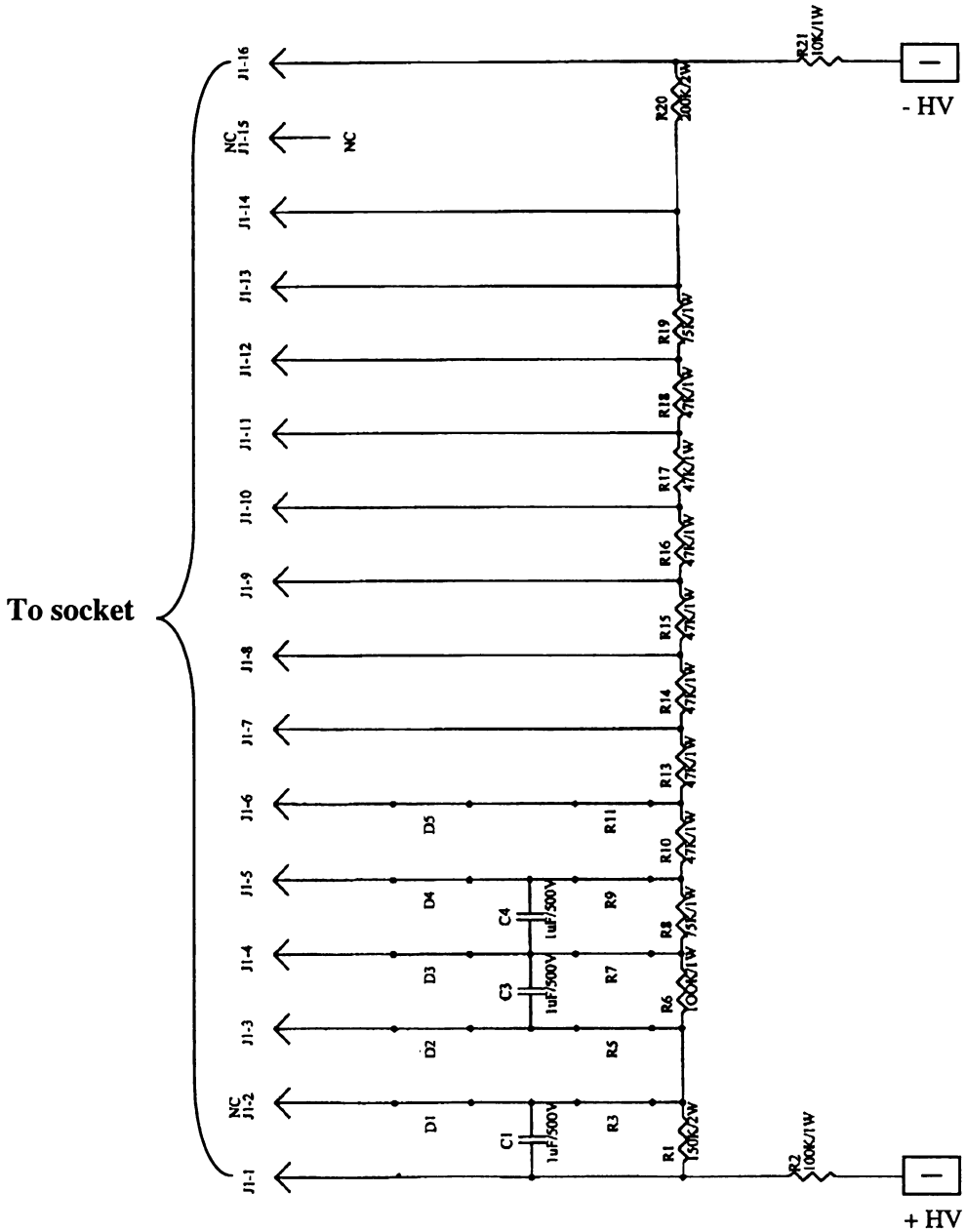

Figure 2.4. 3 The divider of the PMT base designed for the scintillator bar. The divider was placed in the air to dissipate the heat. The divider is connected to the socket in Fig. 2.4.4 according to the order from J1-1 to J1-16, which can be found in this figure and in Fig. 2.4.4.

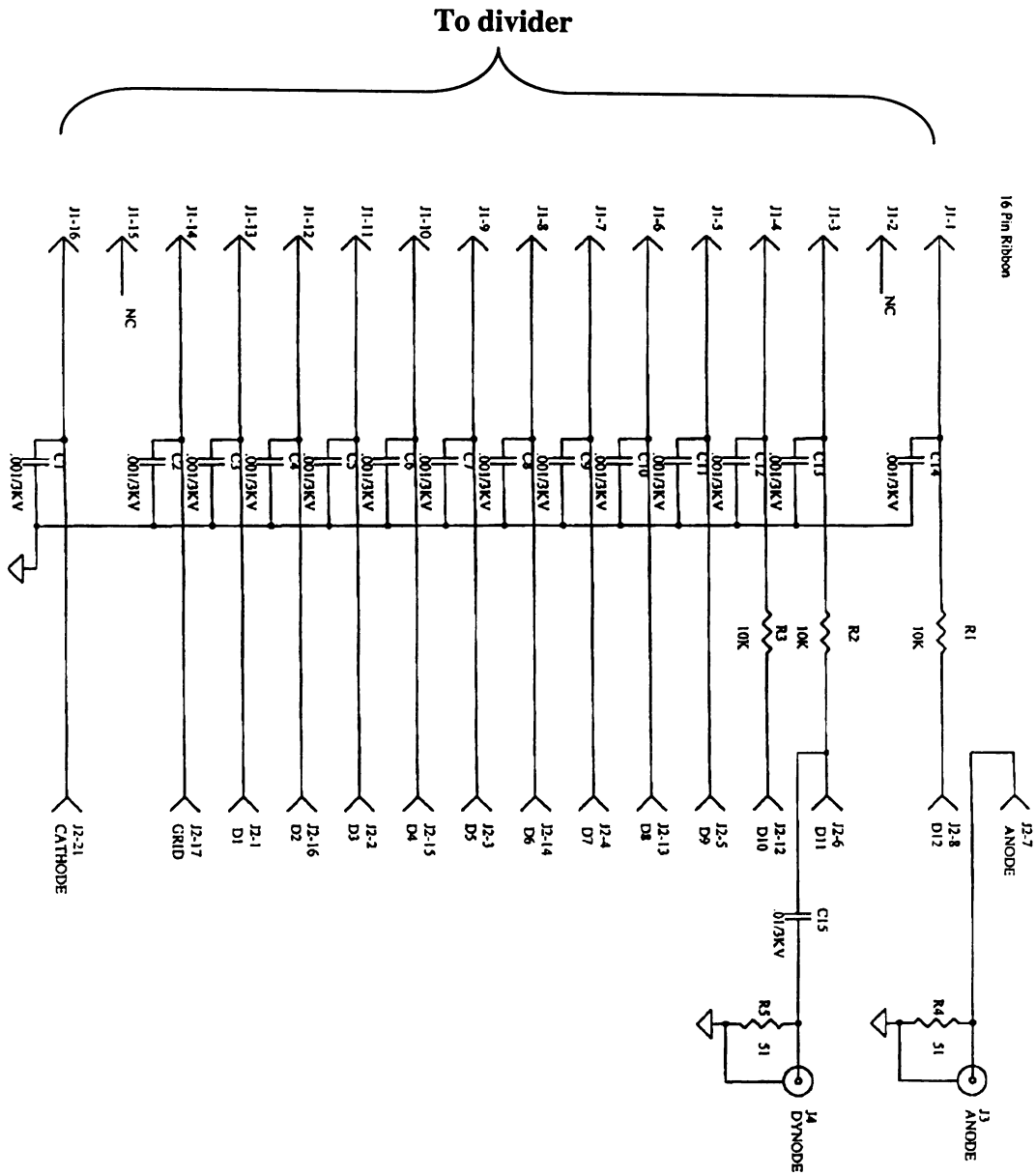

Figure 2.4. 4 The socket of the PMT base designed for the scintillator bar. The socket, attached to one end of a scintillator bar, was placed inside the vacuum chamber.

used to divide the high voltage among the dynodes of a PMT. A socket includes the capacitors to provide electrons. The socket is attached to a PMT placed in the vacuum chamber. The divider board is out in the air. By putting the resistors outside the chamber, we can avoid overheating them and the tube. If the resistors were put inside the vacuum with the socket, as in conventional bases, the heat generated in the resistors would be hard to dissipate and might result in damage to the PMTs. Each socket is connected to a divider board through a 16-pin vacuum feedthrough glued on to the back plate. Four divider boards are placed in a divider box, which is mounted on the back plate of the vacuum chamber as shown in Fig. 2.4.1. The signals from the 11th dynode and anode are picked up from the socket in the vacuum, then transmitted to the electronic modules through the lemo feedthroughs on the back plate.

The positions of the detectors were not randomly chosen as mentioned before. If the array was put too close to the target, it would stand between the neutron walls and the target. Neutrons from the target might then be scattered off the scintillator bars and become background neutrons for the neutron walls. Furthermore, many neutrons produced in the scintillator bars could then get into the neutron walls. On the other hand, if the array is put too far away from the target, its acceptance will be too small to detect both the ^{6}He and ^{4}He because ^{4}He is deflected more than ^{6}He by the magnet. To take these factors into account, the center of the array was positioned about 1.8 meters from the target [see Fig. 2.1.1]. Actually, this distance was not only chosen to accommodate ^{6}He and ^{4}He around 25 MeV/u, but also chosen to accommodate ^{8}He, ^{6}He, ^{11}Li and ^{9}Li

around 25 MeV/u because the dissociation of ^{8}He and of ^{11}Li were also studied with the same experimental setup.

The two PMTs at the ends of a scintillator bar detect light signals produced by the energy loss of the fragments. The geometric mean of the integrated charges of the signals from the two PMTs measures the fragment energy so that the effect of light attenuation can be removed. The signal from the top photomultilier served as the start signal to measure the TOF of the beam particles between the scintillator bar and the plastic scintillator placed upstream in the beamline. The beamline TOF spectrum is shown in Fig. 2.1.2. The top signal also served as the stop signal to obtain the TOF between the neutron walls and the scintillator bar. The neutron energy was determined from this TOF.

3. Coulomb Dissociation of ^{6}He

3.1 2n Removal Cross-section

The direct approach to calculate the 2n removal cross-section σ_{2n} of ^{6}He is to count the number of the incident ^{6}He particle—N_0, and the number of the ^{4}He fragments produced in the target—N. Then use the equation:

$$N_0 - N = N_0 e^{-\sigma_{2n} nt} \qquad (3.1.1)$$

where n is the target density and t is the target thickness. Although the direct approach is straight forward, the 2-n removal cross section is determined using the n-^{4}He coincident events, in which a neutron is detected in the neutron walls and a ^{4}He is detected in the scintillator array. The reasons are given in the following paragraph.

First, the experiment was designed for a kinematically complete measurement of ^{6}He dissociation. The focus was on the events in which neutrons and a ^{4}He fragment were detected. Therefore, all the coincidence events were processed and recorded. The single-fragment events, in which either a cell in the neutron walls or a bar in the scintillator array fired, were downscaled by a factor of 500 in order to reduce the on-line processing time. Due to the limited beam time for each target, the number of the downscaled ^{4}He was very small. With the U target, the number of ^{4}He events was only 43, compared to 2,827 n-^{4}He events. So, the cross section determined from the singles data can have a very large uncertainty. Second, as we will discuss in sections 3.2 and 3.3, both the ^{6}He projectile and the ^{4}He fragment can be deflected into large angles by the

coulomb force from the target nucleus. The limited acceptance of the magnet poles results in some ^{4}He fragments not being detected by the scintillator array.

Before I show how to determine the 2-n removal cross section of ^{6}He from the n-^{4}He coincidence data, the ^{4}He fragment and neutrons produced in the experiment have to be identified.

3.1.1 ^{4}He Identification

When ^{6}He is excited by interacting with a target nucleus, the excitation energy eventually comes from the ^{6}He projectile itself. The energy provided has to exceed the 2-n separation energy of ^{6}He—0.975 MeV in order for a breakup to occur. The excitation energy is expected to be in the neighborhood of several MeVs. When an excited ^{6}He decays, the decay energy (the difference between the excitation energy and the separation energy) is shared among the fragments—a ^{4}He and two neutrons. Since the decay energy is much less than the incident energy ($\approx$ 144 MeV), the fragments of the incident ^{6}He beam are expected to travel at about the same speed as the beam. Therefore, the ^{4}He from the breakup carries about 2/3 of the energy of the ^{6}He. The resolution of the scintillator array ($\approx$ 4%) should be good enough to separate the two isotopes. Fig. 3.1.1 gives the energy distribution of the charged particles detected in the entire 16-scintillator array for the U target. The broad ^{4}He peak on the left of the ^{6}He peak can come from two sources. Other than from the target, the ^{4}He can be produced in the array through a dissociation of the ^{6}He in the scintillator itself. Because a ^{6}He can break up at any time

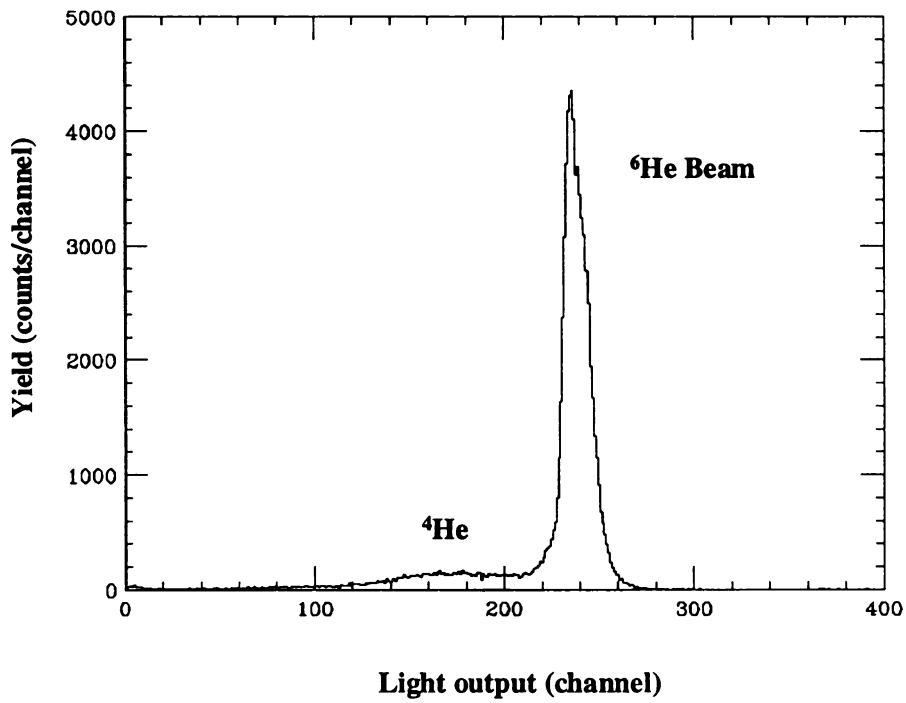

Figure 3.1.1 The light output in the entire 16-scintillator array.

before losing all the energy in the scintillator, the energy loss could be any value between 2/3 and 100% of the beam energy, resulting in the broad peak in Fig. 3.1.1. We need to identify the ^{4}He from the target.

With the deflecting magnet, we were able to do the identification. Due to different mass-to-charge ratios but similar velocities, the ^{4}He from the target and the unreacted ^{6}He were swept into different bars of the scintillator array. Since the magnetic field was accurately mapped, we were able to calculate the trajectory of charged particles at various energies. Figure 3.1.2 shows the trajectories of a ^{4}He ion and a ^{6}He ion coming from the target at 23 MeV/u. In this particular case, the ^{6}He hits bar 5, whereas the ^{4}He hits bar 10. In Fig. 3.1.3 and Fig. 3.1.4, the energy distributions for the sixteen scintillator bars are plotted for the data collected with the U target. As shown in these figures, the ^{6}He beam concentrates on bars 5 and 6. Some ^{6}He particles go into neighboring bars. The spread was caused by the dispersion of the beam and the coulomb scattering in the target. Clearly, the ^{4}He produced in the scintillator array can only appear in the bars where the ^{6}He beam stops. On the other hand, the ^{4}He from the target goes into higher-numbered bars far from the beamline. Figure 3.1.4 shows that almost all the ^{4}He from the target stopped in bars from no. 8 to no. 15. It appears that only an insignificant number of the ^{4}He went into the other bars in the array. So, the ^{4}He particles detected from bar 8 to bar 16 were identified as the fragments produced in the target.

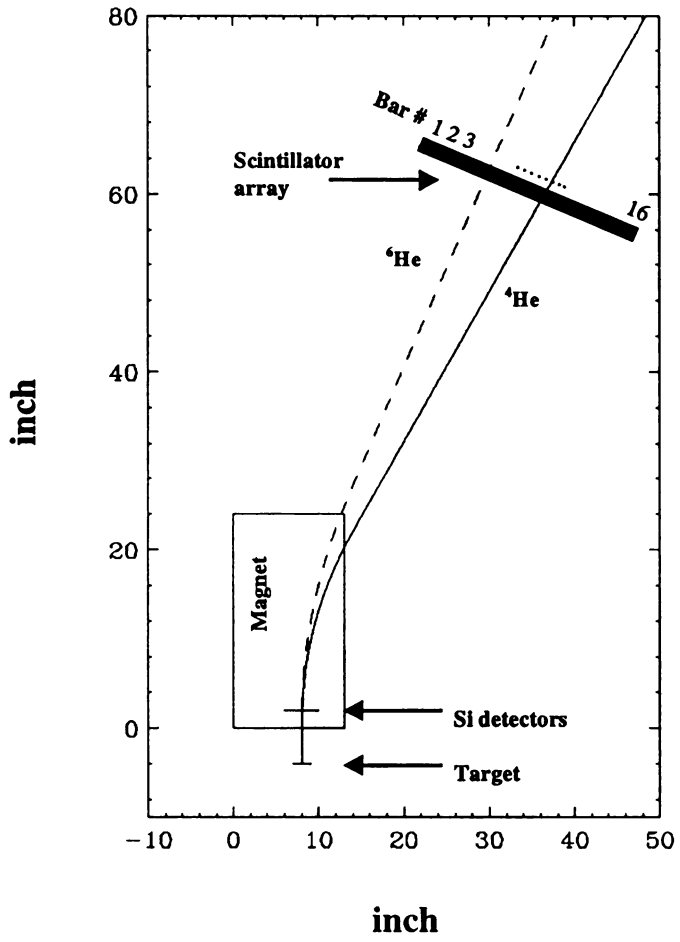

Figure 3.1.2 Trajectories of a ^{6}He projectile and a ^{4}He ion at 23 MeV/u. This is the result of a calculation with the mapped magnetic field. According to the calculation, the ^{6}He hits bar #5, and the ^{4}He hits bar #10.

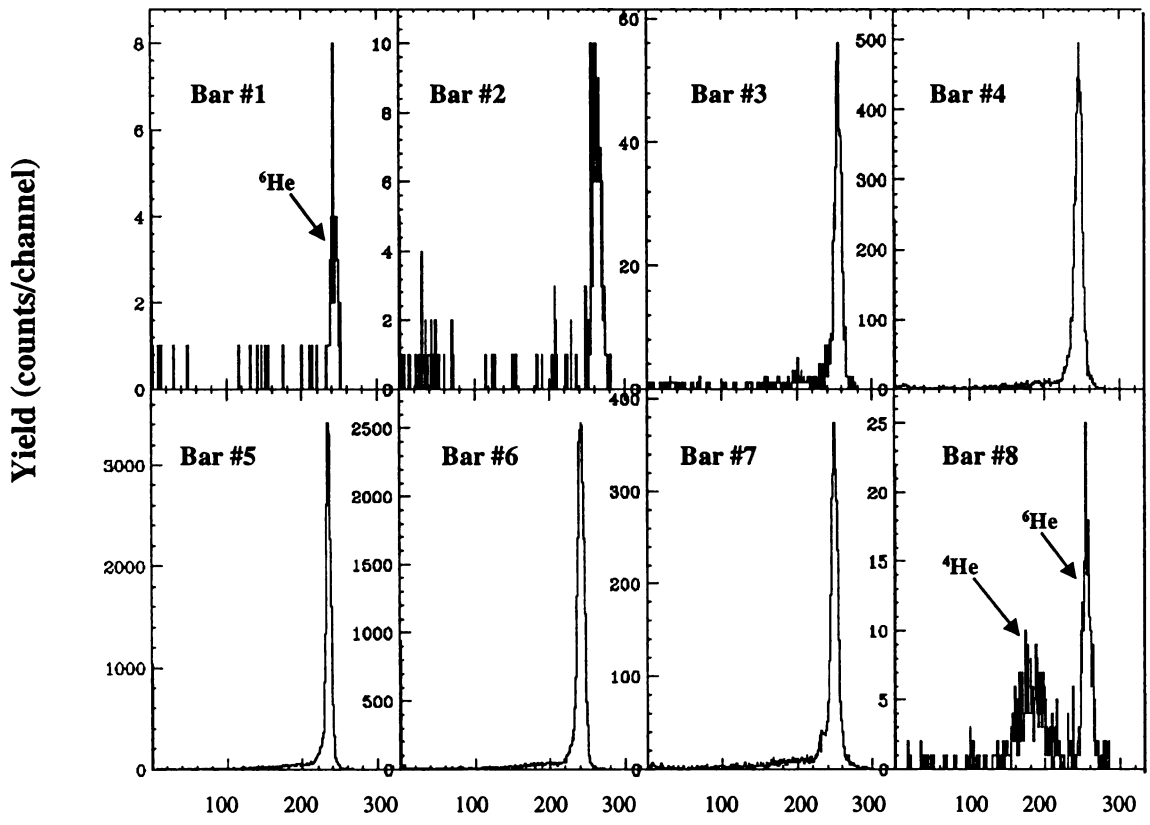

Figure 3.1. 3 The light ouput for the eight scintillator bars close to the beamline. The data were taken with a 25 MeV/u ^{6}He beam incident on a U target. Most of the beam hit bars #5 and #6. A number of ^{4}He particles produced in the target start to appear in Bar #8.

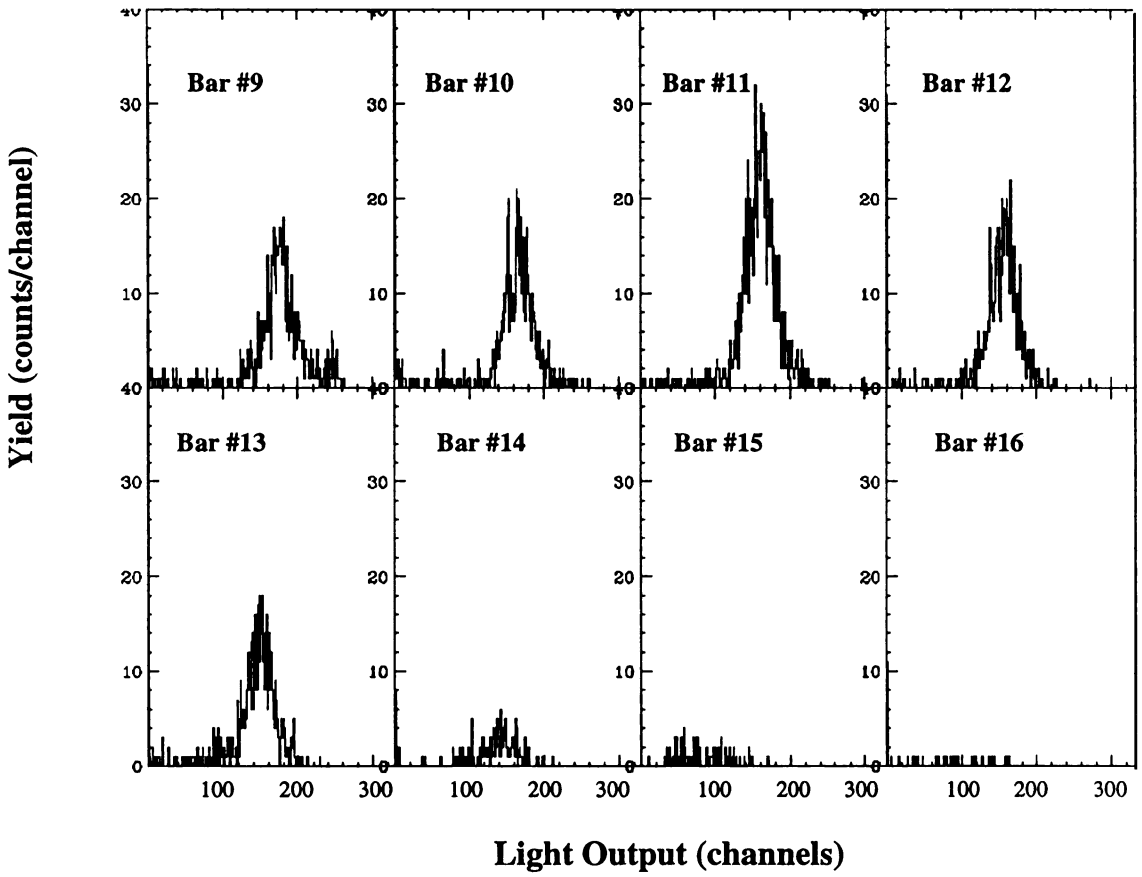

Figure 3.1.4 The light ouput for the eight scintillator bars far from the beamline. Almost all the ^{4}He produced in the target were swept by the magnet to the eight bars and bar #7 shown in Fig. 3.1.3.

3.1.2 n-γ Discrimination

The pulse-shape-discrimination (PSD) capability of the neutron walls enables us to separate neutrons from γ rays (See [32], [38] for details). A brief description is given below. A neutron is detected mainly through a recoil proton that has scattered the neutron. Gamma rays are detected by Compton scattering on electrons. The ionization of the scintillator by protons and electrons generates light. For a majority of organic scintillators, the light yield curve consists of a fast component and a slow component. The two components are the results of prompt fluorescence and delayed fluorescence in the scintillator molecules. The gamma-ray-induced electrons generate a larger fraction of their scintillation light in the fast component of the light yield curve as compared with the neutron-induced recoil protons, hence producing different pulse shapes. A special n-γ discrimination circuit was built for the scintillator cells of the neutron walls. The input of the circuit is the anode signal. The outputs of the circuit are "Fast", "Total", "Attenuated Fast" and "Attenuated Total". "Fast" is proportional to the fast component of the signal. "Total" is proportional to the total charge of the signal. In order to cover a large dynamic range of pulse heights in the experiment, the "Fast" output and the "Total" output were attenuated by a factor of 4. The attenuated "Fast" and "Total" signals are labeled as "Attenuated Fast" and "Attenuated Total" respectively. In the top spectrum of Fig. 3.1.5, the y-axis is the "Fast", and the x-axis is the "Total". The spectrum is for one of the 32 cells of the neutron walls used in the experiment. These events were taken with a Pu-Be source placed next to the neutron walls. The upper branch is from cosmic rays and gamma rays. The lower one is from neutrons. The bottom spectrum of Fig. 3.1.5 shows the data taken during the ^{6}He runs for the same cell except that the x and y axes are for

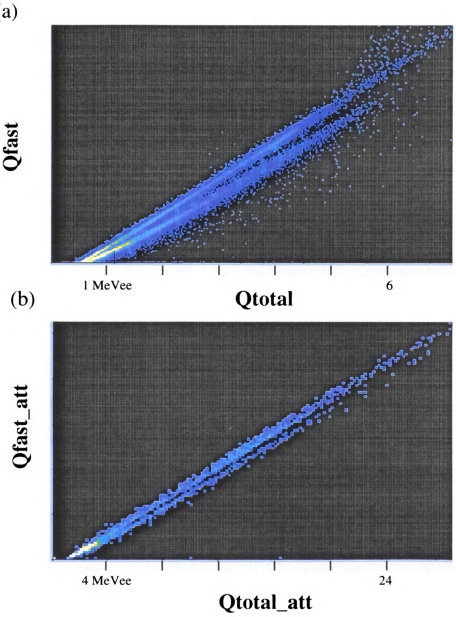

Figure 3.1.5 The n-γ discrimination spectra. The top branches are γ and cosmic rays. The bottom ones are neutrons. (a) The "Fast" signal versus the "Total" signal. The data were taken with a Pu-Be source. (b) The attenuated "Fast" signal versus the attenuated "Total" signal. The attenuation factor is 4. The data were taken with a ^{6}He beam.

attenuated light outputs. To select neutrons with pulse heights less than 6 MeVee (1 MeVee is the light output by a 1-MeV electron), a contour was drawn around the lower branch of the top spectrum for each cell. Any event inside the contour is considered a neutron event. For neutrons with pulse heights greater than 6 MeVee, a straight line was drawn between the two branches in the attenuated spectrum (Fig. 3.1.5 (b)). Any event below the line is considered a neutron event.

3.1.3 n-^{4}He Coincidence Data

Fig. 3.1.6 shows the summed energy spectrum of the ^{4}He fragments in coincidence with the neutron walls for the U target. These are the events detected in bars from bar 8 to bar 16. As shown in the figure, some other fragments, such as ^{3}H and ^{3}He, form the tail on the left side of the ^{4}He peak. There also is a small ^{6}He peak on the right side of the ^{4}He peak as a result of the coincidence between the ^{6}He and some gamma rays produced in the scintillator array. A gate was drawn to select the ^{4}He. There are factors making the number of the detected n-^{4}He events—N', less than from the number of ^{4}He produced in the target—N. One factor is the detection efficiency of the neutron walls for the neutrons—$\epsilon<1$. The detection efficiency of the scintillator bars should be 100%. The other factor is the system's solid-angle acceptance for the neutrons Ω_n and for the ^{4}He Ω_α from the target. The geometry of the field, poles and coils of the magnet and of the vacuum chamber makes knowledge of the energy dependent Ω_α impossible to know with any accuracy. Instead, we write

$$N' = N \bullet \varepsilon \bullet \Omega_n \bullet \Omega_\alpha = N \bullet f \qquad (3.1.2)$$

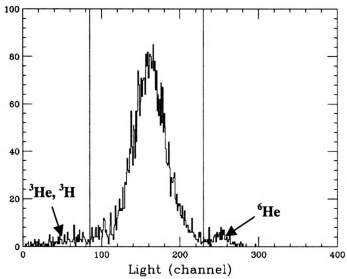

Figure 3.1.6 Light output distribution for coincidence events detected on bars from #8 to #16 for the U target. The solid gate was used to select the ^{4}He fragment. The tail on the left side of the ^{4}He peak is formed by other light fragments such as ^{3}H and ^{3}He. The small peak on the right side of the gate is formed by some ^{6}He particles.

Energy (MeV/u)	σ_{2n} (barn)
$0.0 \rightarrow 13.7$	0.41 ± 0.10
$13.7 \rightarrow 29.0$	0.47 ± 0.06
$29.0 \rightarrow 39.5$	0.47 ± 0.05
$39.5 \rightarrow 48.1$	0.40 ± 0.04
$48.1 \rightarrow 55.6$	0.35 ± 0.15

Table 3.1. 1 Measured 2n removal cross sections on Si for ^{6}He from ref. [17]. These data were used for the normalization.

Then

$$N = N'/f \qquad (3.1.3)$$

To determine the factor f, we normalized our Al data to the 2n removal cross section of ^{6}He on a Si target measured by Warner et al. [17]. Table 3.1.1 lists the measured cross sections for ^{6}He at various energies from ref. [17]. We took the cross section for the energy range 13.7-29.0 MeV/u, $\sigma_{2n}(Si) = 0.47 \pm 0.06b$, since the average energy of the ^{6}He beam in the middle of the targets (~24 MeV/u) is in the above energy range. We took the approximation that the cross-section for Al—$\sigma_{2n}(Al)$ is the same as that for Si. This normalization gives f = 0.0648. To see if this normalization factor makes sense, we want to know the values ε, Ω_n and Ω_α. From chapter 2, we know that the neutron detection efficiency for one neutron wall is 11% at 25 MeV/u. The two walls, with the way they were set up in the experiment (refer to chapter 2), have a detection efficiency around 18%, i.e. ε = 0.18. As shown in Fig. 3.3.2, the solid-angle acceptance Ω_n of the detection system as a function of the decay energy for ^{6}He is calculated. The average Ω_n for Al is about 0.35 at 1.5 MeV that is where the measured ^{6}He decay energy for Al concentrates, as shown later in Fig. 3.3.1. If Ω_α is not much less than 1, $f = \varepsilon \bullet \Omega_n \bullet \Omega_\alpha = 0.063$, which is consistent with the value obtained from the normalization. The 2n removal cross-sections for all the other five targets were calculated with the same f. The results are listed in the second column, the column labeled σ_{2n}, of Table 3.1.2. The errors due to statistical fluctuation are put next to the measured cross-sections.

Target	σ_{2n} (barn)	σ_{2n}' (barn)	Warner [30] (barn)	Ferreira et al. [37] (barn)
U	1.87 ± 0.24	1.38± 0.18	1.68	
Pb	1.70 ± 0.22	1.25± 0.16	1.51	1.80
Sn	1.22 ± 0.16	0.95± 0.12	0.91	
Cu	0.82 ± 0.10	0.72± 0.09	0.62	0.89
Al	0.47 ± 0.06	0.47± 0.06	0.45	
C	0.36 ± 0.05	0.39± 0.05	0.34	0.46

Table 3.1. 2 2n removal cross sections in the experiment. σ_{2n} is the measured cross section assuming constant neutron multiplicity. σ_{2n}' is the measured cross section adjusted for neutron multiplicity [40,41]. The calculated cross sections are from refs. [30] and [37].

Target	Multiplicity
C	1.3
Al	1.4
Cu	1.6
Sn	1.8
Pb	1.9
U	1.9

Table 3.1. 3 Neutron multiplicity for the six targets [40].

It is an approximation that the detection system has the same efficiency factor f for all the six targets. The approximation could cause a systematic error in the measured cross sections because we are actually assuming that the neutron multiplicity for the six targets is the same. According to a model developed by Barranco et al. [40,41], there are three reaction mechanisms responsible for the ^{6}He breakup: coulomb breakup, diffraction breakup and stripping. Two neutrons are produced and available for detection in coulomb and diffraction breakups, whereas only one neutron is detectable in stripping breakups. Since the coulomb reaction becomes the dominant breakup mechanism for the high Z targets, neutron multiplicity is expected to increase with charge Z. The calculated neutron multiplicity [40] for the six targets ranges from 1.3 for C to 1.9 for U, as listed in Table 3.1.3. The 2n removal cross sections adjusted for the neutron multiplicity (σ_{2n}') are shown in Table 3.1.3. The adjustment is more significant for the high-Z targets than for the low Z targets. For targets heavier than Al the unadjusted cross section is larger than the adjusted one, and for C, it is smaller. For example, for U, σ_{2n} = (1.87±0.24) b vs. σ_{2n}' = (1.38±0.18) b, for C, σ_{2n} = (0.36±0.05) b vs. σ_{2n}' = (0.39±0.05) b. One has to be careful about adjusting the cross sections for the varying multiplicity because the solid-angle acceptance of our detection system may change the measured multiplicity. For example, even though a coulomb breakup generates two neutrons, one neutron may go to the neutron walls and the other one may miss the walls, and this is more likely for a high Z target, such as U, than for a low Z target, such as C. The reason is that strong coulomb deflection is involved in many breakups for the high Z targets since the breakups can only occur when ^{6}He is close enough to the target. When a ^{6}He nucleus breaks up on U, it may have been deflected from its incident direction, which is assumed to be

perpendicular to the neutron walls. In an extreme case in which one neutron recoils against the other neutron and the ^{4}He, the first neutron may come out with such a large angle to the incident direction that it may just miss the wall or hit the magnet poles. On the other hand, the second neutron may come out aiming right at the neutron walls. The effect causes the measured multiplicity for the U target to be lower. Therefore the difference between the measured neutron multiplicity for the U target and that for the C target may not be as big as the theory predicts (1.9 vs. 1.3).

The experimental cross sections with and without the adjustment for the neutron multiplicity are compared with two theoretical calculations in Table 3.1.2. The calculation by Warner [35] follows closely that by Bertsch et al. [36] for ^{11}Li using the microscopic independent-particle model. In microscopic theories, the matter densities in two colliding nuclei and the nucleon-nucleon total cross section are two important input factors. The calculation is described in detail in the paper [35]. The result given by Ferreira et al. [30] is quite different. Most of the difference comes from the calculation of the nuclear cross section, since Warner used the same model as Ferreira et al. to obtain the coulomb cross section. One factor accouting for the difference is that they use different rms radii in their codes. Another factor, pointed out by Warner, is that Ferreira et al. did not consider core survival while calculating halo disintegration. We note that the ^{6}He energy in Warner's calculations is 24 MeV/u [37], which is our beam energy, while the energy in Ferreira et al. is 30 MeV/u. Warner's calculation is probably the better one for comparison with our data.

3.1.4 Coulomb Contribution

One of the purposes of using both light and heavy targets in the experiment is to separate the coulomb contribution from the nuclear contribution to the 2n removal cross section. The significance of disentangling the two is that it can help people further understand the nature of halo nuclei. Because the unadjusted cross sections better agree with Warner's calculation for the heavy targets (U, Pb) where the coulomb breakup is a major contributor, we use the unadjusted cross sections for the coulomb extrapolation.

In this section, two methods will be introduced to extract the coulomb contribution. The first method is by extrapolation. For light targets nuclear dissociation is dominant. An extrapolation of the nuclear cross section to the heavier targets is shown in Fig. 3.1.7. To make the extrapolation possible, we assume that 1) only the nuclear interaction contributes to the ^{6}He breakup on the C and Al targets; 2) if A is the mass number of a target nucleus, the nuclear 2n removal cross section is proportional to $A^{1/3}$, i.e., proportional to the radius of the target. So, the extrapolating line is expressed by

$$\sigma_{nuclear} = a + bA^{1/3} \qquad (3.1.4)$$

where a and b are two parameters to be determined. If the extrapolation relies only on two points, C and Al, it may result in a large uncertainty. So, the third point at $A = 0$ is deduced. This point is the nuclear cross section as the target nucleus gets infinitely small. We know that ^{6}He consist of a hard ^{4}He core and a neutron halo [40] formed by two valence neutrons. In a classical picture, we assume the 2n removal cross section results from a peripheral collision. In the collision the neutron halo is broken by striking the

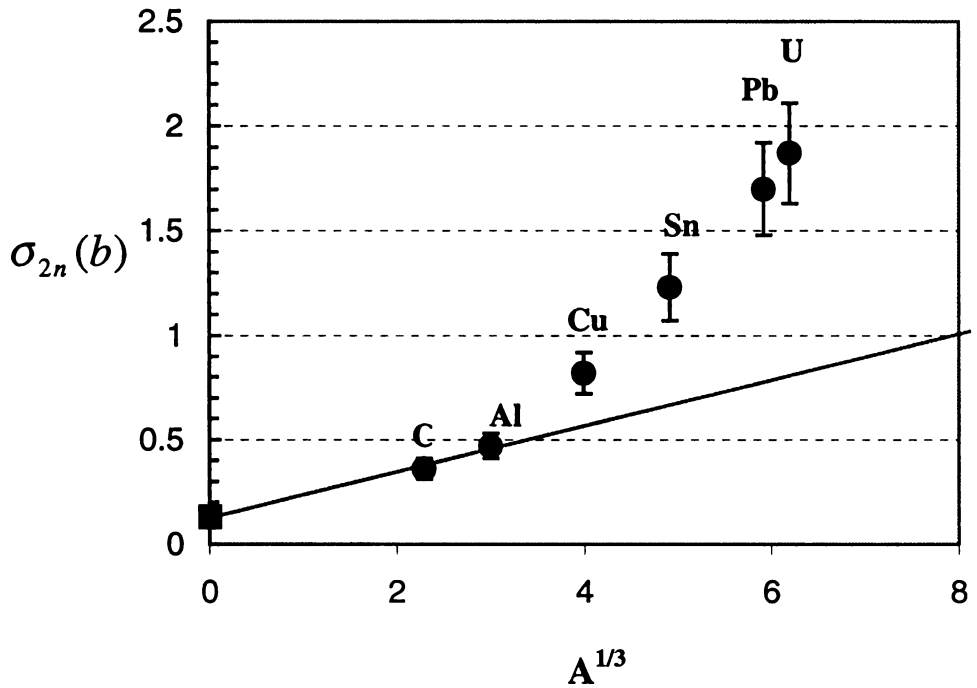

Figure 3.1.7 Total 2n removal cross sections for the six targets. The solid line is a simple model (eq. 3.1.4) to extrapolate the nuclear parts of the cross sections for the high Z targets. The results are listed in Table 3.1.4

infinitely small nucleus, leaving the core untouched. If the core is hit, reactions other than 2n breakup occur. So, the cross-section could be written as the area of the halo. The thickness of the neutron halo was measured to be 0.87 fm [38]. Using the measured radius of ^{6}He—2.33 fm [38], we get

$$\sigma_{nuclear}(A=0) \approx 2\pi \times R(^6He) \times 0.87$$

$$= 0.13(b) \qquad (3.1.5)$$

In Fig. 3.1.7, the straight line is the fitting result of the first three points (A=0,12,27),

$$\sigma_{nuclear} = 0.1257 + 0.1102A^{1/3} \qquad (3.1.6)$$

The difference between the points and the line is considered to be the coulomb part of the cross-section. The coulomb 2n cross section from the extrapolation is listed in Table 3.1.4 and plotted in Fig. 3.1.8. The solid curve is the calculation by Warner.

The second method used to separate the coulomb contribution from the nuclear contribution is to use the expected dependency of coulomb dissociation on target charge, $Z^{1.8}$. The coulomb cross section of ^{6}He depends on the strength of the coulomb field of the target, i.e., on the intensity of the equivalent photons surrounding the target nucleus as expressed in eq. (1.5.1), so $\sigma_{coulomb}(Z,E_\gamma) \propto n_{E1}(Z,E_\gamma)$. If one carefully compares $n_{E1}(Z,E_\gamma)$ in Fig. 1.1 for the six targets in the region where the dipole strength function is supposed to concentrate (~2-3MeV), one finds the relationship between photon number $n_{E1}(Z,E_\gamma)$ and target charge Z very close to $n_{E1}(Z,E_\gamma) \propto Z^{1.8}$. If we simply assume the nuclear cross section to be proportional to $A^{1/3}$, then we can express the total 2-n removal cross section as

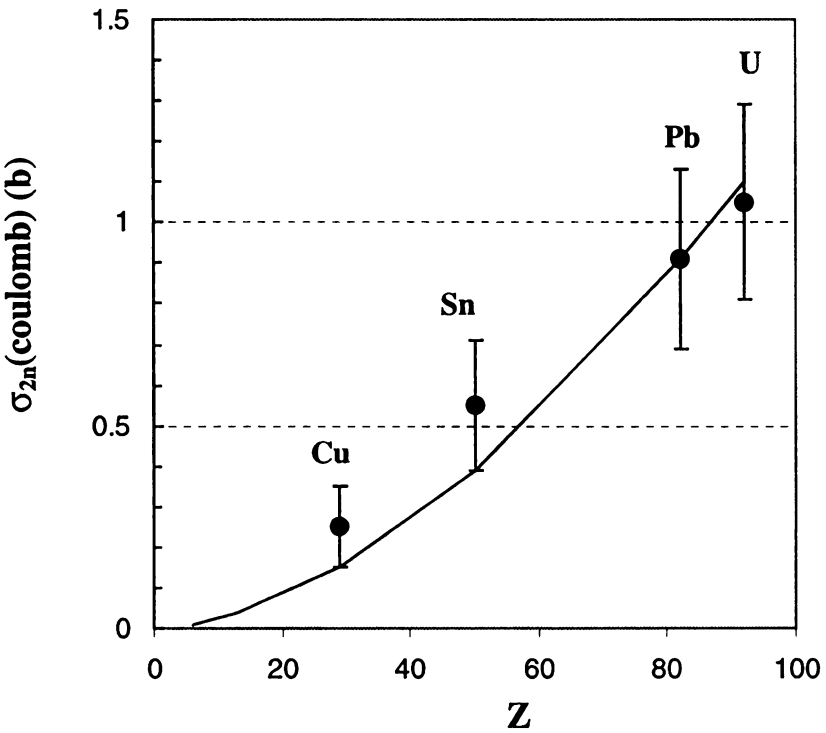

Figure 3.1. 8 Coulomb dissociation cross sections of ^{6}He for the four targets. The data points are the results of the extrapolation shown in Fig. 3.1.7. The solid line is the theoretical calculations by Warner [35,37].

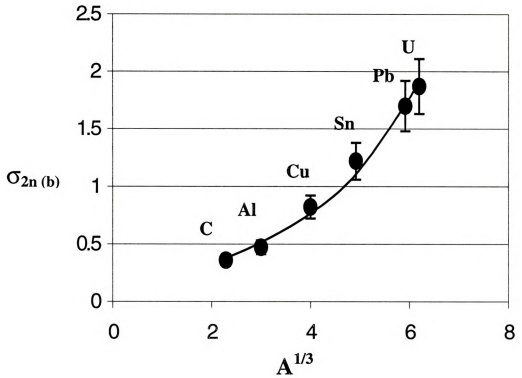

Figure 3.1.9 Total 2n removal cross sections for the six targets. The points are the experimental data. The solid curve is a fitting model to extract the coulomb part of the cross section (eq. 3.1.7). The results are listed in Table 3.1.4.

Target	Method 1 (barn)	Method 2 (barn)	Warner (barn)
U	1.06 ± 0.24	0.92± 0.24	1.10
Pb	0.92 ± 0.22	0.75± 0.22	0.91
Sn	0.56 ± 0.16	0.31± 0.16	0.39
Cu	0.25 ± 0.10	0.12± 0.10	0.15
Al	-	0.03± 0.06	0.04
C	-	0.01± 0.05	0.01

Table 3.1. 4 Coulomb 2n removal cross sections by the extrapolation described in the text. The calculated cross sections are from Warner [35,37].

$$\sigma_{2n} = \sigma_{nuclear} + \sigma_{coulomb} = aA^{1/3} + bZ^{1.8} \qquad (3.1.7)$$

The best fit of the data is shown in Fig. 3.1.9 with $a = 0.1625 \pm 0.0089$, $b = (2.692 \pm 0.294) \times 10^{-4}$. The coulomb cross section

$$\sigma_{coulomb} = 2.692 \times 10^{-4} Z^{1.8} \qquad (3.1.8)$$

is also listed in Table 3.1.4. The coulomb cross sections obtained by method 2 are smaller than those by method 1 and the calculations by Warner excluding. It also can be observed that for U and Pb, the coulomb effect contributes about half to the total 2-n removal cross section of ^{6}He.

3.2 Parallel Momentum Distributions

3.2.1 *Why parallel momentum distributions*

Other than reaction cross sections, the momentum distributions of nuclear fragments from reactions of halo nuclei help us obtain more detailed information about the structure of neutron haloes. For example, momentum distributions may make it possible for us to determine the wave function of the valence neutrons removed in the reaction. The relation between the momentum distribution and the wave function of the valence neutrons was described in section 1.1.

In this kinematically complete experiment, the momentum of the neutrons and the momentum of the ^{4}He from the ^{6}He breakup were measured. Although the full momentum was measured in the experiment, the measured neutron and ^{4}He parallel momentum distributions are expected to better reflect the momentum function of the halo neutrons than the full neutron and ^{4}He momentum distributions, because the transverse parts of the full distributions are distorted due to the following reasons.

For neutron: The solid-angle acceptance of the neutron walls prevents us from detecting neutrons with large transverse momentum. Let's estimate how much the limitation is with the setup in this experiment. The first neutron wall, 2 meters wide and 5 meters from the target, has an opening angle of 0.2 radian on one side. With the above geometry, the average neutron momentum 210 MeV/c yields a transverse momentum of 42 MeV/c, which actually is the cut-off point for the neutron transverse momentum in this experiment. The geometric limitation obviously does not apply to the parallel

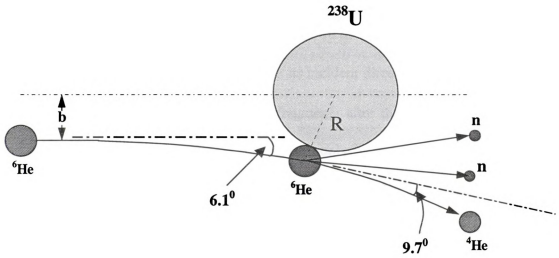

Figure 3.2.1 Breakup of ^{6}He into ^{4}He + n +n. The breakup occurs as the ^{6}He projetile touches the U nucleus. Both the ^{6}He projectile and the ^{4}He fragment are deflected by the coulomb force from the U nucleus.

momentum.

For ^{4}He: The coulomb deflection of the incident ^{6}He and the ^{4}He fragment by the target nucleus distorts the fragment momentum in the following way. The direction of the incident ^{6}He is measured by two PPACs before it enters the target. If the ^{6}He is deflected by the coulomb force as it approaches the target nucleus, the true direction of the ^{6}He right before the breakup is going to be different from the measured direction. In the extreme case as shown in Fig. 3.2.1, a ^{6}He breaks up as it just touches the U target nucleus. The ^{6}He would be deflected by 6.1° from its incident direction. If we assume that the decay energy shared by the fragments after the breakup is zero, the direction of ^{4}He after the breakup would be changed only by the coulomb force. The scattering angle of ^{4}He would be 9.7° after it breaks away from the ^{6}He. This leads to a total deflection of 15.8°. In this case, the true transverse momentum is zero because the decay energy is zero, but the measured one is obviously not. Coulomb deflection is expected to cause the transverse momentum distribution to be wider than it should be. To see how much the coulomb deflection effect could be, let's assume that the average deflection angle is half of the maximum value, i.e., 7.9^0. At 23 MeV/u, the momentum per nucleon is about 207 MeV/c. The coulomb deflection of 7.9^0 gives a ^{4}He transverse momentum $P_\perp$ (^{4}He) = 114 MeV/c. At the same time, if we use half of the ^{6}He deflection for the neutrons, i.e., 3^0, then the neutron transverse momentum $P_\perp$ (neutron) = 11 MeV/c. In the longitudinal direction, however, the change of the ^{4}He parallel momentum is only about 2 MeV/c with a 7.9^0 deflection. Compared to U, the effect of the coulomb deflection for C is much smaller because the maximum deflection angle is only about

5.5^0.

3.2.2 *Neutron Parallel Momentum Distributions*

To help compare different measurements it is desirable to characterize the distributions by parameters from simple statistical distributions. In Fig. 3.2.2, the neutron parallel momentum distributions are all fitted with a Gaussian function. The solid curves are the best fits. The widths of the parallel momentum distributions are represented by the σ of the Gaussian function. Graph (b) in Fig. 3.2.3 shows the values of the neutron parallel momentum distributions against Z of the targets in the experiment. Kobayashi et al. [9] measured the neutron transverse momentum distributions from ^{6}He fragmentation on C and Pb at 0.8 GeV/u. In their measurement, two components were found in the transverse momentum distributions. Their narrow component, which is thought to be the result of the removal of the valence neutrons in ^{6}He, is compared with the result of this experiment. The reported rms width (σ) of the narrow component of the neutron transverse momentum distribution, about 32 MeV/c for C, is somewhat larger than the width of (26.9±2.2) MeV/c for C measured in our experiment. For Pb, the measured width $\sigma \approx 31$ MeV/c by Kobayashi et al. is significantly larger than our result $\sigma \approx$ (19.8±1.2) MeV/c. The earlier discussion about the difference between the transverse momentum distributions and the parallel momentum distributions may explain the difference in the measured momentum widths.

It can be observed from Fig. 3.2.3 that the width of the neutron parallel momentum distribution decreases with the size of the target. For C, σ is (26.9±2.2)

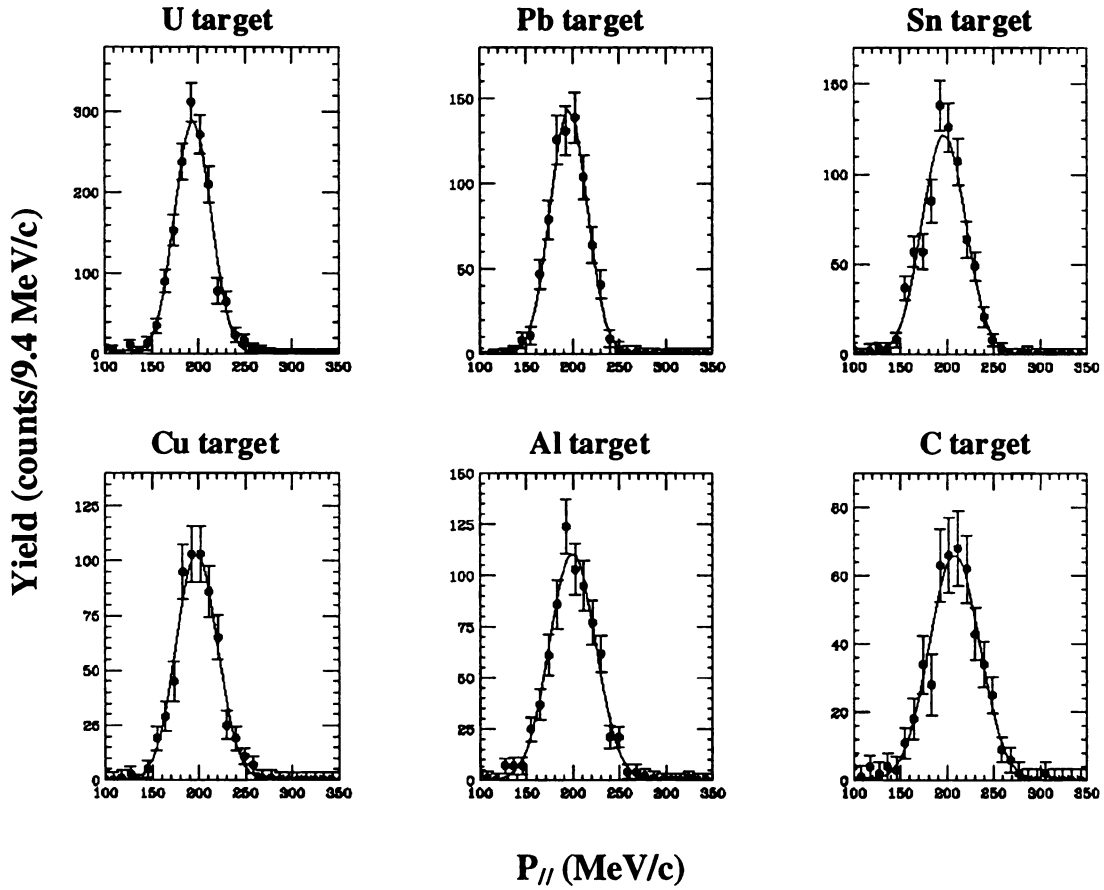

Figure 3.2.2 Neutron parallel momentum distributions for the ^{6}He breakup. The parallel momentum is the projection of the momentum on the incident direction of the ^{6}He beam. The solid curves are Gaussian fits. The widths of the distributions are listed in Table 3.2.1

(unit: MeV/c)

	U	Pb	Sn	Cu	Al	C
$\sigma_{P//}$ (^{4}He)	31.2±0.9	32.4±1.4	33.0±1.3	33.1±1.6	44.6±2.2	40.2±2.3
$\sigma_{P//}$ (n)	19.5±1.0	19.8±1.2	23.0±1.3	21.9±1.5	24.7±1.4	26.9±2.2

Table 3.2.1 The widths of the measured parallel momentum distributions

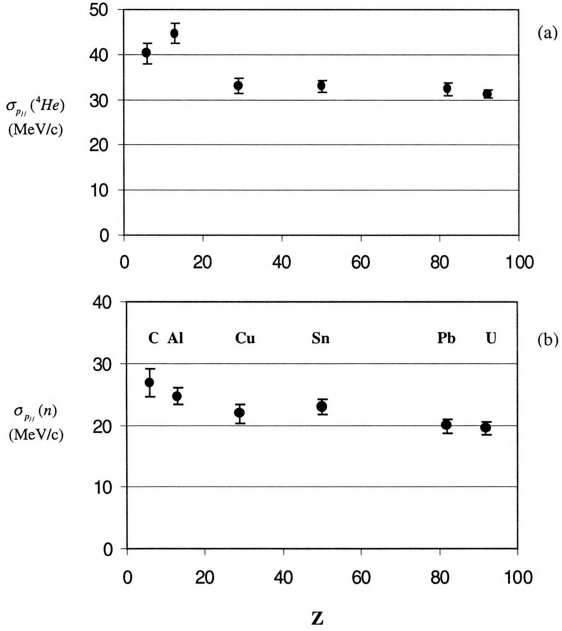

Figure 3.2. 3 (a) The widths of the ^{4}He parallel momentum distributions for the six targets. (b) The widths of the neutron parallel momentum distributions for the six targets.

MeV/c; for U, σ has decreased to (19.5±1.0) MeV/c. The change of the momentum width can be attributed to the following two factors:

1) The Serber model tells us that the fragment momentum distribution measures the momentum function of the fragment in the projectile. This model is based on the "sudden approximation." In this approximation, the target nucleus knocks the fragment out of the projectile in a very short time so that the fragment remains in the initial state until the instant of breakup. To qualify for a very short time, the interaction time between the target nucleus and the projectile has to be much smaller than the time for the fragment in the projectile to complete a full internal oscillation. In other words, it has to be a "snap shot" catching the moment of the action. If the interaction is too long, the Serber model breaks down because the initial state of the fragment can be changed. In our experiment, for the C target, almost all the ^{6}He breakups are due to nuclear interactions. Our beam velocity of c/4 and an interaction pathlength for the ^{6}He projectile of 11 fm (assumed to be twice the diameter of the C nucleus) yield an interaction time of about 44 fm/c. To estimate the period of the internal oscillation of a halo neutron, we note that a halo neutron has an rms radius of about 2.6 fm [38] and a momentum about 25 MeV/c in ^{6}He, hence a period of about 610 fm/c, about 14 times the interaction time. Therefore, the "sudden approximation" is valid in this case. If we go to heavy targets such as U, whose coulomb interactions with ^{6}He contribute more to the breakup than the nuclear interactions, the "sudden approximation" becomes less valid due to the long-range coulomb interaction. Because ^{6}He may well be disturbed before it breaks up, what we measure with the heavy targets may not as well reflect the internal momentum function of the ^{6}He. As a result, the momentum distribution could differ from the light targets to the

heavy ones.

2) The target-dependence of the width of the momentum distribution could also be the result of other reaction mechanism effects. For example, for light targets such as C, sequential breakup of ^{6}He via ^{5}He is thought to be the dominant process [14] because of the stripping mechanism, while for heavy targets such as U, simultaneous breakup of ^{6}He into ^{4}He and two neutrons dominates because of the coulomb breakup mechanism.

3.2.3 *^{4}He Parallel Momentum*

Figure 3.2.4 and Table 3.2.1 show the ^{4}He parallel momentum distribution for each of the six targets. Their width vs. Z of the target is plotted in part (a) of Fig. 3.2.3. The width of the ^{4}He parallel momentum distribution also shows a target dependence. The width for Al appears to be larger than the others. The big tail on the left side of the Al peak in Fig. 3.2.4 contributes to the abnormality. If the tail were ignored, the width of the distribution for Al would be in line with the trend in the target dependence.

3.2.4 *Valence Neutron rms Radius*

One purpose for measuring the ^{4}He fragment momentum distribution is to learn the wave function of the halo neutrons in the ^{6}He projectile. Although the direct linkage between the parallel momentum distribution and the wave function is a simplification, it can lead us to see a valence neutron distribution which extends far beyond the nuclear radius determined from $R=1.2A^{1/3}$ for normal nuclei. We can use the simple zero-range

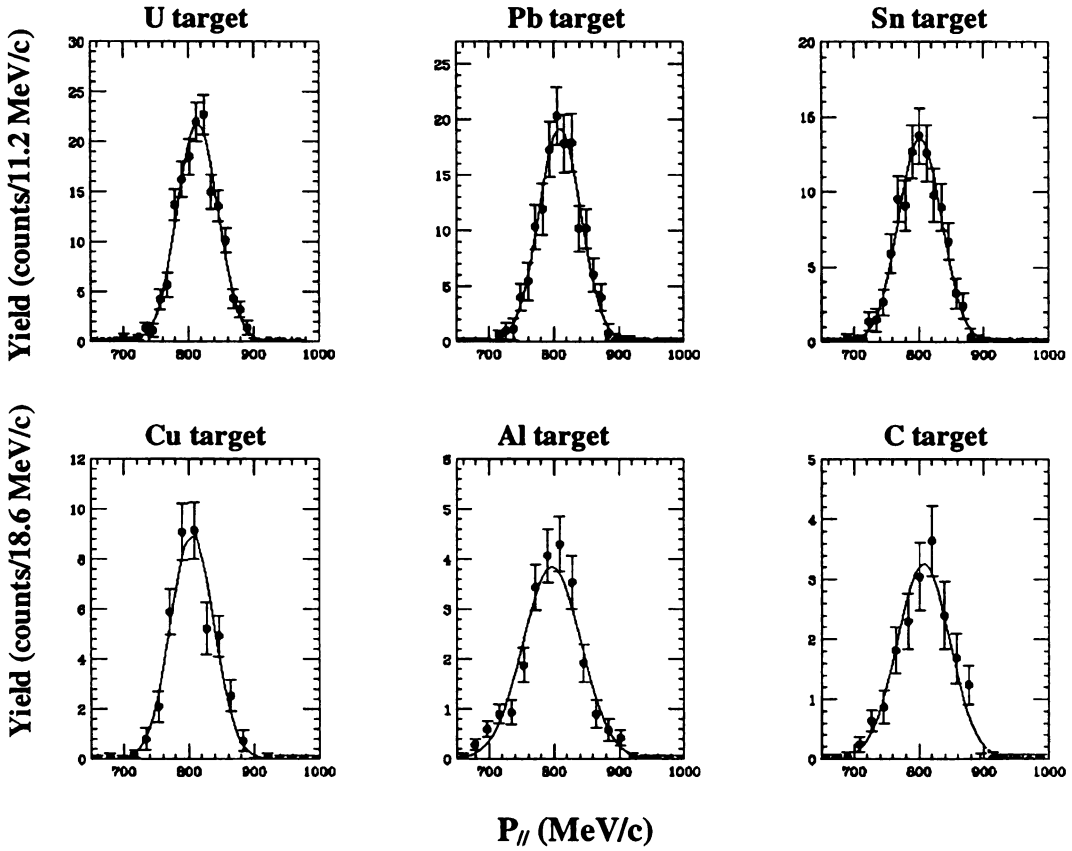

Figure 3.2.4 The ^{4}He parallel momentum distributions for the ^{6}He breakup. The parallel momentum is the projection of the momentum on the incident direction of the ^{6}He beam. The solid curves are Gaussian fits. The widths of the distributions are listed in Table 3.2.1.

Yukawa-type wave function first introduced by Hansen and Jonson [4] to obtain the asymptotic behavior of the wave function. This is the region with the most strength for peripheral reactions.

$$\psi(r) \propto \frac{1}{\sqrt{2\rho\pi}} \frac{e^{-r/\rho}}{r} \qquad (3.2.2)$$

where ρ is the range parameter, r is the radial distance between the ^{4}He core and the halo neutrons. After the Fourier transform of the spatial wave function, the momentum distribution becomes a Lorentzian

$$\frac{ds}{d\vec{p}} \propto \frac{\Gamma}{\left[\vec{p}^2 + \Gamma^2/4\right]^2}, \qquad (3.2.3)$$

where $\Gamma = \frac{2\hbar}{\rho}$. After integrating over the other two transverse dimensions, the parallel momentum distribution has the form

$$\frac{ds}{dp_{//}} \propto \frac{\Gamma}{\left[p_{//}^{\ 2} + \Gamma^2/4\right]}, \qquad (3.2.4)$$

with FWHM = Γ. If this distribution and a Gaussian distribution with the same FWHM are configured, they are almost identical in the central region. So, the width σ we obtained from Gaussian fitting can be used to estimate the size of the halo of ^{6}He using the rms halo radius $\langle r^2 \rangle^{\frac{1}{2}} \approx \frac{\rho}{\sqrt{2}}$. In the experiment, the width of the ^{4}He parallel momentum distribution depends on the target. We use the width for the C target, σ = 40.2±2.3 MeV/u (*FWHM* = 94.6±5.4 *MeV/c*), since it is expected to reflect the intrinsic momentum distribution of the halo better than the high Z targets, as explained earlier. For the C target,

$$\Gamma = FWHM = 94.6 \pm 5.4\, MeV/c \Rightarrow \rho = \frac{2\hbar}{\Gamma} = 4.17 \pm 0.24\, fm$$

$$\Rightarrow \langle r^2 \rangle^{\frac{1}{2}} \approx \frac{\rho}{\sqrt{2}} = 2.95 \pm 0.17\, fm. \qquad (3.2.5)$$

The rms radius of the neutron matter distribution was determined from ^{6}He interaction cross sections in two measurements which gave very close results: 2.59±0.04 fm [39] and 2.61±0.03 fm [44]. The rms radius determined from the ^{4}He parallel momentum distribution here reflects the tail of the valence neutron matter density, because the calculation is based upon an asymptotic wave function of the neutron halo. On the other hand, the rms radius determined in the two previous measurements reflects the entire neutron matter density of ^{6}He. Therefore, the rms radius determined here should be larger than the two reported results, by 0.35 fm according to this measurement. It is nice to see the consistency between the experimental results, considering that the model and the approach used above are simple.

3.3 The Decay Energy Distributions

One of the goals of this experiment was to look for possible evidences of the soft dipole resonance in ^{6}He. In section 1.5, we showed how to relate the dipole strength function $\frac{dB(E_1)}{dE}$ to the differential coulomb cross section $\frac{d\sigma^{E1}}{dE}$ by using the equivalent photon method. To obtain $\frac{dB(E_1)}{dE}$ for ^{6}He, we measured the decay energy distributions for the six targets. The decay energy E_d of ^{6}He is the difference between the excitation energy E_x and the 2-n separation energy S_{2n} of ^{6}He, i.e. $E_d = E_x - S_{2n}$. The decay energy of ^{6}He can be expressed as [10],

$$E_d = \frac{1}{2}\mu_1 \vec{V}_{2n-4}^2 + \frac{1}{2}\mu_2 \vec{V}_{n-n}^2 \qquad (3.3.1)$$

where $\mu_1 = \frac{m_4(2m_n)}{m_4 + 2m_n}$, $\mu_2 = \frac{m_n}{2}$, m_4 is the ^{4}He mass, m_n is the neutron mass, $\vec{V}_{2n-4}$ is the relative velocity between the ^{4}He and the center of mass of the two neutrons, $\vec{V}_{n-n}$ is the relative velocity between the two neutrons. The decay energy was calculated for each 2n-^{4}He coincident event. The measured decay energy distributions $\frac{d\sigma_m}{dE_d}$ for the six targets are shown in Fig. 3.3.1. The distributions were obtained after subtracting the target-out data from the target-in data in order to exclude the reactions in the Si strip detectors. A peak at around 1 MeV can be found in all the decay energy distributions. Before any conclusion can be drawn upon the raw differential cross sections, we have to know what are the constituents of the distributions and what are the complications coming from our detection system.

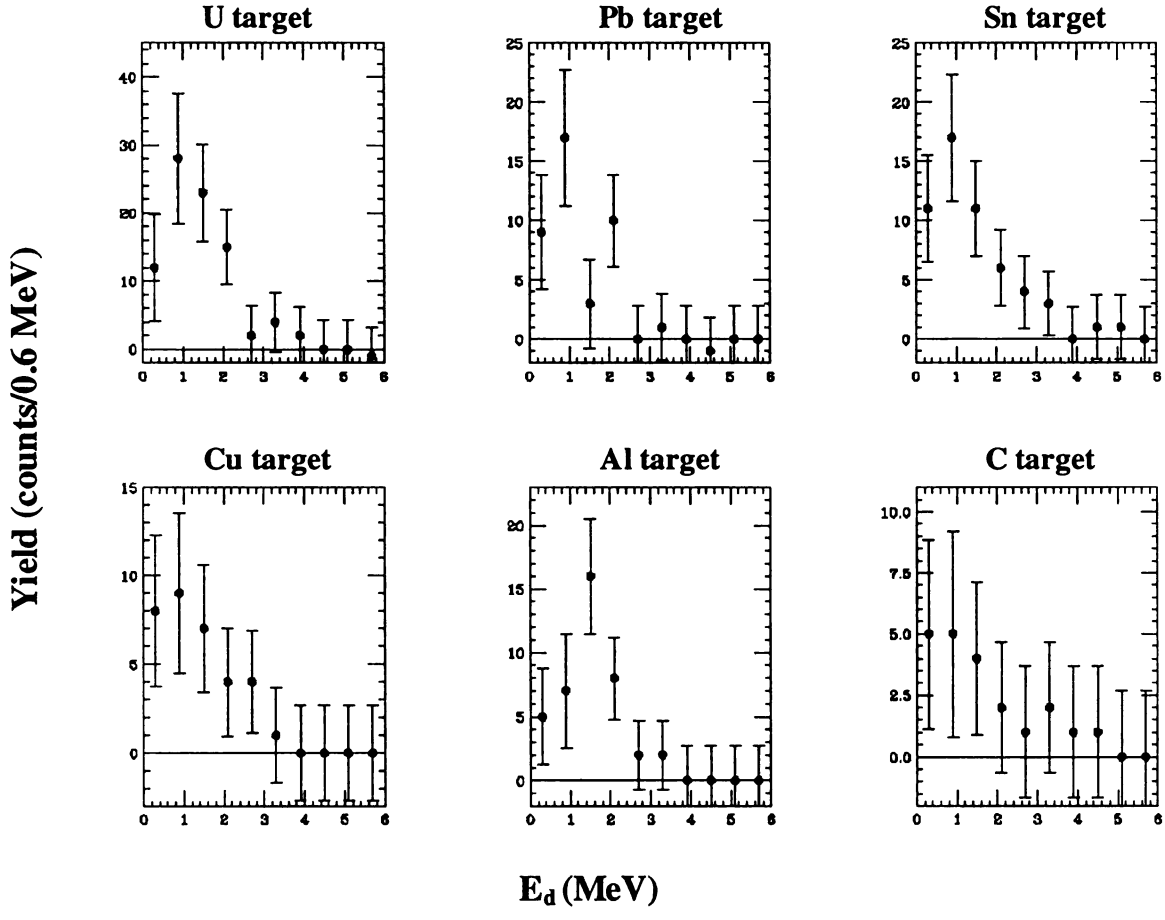

Figure 3.3.1 Decay energy distributions—$d\sigma_m/dE_d$ for the six targets. These are 2n-^{4}He oincidence events.

Since both nuclear and coulomb interactions contribute to the breakup of ^{6}He into two neutrons and a ^{4}He, the decay energy distributions in Fig. 3.3.1 are not pure coulomb differential cross sections. Because we are interested in electromagnetic dipole excitation, we want to exclude the nuclear part of the distributions. However, the small number of 2n-^{4}He events prevents us from making any valuable separation of the nuclear contribution. Fortunately, we think it is a good approximation to assume that only the coulomb breakup contributed to the decay energy spectrum for the U target. There are a couple of reasons supporting this approximation. First, based on the 2-n removal cross sections obtained in section 3.1, the coulomb interaction accounts for more than half of the total cross section for the U target. The nuclear cross section is about 40% of the total cross section according to our extrapolation. Second, the reaction mechanisms in nuclear breakups are diffraction and stripping. The diffraction produces events with two neutrons in the final state, while in the stripping process, because one neutron is absorbed by the target, only one neutron is observed. The requirement of two neutrons being detected in the decay energy spectra rules out the stripping mechanism. Because the stripping mechanism accounts for more than half of the nuclear breakups [40,41], the nuclear contribution to the decay energy distribution for the U target could be less than 20%, a rather small part of the spectrum. So, we do not expect the events from nuclear breakup to significantly affect the shape of the spectrum for the U target. As the contribution of the nuclear interactions increases from the heavy to the light targets, the approximation becomes less reliable.

Now, let's explain the complications caused by the detection system. The measured decay energy spectrum for the U target $\frac{d\sigma_m}{dE_d}$, shown in Fig. 3.3.1, is related to the true spectrum $\frac{d\sigma}{dE_d}$ by the following equation:

$$\frac{d\sigma_m}{dE_d}(E_d) = \int \frac{d\sigma}{dE_d'}(E_d')\varepsilon(E_d', E_d)dE_d' \qquad (3.3.2)$$

where $\varepsilon(E_d', E_d)$ is the response of the detection system that represents how much the detection system distorts the true decay energy spectrum. $\varepsilon(E_d', E_d)$ is a complicated function of neutron timing (σ_t = 1.27 ns) and angular resolution (σ_a = 0.4°), ^{4}He energy (σ_E = 2%) and angular resolution (1.2°), energy loss in the U target ($\overline{\Delta E}$ = 6.24 MeV) and multiple scattering effects, plus the solid angle acceptance of the neutron walls.

The solid-angle acceptance of the neutron walls was limited vertically (~ 1 meter) by the magnetic poles, horizontally (~ 2 meters) by the length of the cells. So the maximum vertical neutron angle with respect to the ^{6}He projectile direction was only 5.7°. In the horizontal direction, the maximum neutron angle was 11.3°. The decay energy distributions are affected by the solid-angle acceptance of the detection system. The higher the decay energy, the smaller the acceptance because large decay energy results in higher neutron transverse momentum, making the neutrons more likely to miss the neutron walls. With decay energies below 0.3 MeV, no neutron will miss the neutron walls because both neutrons have laboratory angles less than 5.7°. When the decay energy exceeds 0.3 MeV, some neutrons start to miss the wall in the vertical direction. In

an extreme mode, in which one neutron recoils against the other neutron and the ^{4}He, the first neutron will have the maximum velocity. The first neutron will just miss the neutron walls at E_d = 0.3 MeV if its momentum in the rest frame of the ^{6}He projectile is perpendicular to the pole faces of the magnet. When the decay energy is over 1.2 MeV, some neutrons start to miss the wall horizontally. Fig. 3.3.2 shows the calculated solid-angle acceptance vs. decay energy based on a Monte-Carlo simulation using the 3-body phase space distribution. The curve starts to fall around 0.3 MeV as predicted.

Because the response function is too complicated, it is not possible to unfold the response from $\frac{d\sigma_m}{dE_d}$ directly. So, models were chosen for $\frac{d\sigma}{dE_d}$. Each one of the models was filtered through the detection system using a Monte-Carlo simulation, and compared with the measured decay energy spectrum. The one that gave the best fit was considered the true decay energy spectrum. As shown in eq. 1.5.1, to obtain $\frac{d\sigma}{dE_d}$, we have to know the photonuclear cross section $\sigma_{E_1}(E)$. We used the empirical model parameterized with a Breit-Wigner function introduced in [10]

$$\sigma_{E_1}(E_d) = \frac{a\Gamma}{(E_d - E_0)^2 + (\Gamma/2)^2}, \qquad (3.3.3)$$

where

$$\Gamma(E_d) = \frac{\Gamma(E_0)T(E_d)}{T(E_0)}. \qquad (3.3.4)$$

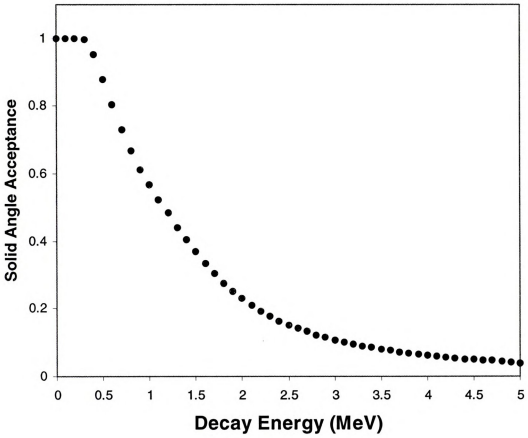

Figure 3.3.2 Calculated solid-angle acceptance of the detection system. The simulation is based on the 3-body phase space model.

In eq. 3.3.3, Γ is the width, E_0 is the resonance energy and a is a normalization factor. For ^{6}He, the excitation energy $E_x = E_d + 0.975\,\text{MeV}$. In eq. 3.3.4, $\Gamma(E_0)$ is the width at E_0, $T(E_d)$ is the transmission coefficient with the energy dependence of s-wave neutrons [45]. The energy dependence forces the Breit-Wigner function to be zero at zero decay energy. In Fig. 3.3.3a, the measured decay energy for the U target is shown again with a solid line that is the Breit-Wigner model with the resonance parameters E_0 = 1.9 MeV and $\Gamma(E_0) = 1.5$ MeV. Within statistical errors, the model gives a very good fit to the data. So, eq. 3.3.3 with the two best parameters is considered our measured photonuclear function $\sigma_{E_1}(E)$ for ^{6}He. The function is plotted in Fig. 3.3.3b. The corresponding dipole strength function, as shown in Fig. 3.3.3c, was determined from the photonuclear function $\sigma_{E_1}(E)$ based on eq. 1.5.4.

The dipole strength function is compared with two three-body models, as shown in Fig. 3.3.4. The model by Danilin et al. was first introduced in ref. [25] to look for the dipole resonance for ^{6}He. This model is based on hyperspherical harmonics and the coordinate space Faddeev approach [23]. The model was later used to calculated cross sections for coulomb dissociation of ^{6}He [30]. The dashed curve is the most recent calculation obtained from Ian Thompson, one of the collaborators in ref. [30]. In the other three-body model, by Pushkin et al.[46], the strength function for two-valence neutron halo nuclei is expressed as

$$\frac{dB(E1)}{dE} \propto \frac{E^3}{(S_{2n}^{eff} + E)^{\frac{11}{2}}} \qquad (3.3.5)$$

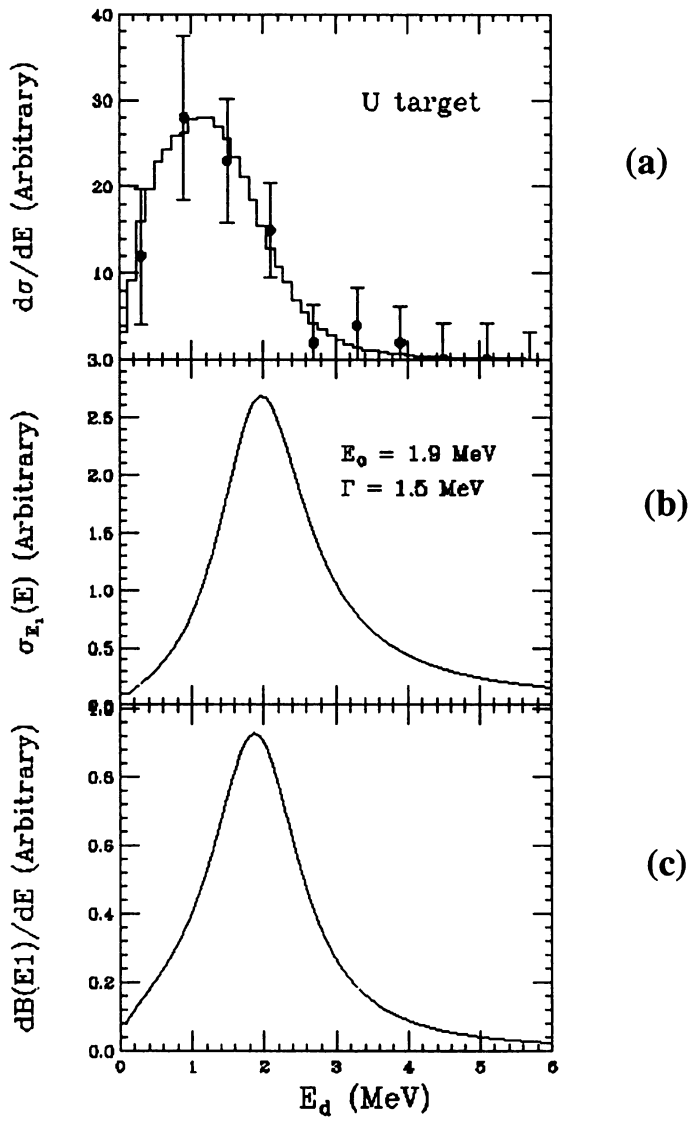

Figure 3.3.3 Decay energy spectrum for the U target. (a) The points are experimental data. The solid line is the result of a Monte Carlo simulation with a Breit-Wigner function (E_0 = 1.9 MeV and Γ = 1.5 MeV). (b) The photonuclear spectrum corresponding to the Breit-Wigner parameters determined from the data. (c) The dipole strength function determined from the data.

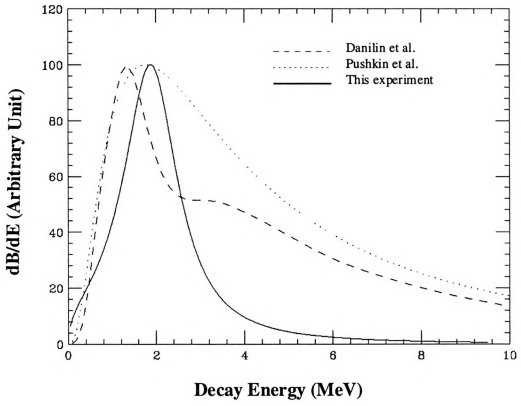

Figure 3.3.4 The dipole strength functions. The dashed curve and the dotted curve are from two 3-body models [25,46].

where $S_{2n}^{eff} = aS_{2n}$ is an effective separation energy with $a = 1.45 - 1.55$. The strength function for two-neutron halo nuclei is derived from the E1 strength function for one-neutron halo nuclei by Bertulani et al. [18]. The dotted curve in Fig. 3.3.4 is the result of the model with $a = 1.50$ and $S_{2n} = 0.975$ MeV. Even though the shapes of the strength functions differ quite a bit, they are very well concentrated in the area between 1.5 MeV and 2.0 MeV. Since excitation energy $E_x = E_0 + 0.975$ MeV, this may indicate a concentration of the dipole function between $E_x = 2.475$ MeV and $E_x = 2.975$ MeV.

We can further compare our data with another 3-body model using the coupled-rearrangement-channel method base on an $\alpha + n + n$ cluster model [28]. The calculated strength distribution had a broad peak at $E_x \approx 2.5$ MeV. The width of the peak predicted in the model is in the neighborhood of 4 MeV, which is very similar to the model by Pushkin et al. Some authors [25,28] in their papers thought that the broad widths did not support the existence of a resonance in ^{6}He. They call the peak a reminiscence of a resonance behavior since the soft dipole resonance is supposed to have a very narrow width ($\Gamma \leq 1$ MeV).

The experiment and the calculations agree that there is a strong concentration of the dipole strength at low energy $E_x \sim 3$ MeV. However, it is not clear whether the ^{6}He breakup occurs directly or through a resonance state if we base our judgement solely on the decay energy spectrum. We will look for further evidences in the following section.

3.4 Post-breakup Coulomb Acceleration

It remains as an interesting topic whether halo nuclei, such as ^{11}Li and ^{6}He, breakup in the coulomb field through a soft dipole resonance, or simply break directly into three pieces—two neutrons and a charged fragment. For ^{11}Li, the post-breakup coulomb acceleration (PBA) of the ^{9}Li fragment favored the direct breakup mechanism [10]. It is one of the goals of the experiment to find if PBA can be found in the ^{6}He breakup as well. First, let's briefly explain what is PBA using the ^{6}He projectile and the U target as an example.

Because of the great photon intensity, coulomb excitation is more likely to occur when the ^{6}He projectile is close to the U nucleus [10]. If the projectile decays immediately after being excited by the coulomb field, the two valence neutrons fly away with whatever velocity they have at the moment of the breakup because the neutrons do not feel the coulomb force. On the other hand, the ^{4}He would be accelerated as it leaves the coulomb field of the U nucleus. Since the decay energy is small relative to the incident energy of the ^{6}He, it cannot significantly alter the velocities of the fragments. Therefore, on average, the accelerated ^{4}He fragment tends to have a higher velocity than the neutrons if the direct breakup is the dominant mechanism. However, if it forms a resonance after being excited, the projectile will not break up until the resonance reaches the end of its lifetime. If the resonance lives long enough, the excited ^{6}He will travel far away from the U nucleus. As a result, the neutrons and the ^{4}He fragment will have about the same velocity because the coulomb field at the point of the breakup is too weak to have any effect on the ^{4}He fragment.

3.4.1 *Projectile Slow-down*

As we can see from the above, the premise for the post-breakup acceleration is that the ^{6}He projectile has to break up when it is close to the target nucleus. As the ^{6}He projectile approaches the target nucleus, it slows down when part of its kinetic energy transforms into potential energy. The closer the projectile is to the target nucleus, the more kinetic energy it loses, and the lower its velocity. It can be inferred that if the ^{6}He breaks up at a place close to the target nucleus, the average neutron energy should be lower than the incident beam energy per nucleon. The energy distributions of the neutrons from the ^{6}He 2-n removal reactions are shown in Fig. 3.4.1. These events were n-^{4}He coincidence events. The distributions were fitted with a Gaussian function. The centroids of the distributions give the average neutron energies. Fig. 3.4.2 shows the difference ΔE between the average neutron energies $\overline{E}_n$ and the average beam energies per nucleon $\overline{E}_{beam}$. The solid line connects points $\Delta E_{\max}$ for the maximum slow-down as the ^{6}He projectile grazes the target nucleus. If R_t and Z_t denotes the radius and the change of the target nucleus, respectively, $\Delta E_{\max}$ can be expressed by the potential energy at $R = R_{s_{He}} + R_t$,

$$\Delta E_{\max} = \left(\frac{Z_t Z_{s_{He}} e^2}{R} \right) \Big/ 6 \qquad (3.4.1)$$

where $R_{s_{He}} = 2.33 fm$, $R_t = 1.2\, A^{1/3}$. As shown in the figure, the ^{6}He projectile slows down more for the high Z targets because of the presence of stronger coulomb fields.

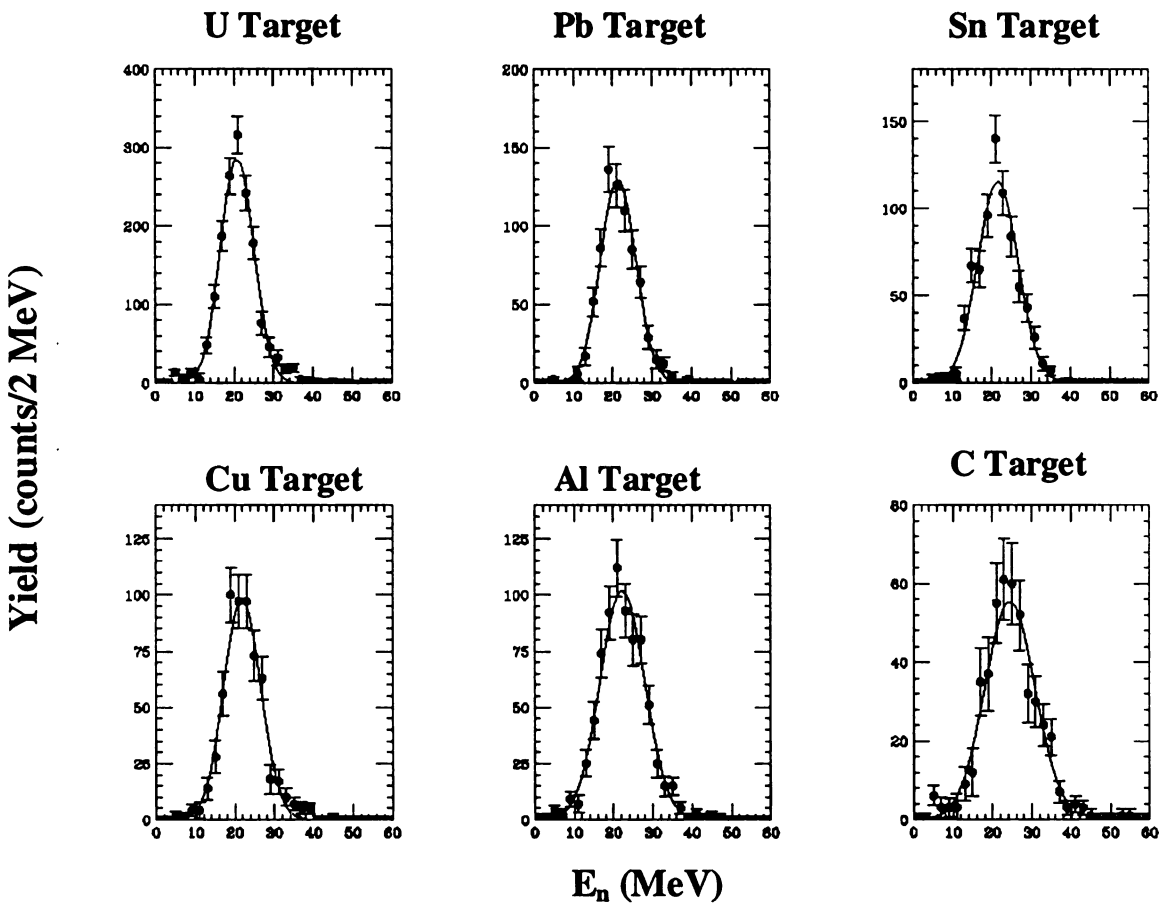

Figure 3.4.1 Neutron energy distributions for the ^{6}He breakup. The points are 1n-^{4}He coincidence events from the experiment. The solid lines are Gaussian fits.

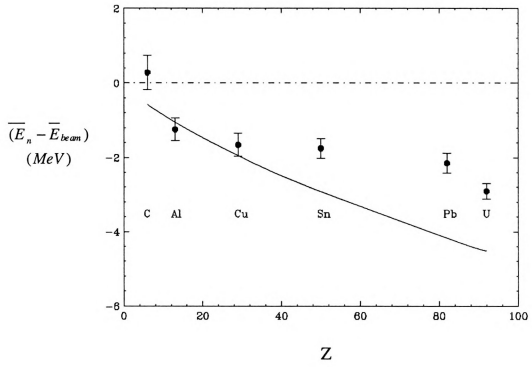

Figure 3.4.2 Difference between the average neutron energy and the average ^{6}He beam energy per nucleon. The average neutron energy is determined from the centroid of the Gaussian in Fig. 3.4.1. The average beam energy is equal to the beam energy at the center of the target. The solid line connects the maximum energy differences for the six targets.

Another observation is that the lower the Z of the target, the closer the slow-down is to the maximum. This indicates the dominance of the nuclear interactions for the low Z targets, interactions in which the ^{6}He projectile has to get very close to the low Z targets in order to acquire sufficient energy to induce a breakup.

3.4.2 Velocity Shift

Although the projectile slow-down proved that the breakup of ^{6}He occurs close to the target nucleus, it did not tell how the ^{6}He breaks up—direct or through a resonance state. We turned to the difference between the average the ^{4}He velocity and average neutron velocity for further evidence. For each 2n-^{4}He coincidence event, we determined the velocity for each neutron and the velocity for the ^{4}He fragment. To rule out the bias towards any one of the neutrons, we took the average of the velocities of the two neutrons. The top three graphs in Fig. 3.4.3 show the difference between the z-component of the ^{4}He velocity and that of the average velocity of the two neutrons for the three heavy targets—U, Pb, Sn. It will be explained later why only the z-component is used. The results for the light targets—Cu, Al, C are shown in the top three graphs in Fig. 3.4.4. The velocity difference is expressed relative to c, the velocity of light. One concern with the velocity difference between the neutrons and the ^{4}He fragment was that neutron and ^{4}He velocities were measured by different detectors in the experiment. Different responses of the detectors could cause a systematic shift in the velocity difference. This type of systematic error might lead us to a wrong conclusion. In order to see if a systematic shift exists in our detection system, we calculated the z-component of the center-of-mass velocity for the 2n+^{4}He system both before breakup and after breakup.

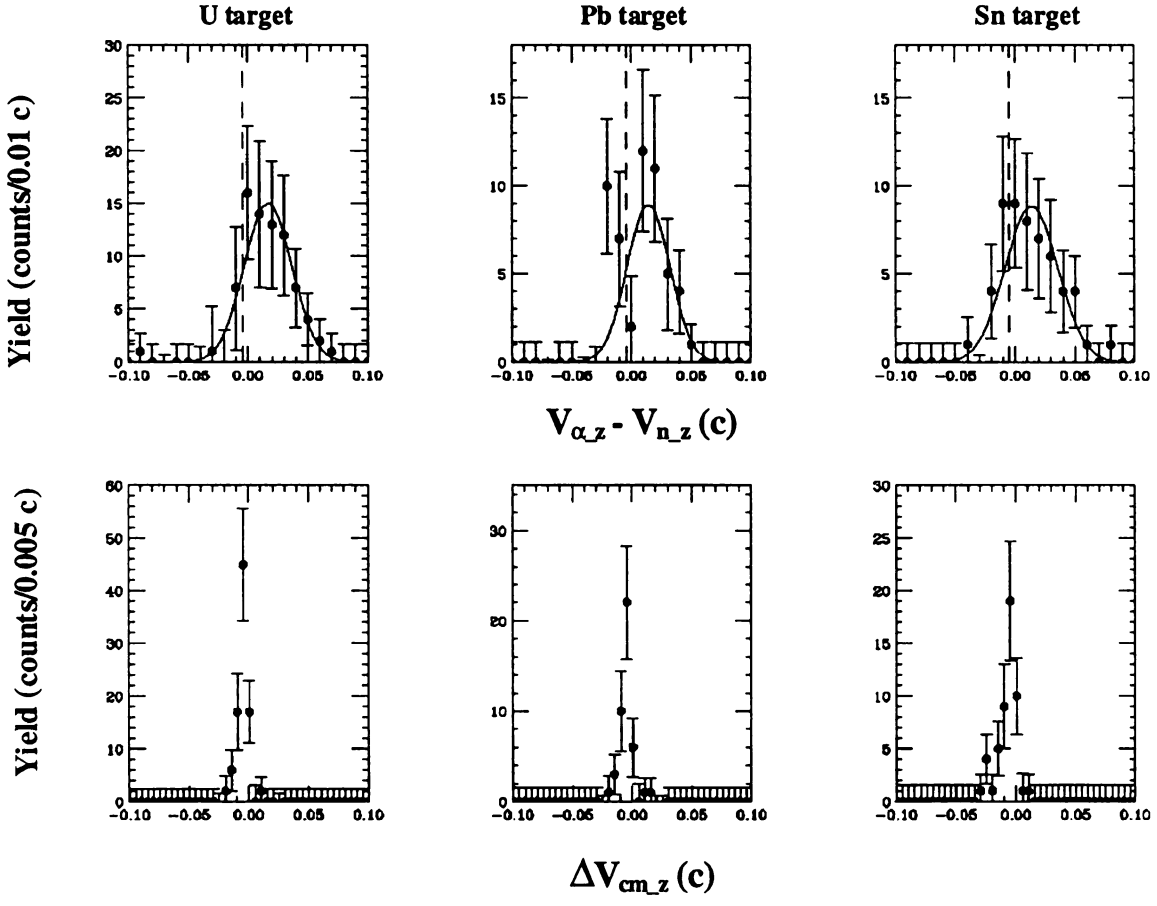

Figure 3.4.3 Velocity (z-component only) difference distributions for the three heavy targets in the expriment. The top three graphs are the differences between the ^{4}He velocity and the average velocity of the two neutrons, calculated on an event-by-event basis. The bottom three graphs are the differences between the ^{6}He center of mass velocity before breakup and after breakup for the same three targets, respectively. The dashed lines are the centroids of the bottom distributions.

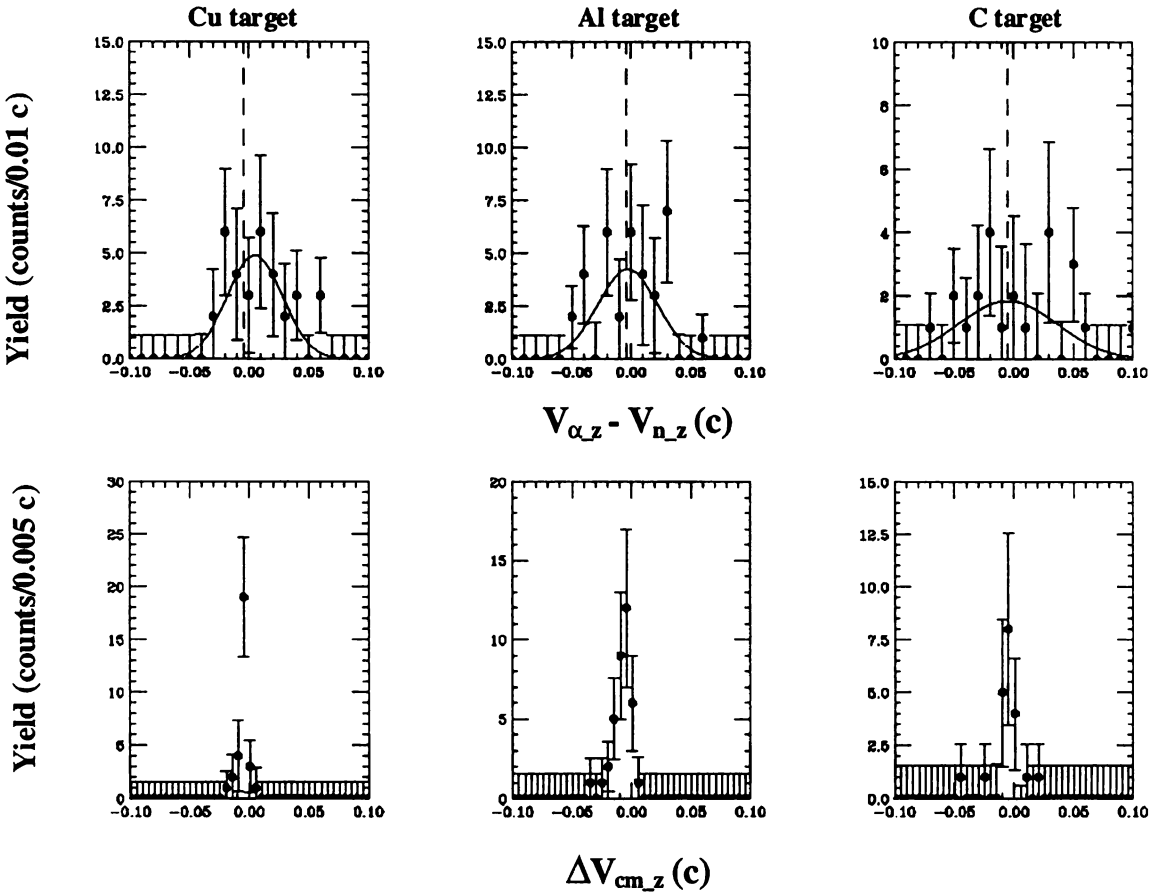

Figure 3.4.4 Velocity (z-component only) difference distributions for the three light targets in the expriment. The top three graphs are the differences between the ^{4}He velocity and the average velocity of the two neutrons, calculated on an event-by-event basis. The bottom three graphs are the differences between the ^{6}He center of mass velocity before breakup and that after breakup for the same three targets, respectively. The dashed lines are the centroids of the bottom distributions.

Before breakup, the center-of-mass velocity is determined from the incident beam energy at the center of the target. After breakup, the center-of-mass velocity is determined from the measured velocities of the two neutrons and the ^{4}He. Based on momentum conservation, the difference between the two velocities should center at zero if there is no systematic error with the measurements. It has to be pointed out that only the z-component can be used, because the center-of-mass velocity of the ^{6}He is changed in the transverse direction due to the interaction with the target nucleus. The z-component, on the other hand, remains the same since the target nucleus on average recoils at 90° to the z direction. Therefore, it is a good approximation to assume that the target nucleus gains zero momentum in the z direction after the impact. Based on momentum conservation, there should be no momentum change for the z component of the 2n + ^{4}He system before and after the interaction, i.e. the center-of-mass velocity difference should be zero. The graphs on the bottom in Figs. 3.4.3 and 3.4.4 show the center-of-mass velocity difference distributions for the six targets. Every peak in the graphs has a center at (-0.0045±0.0012) c. This indicates that there is a small systematic shift in the detection system. The vertical dashed lines in the top graphs indicate -0.0045 c. To account for the systematic shift, the velocity shift was measured from the centroid of the velocity difference distribution to the dashed line. The result is shown in Fig. 3.4.5. As shown in the figure, within the statistical uncertainty, the heavier targets produce a ^{4}He fragment with a higher velocity than the neutrons.

If a resonance state was formed, it would be meaningful to see how long the excited ^{6}He nucleus remained in the resonance state in order for the observed velocity

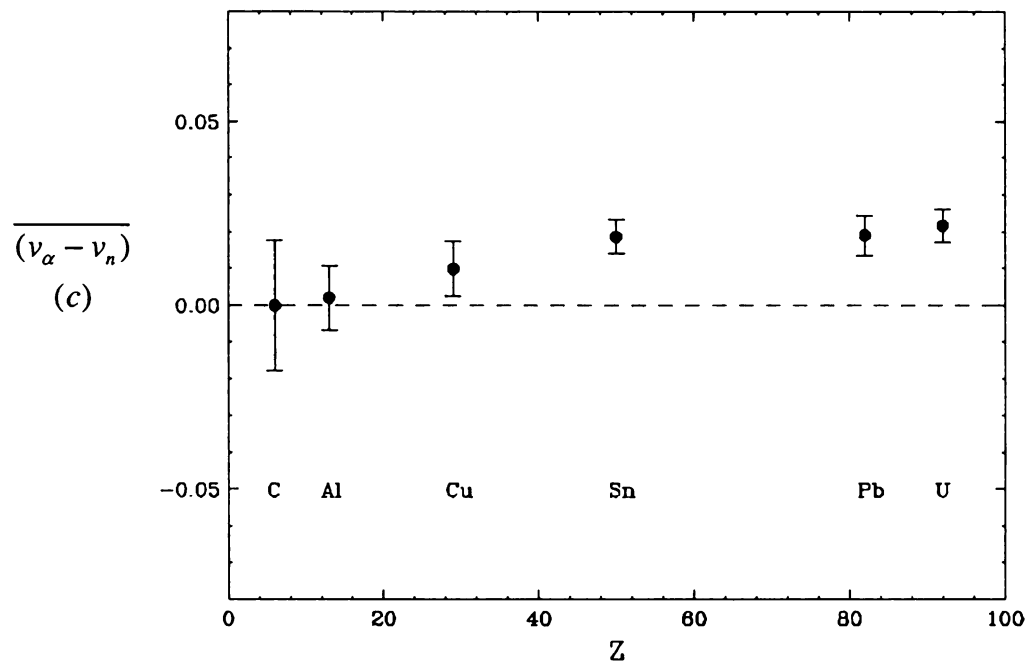

Figure 3.4. 5 Average velocity difference between the ^{4}He and the neutrons from the ^{6}He breakup. The data points are determined from the centroids of the top graphs in Figs. 3.4.3 and 3.4.4. The data are adjusted for the systematic shift (indicated by the dashed lines in those figures).

shifts to be produced. Obviously, the longer the lifetime, the smaller the velocity shift. Sackett et al. [10] showed how to calculate the lifetime of the resonance from the velocity shift. As shown in Fig. 3.4.6, simplified breakup schematics is used in the calculation. First, a straight-line trajectory is assumed, since the ^{6}He is only deflected by a few degrees. Second, the excitation occurs at the distance of closest approach, because the electric field is the most intense at that point. So, the ^{6}He is excited at point A, then breaks up at point B. To see the detailed deduction of the formula, please refer to ref. [10]. The relation between the average velocity shift and the mean lifetime is expressed as:

$$\langle \Delta V \rangle = \langle V_{4z}(\infty) - V_{2nz}(\infty) \rangle = \frac{Z_{He} Z_U e^2}{m_4 V} \frac{1}{\sqrt{b^2 + V^2 \tau^2}}, \qquad (3.4.2)$$

where $V_{4z}(\infty)$ and $V_{2nz}(\infty)$ are the z-component of the measured velocities for the ^{4}He and the two neutrons, respectively, V is the incident beam velocity, b is the impact parameter and τ is the mean lifetime of the resonance. For the U target, $\langle \Delta V \rangle = 0.0216 \pm 0.0045\,c$ and $V = 0.2260\,c$. If we use a small average impact parameter, b = R(^{6}He)+R(^{238}U) = 2.33 + 7.44 = 9.77 fm, based on eq. 3.4.2 the mean lifetime of the resonance is $\tau = 47 \pm 18 fm/c$, which yields a width of $\Gamma = 4.2 \pm 1.6 MeV$. This means that a resonance state has to have a width 4.2 MeV to be consistent with the measured velocity shift, which would be much larger than the $\Gamma = 1.5 MeV$ obtained from the decay energy spectrum in Fig. 3.3.3a. Based on the measured $\Gamma = 1.5 MeV$, the resonance should have a lifetime of about 131 fm/c. The velocity shift shows, however, that the ^{6}He projectile breaks up long before 131 fm/c. This means that the time is too short to form a

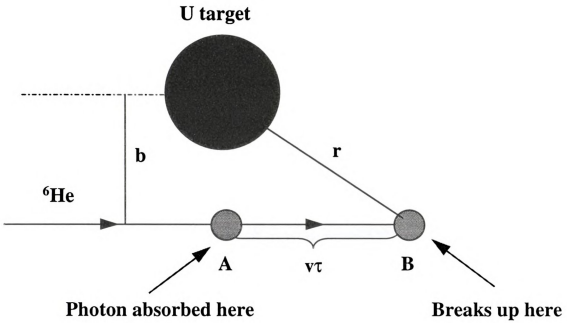

Figure 3.4. 6 Schematic view of a ^{6}He breakup. The impact parameter is denoted by b. The ^{6}He is excited at point A, the closest approach, then breaks up at point B. The distance between the U nucleus and point B is r, v is the beam velocity and τ is the mean lifetime of the resonance.

Target	U	Pb	Sn
$<\Delta V>/c$	0.0216±0.0045	0.0190±0.0055	0.0185±0.0046
τ (fm/c)	47±18	50.5±24	18.6±22
Target	**Cu**	**Al**	**C**
$<\Delta V>/c$	0.0098±0.0075	0.0019±0.0087	-0.0002±0.0177
τ (fm/c)	27±49	100±491	∞±∞

Table 3.4. 1 Average velocity shift $<\Delta V>$ between the ^{4}He and the neutrons from the ^{6}He breakup, and the mean lifetime of the resonance determined from $<\Delta V>$.

resonance. So, the velocity shift appears to support a direct breakup mechanism. One can notice that it is a conservative estimation by setting the average impact parameter at the sum of the radii of the ^{6}He and U nuclei. With a higher b, the mean lifetime of the resonance τ is even smaller, therefore the corresponding Γ will be even further from the measured $\Gamma = 1.5MeV$. The mean lifetimes determined from the velocity shifts for the other targets are listed in Table 3.4.1. For Al and C, eq. (3.4.2) does not stand since E1 excitation is a very small part of the ^{6}He breakup, hence the calculated mean lifetimes have no physical meaning. The calculated mean lifetimes for the other targets are consistent within the statistical uncertainties.

3.5 Neutron Correlation

3.5.1 *Evidence From Neutron Relative Angle*

When the neutron halo was found in the nuclei near the neutron dripline, a simple model of core-plus-dineutron was suggested as the main structure [4]. If the ^{6}He nucleus does have a dineutron structure, coulomb excitation would cause a two-body breakup, in which the ^{4}He core is pushed away by the target nucleus, leaving the two neutrons with the same momentum. As a result, the two neutrons are going to be strongly correlated, i.e., the relative angle θ between the momenta of the two neutrons in the rest frame of the ^{6}He should be zero, or $\cos\theta$ should be 1. The measured $\cos\theta$ distributions are shown in Fig. 3.5.1 for the six targets. Two observations can be made from the figure. First, from the U target to the Al target, the distributions peak forward at $\cos\theta = 1.0$. Second, the forward peak, becoming weak from the heavy to the light targets, is hardly found in the distribution for the C target.

Again, the response of the detection system might distort the true $\cos\theta$ distribution. Since the solid-angle acceptance of the system favors the breakups with small n-n angles, the $\cos\theta$ distribution may be forced to be forward peaked. To take the response and other geometry effects into account, we calculated the $\cos\theta$ distribution for the U target in two extreme decay modes by Monte-Carlo simulations. In the first mode the two neutrons recoil against the ^{4}He core as a dineutron. The dashed histogram in Fig. 3.5.2, which shows the simulation result in the dineutron mode, is strongly forward peaked. The solid histogram in Fig. 3.5.2

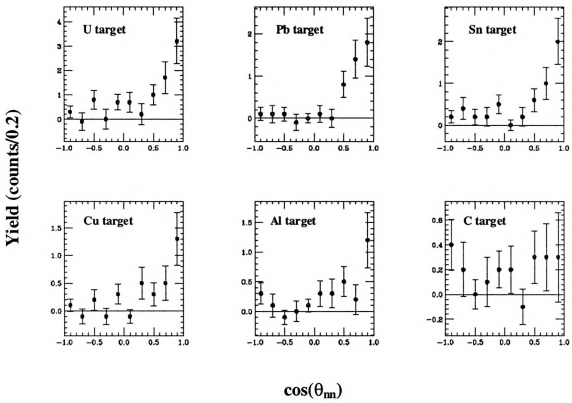

Figure 3.5.1 Angle distribution of the two neutrons from the ^{6}He breakup. These are 2n-^{4}He coincidence events for the six targets used in the experiment. The angle was calculated in the 2n+^{4}He center of mass frame.

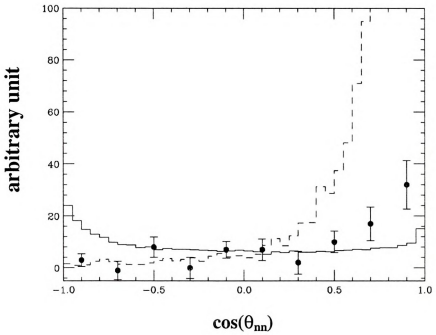

Figure 3.5.2 Angle distribution of the two neutrons from the ^{6}He breakup. The points are from the experiment for the U target. The solid histogram is a Monte-Carlo simulation with the 3-body phase space model. The dashed line is the same simulation with the dineutron model. The dashed line reaches above 10000 at $\cos\theta = 1$

is for the three-body phase space model. The two neutrons in the phase space decay mode are uncorrelated. As shown in Fig. 3.5.2, the angle distribution for the phase space model is only slightly peaked after being folded with the response function of our detection system. It also appears to be peaked at $\theta_{nn} = 180^0$. Figure 3.5.2 only plots the U data against the simulation results from the two models. We can further compare the two models with the angle distributions for the other targets shown in Fig. 3.5.1. One can see that the data suggest the correlation between the neutrons in ^{6}He is in between the two extreme models. This is consistent with the hybrid model [22] introduced in section 1.4. In this model, the two valence neutrons of ^{6}He stay in shell model orbits when they are close to the core, but form a cluster (dineutron) when they are far from the core. If the ^{6}He nucleus breaks up when the neutrons are far from the core, the neutrons tend to be strongly correlated. If the ^{6}He breaks up when the neutrons are close to the core, the neutrons tend to be uncorrelated. The tendency of the neutrons to be uncorrelated from the heavy to the light targets may be caused by the dominance of the sequential decay of the ^{6}He through the ^{5}He. In the sequential decay mode, the first neutron knocked out from the ^{6}He projectile has no correlation with the second neutron, which is later separated from the unstable ^{5}He. Only after all these decay modes are taken into account, can the cosθ distributions for the six targets be reproduced theoretically.

3.5.2 Evidence From Neutron Momentum

One indirect method to find the n-n correlation in ^{6}He is to compare the width of the ^{4}He parallel momentum distribution with that of the neutron parallel momentum

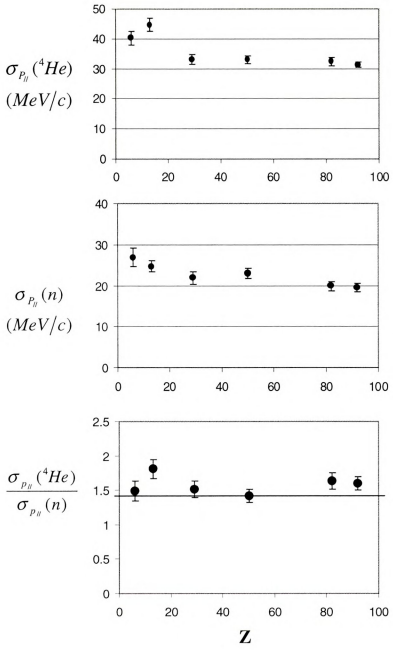

Figure 3.5.3 (a) The width of the ^{4}He parallel momentum distribution for the six targets. (b) The width of the neutron parallel momentum distribution for the six targets. (c) The ratio of the ^{4}He momentum width to the neutron momentum width. The data, the same as those in Fig. 3.2.8, are from n-^{4}He events. The dashed line indicates $\sqrt{2}$.

distribution. The theory is based on momentum conservation in a projectile as in the Goldhaber model [47]. The momentum correlation term between two neutrons in a projectile A can be written as

$$\langle \vec{p}(n_1) \bullet \vec{p}(n_2) \rangle = 1.5(\sigma_{A-2}^2 - 2\sigma_n^2), \qquad (3.5.1)$$

where σ_{A-2} and σ_n are the momentum widths of a fragment (A-2) and a neutron, respectively. It is easy to see that if the two neutrons are not correlated, then $\langle \vec{p}(n_1) \bullet \vec{p}(n_2) \rangle = 0$, and $\frac{\sigma_{A-2}}{\sigma_n} = \sqrt{2}$. In Fig. 3.5.3, the bottom graph plotted the ratio between $\sigma_{^4He}$ and σ_n for all the targets used in the experiment. The dashed line is $\sqrt{2}$. As shown in the figure, the data points are very much lying on the dashed line except the abnormal point for Al. This may indicate that the two neutrons in ^{6}He are uncorrelated.

4 Summary

The kinematically complete measurement of the ^{6}He dissociation made it possible for us to study the ^{6}He nucleus in a variety of perspectives. At first, the 2-n removal cross sections for the six targets were determined with the n-^{4}He coincidence data. The efficiency of the detection system was taken into consideration by scaling our data to a measured cross section on Si [17] at a similar energy. Our measured cross sections were consistent with the two theoretical calculations by Warner et al. [30] and Ferreira et al.[37]. For example, for U, σ_{2n} = (1.87 ± 0.24) b vs.1.68 b from ref. [30]; for C, σ_{2n} = (0.36 ± 0.05) b vs. 0.34 b from ref. [30] and 0.46 b from ref. [37]. The measured cross sections were also adjusted for the neutron multiplicity based on the theory by Barranco et al. [40,41]. The adjusted cross sections are somewhat smaller than the unadjusted ones except for C and Al.

The coulomb cross sections were separated from the nuclear cross sections by two methods, method 1 (extrapolation) and method 2 (fitting). The coulomb cross sections from method 1 are larger than those from method 2. Except for U and Pb, the results of method 2 are in better agreement with the calculation [37]. For U, Method 1 gives $\sigma_{coulomb}$ = (1.06±0.24) b; method 2 gives $\sigma_{coulomb}$ = (0.92±0.24) b . So on average, for U, the coulomb cross section contributes about 50% to the total cross section.

Neutron and ^{4}He momentum distributions were reported for the six targets. We chose the parallel momentum distributions over the transverse momentum distributions because the neutron and ^{4}He transverse momentum distributions were shown to be

significantly affected by the coulomb deflection and the solid-angle acceptance of the detection system. A Monte-Carlo simulation shows that the parallel momentum distribution is hardly altered by the acceptance of the system. The parallel momentum distributions were fitted with Gaussian functions. The width σ_n = (26.9±2.2) MeV/c for C is a little bit smaller than the result by Kobayashi et al. [9] who reported a width of 32 MeV/c for a transverse momentum distribution at a beam energy of 0.8 GeV/u. It was found that the widths of the neutron and ^{4}He parallel distributions increase as the size of the target decreases. This may indicate a shift of the reaction mechanism from dominating coulomb breakup to dominating nuclear breakup. The measured width of the ^{4}He parallel distribution, σ_n = (40.2±2.3) MeV/c, yields a rms radius of $\langle r^2 \rangle^{\frac{1}{2}} = 2.95 \pm 0.17\, fm$ for ^{6}He, which is consistent with the results determined by Tanihata et al. from the ^{6}He interaction cross sections [39,44].

The experiment was designed to measure 2-n coincidence events, in which all the three fragments from the ^{6}He breakup were detected. The kinematically complete measurement of the breakup made it possible for us to construct the decay energy distribution. By using the equivalent photon method, the decay energy spectrum for the U target was fitted with a Breit-Wigner function folded with the response function of the detection system. The fitting yields a Breit-Wigner shape dipole strength function $dB(E1)/dE_d$ with E_d = 1.9 MeV and Γ = 1.5 MeV. The location of the strength function agrees with the predictions of several three-body models [24,28,45]. However, the width of our dipole strength function appears to be narrower than those predicted in the models. This may be the result of our system's low sensitivity at high decay energies (> 3MeV).

Although our experimental result as well as the models [25,28,45] agree on the enhancement of the dipole excitation between E_x = 2.5 MeV and 3.0 MeV. Whether it is a soft dipole mode (SDM) is inconclusive based upon the shape of the strength function.

We looked for the post-breakup coulomb acceleration [10] in the ^{6}He breakup. First, from the 1n-^{4}He coincidence events, we found that the neutron average energy is significantly less than the ^{6}He per-nucleon beam energy for the high Z targets, which indicates that the breakups occur when the ^{6}He projectile is close to the target nucleus. The energy difference decreases with the decrease of the target charge, which is due to the weakening of the coulomb field of the target nucleus. Then, from the velocity difference spectra, the ^{4}He fragment on average was found to travel faster the neutrons. This finding supports the post-breakup coulomb acceleration. The average velocity shift for the U target, $\langle \Delta V \rangle = (0.0216 \pm 0.0045)\,c$, leads to a resonance with a much shorter mean lifetime than that inferred from the measured width of the dipole strength function. So the post-breakup acceleration suggests that ^{6}He does not break up through a resonance state. The concentration of the dipole strength function is just a resemblance of a resonance state.

To see if the two valence neutrons of ^{6}He are correlated, we plotted the distribution of the relative angle of the two neutrons in the rest frame of the ^{6}He projectile. Compared to the two extreme models—the dineutron model [4] and the direct breakup model [10]—the experimental data lean toward a structure without much correlation. We also found that the forward peaking of the relative angle distributions is

more prominent for heavy targets than for light targets, which may suggest the dominance of the sequential decay of the ^{6}He through the ^{5}He for light targets [16]. Besides the neutron relative angle distributions, we also looked for the neutron correlation in the ^{6}He nucleus from the widths of the neutron and ^{4}He momentum distributions. The fact that, on average, the ratio between the width of the ^{4}He momentum distribution and that of the neutron momentum distribution is close to $\sqrt{2}$, strongly supports that the valence neutrons are not strongly correlated in the ^{6}He nucleus.

PART II

Neutron Cross-talk in a Multiple-detector System

5.1 Introduction

A high-efficiency, position-sensitive, multi-detector system is the ideal apparatus for studying neutrons in the final states of nuclear reactions. Usually such detection systems are arrays of a number of neutron detectors [48-50]. In order to reduce dead space and to be able to measure small-angle coincidences, detectors are put as close to each other as possible. One major concern with these systems is cross-talk between the detectors. Cross-talk happens when a neutron which gives a signal in one detector is scattered into another detector where it again gives a signal. Thus one neutron appears to be two. Unfortunately, neutron cross-talk inevitably distorts the measurement. The ratio of cross-talk events to real two-neutron events varies with neutron energy and with detector configuration, and it could be very significant on some occasions [49-52]. So, it is very important to understand the effects cross-talk might have before such a detection system is used in experiments, and an effective method is needed to identify cross-talk events.

So far, only a few experiments have been reported on the study of cross-talk [49-52]. Cross-talk probabilities and effects in their specific detection systems were discussed. In this thesis, we present a method used to distinguish between cross-talk events and real two-neutron events in the energy region up to ~ 25 MeV.

A pair of "Neutron Walls", shown in Fig. 2.2.2, were built at the National Superconducting Cyclotron Laboratory (NSCL) for experiments in which two neutrons are produced in the final state. Most of the cross-talk events should be identified and rejected in order for a reliable experimental conclusion to be achieved.

5.2 Cross-talk in the neutron walls

5.2.1 Cross-talk types

In this paper, cross-talk events are classified into two categories as illustrated in Fig. 5.2.1.

(a) Cross-talk between the two walls, where a neutron makes one signal in the front wall and one signal in the back wall.

(b) Cross-talk within one wall, where a neutron makes two signals in different cells of the same wall. We anticipate that most of the cross-talk events within one wall happen in neighboring cells, because a neutron has to scatter at a large angle in order to reach distant cells, and the cross section for neutron scattering decreases significantly with increasing angle.

5.2.2 Cross-talk effects

Cross-talk affects a two-neutron experiment in two ways.

(a) It causes overestimation of neutron coincidences. Because cross-talk events

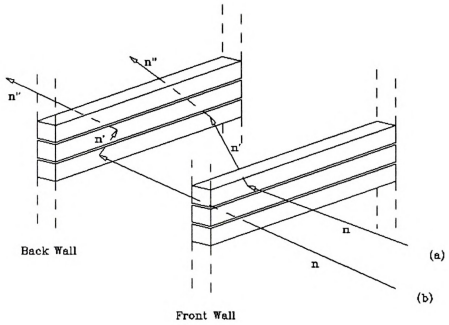

Figure 5.2. 1 The two types of cross-talk in the neutron walls. Type (a) cross-talk makes one signal in the front wall and another in the back wall. Type (b) cross-talk makes both signals in either one of the two walls.

are really one-neutron events, the number of neutron coincidences is enhanced by cross-talk events if these events are not identified as cross-talk events.

(b) The cross-talk within one wall distorts the small-angle correlation (Refer to the n-n relative momentum distribution in [10]). Since a neutron cross-talk event within one wall most probably happens in neighboring cells, the event looks like two neutrons emitted from the source with a small relative angle. If cross-talk events are not identified, the small-angle correlation is falsely enhanced.

Obviously, we have to reject as many cross-talk events as possible to avoid these negative effects.

5.3 Cross-talk identification

5.3.1 Neutron detection in liquid scintillator

It is useful to look at the main interactions between neutrons and scintillator materials before we introduce cross-talk identification.

Since the composition of the scintillator is hydrogen and carbon, neutrons usually interact with scintillator through the six processes listed in Table 5.3.1. Because #4 and #6 have no neutrons in the final states, they make no contribution to cross-talk.

Neutrons are detected with the scintillation light caused by energy loss of charged particles—protons, carbon nuclei and α particles — which are produced in #s 1, 2, 3 and In Fig. 5.3.1, the light response curves for these charged particles are plotted, based on

	Interactions	σ_R (24 MeV)
1	$n + p \rightarrow n + p$	0.406 b
2	$n + C \rightarrow n + C$	0.900 b
3	$n + C \rightarrow n' + C + \gamma$ (4.44 MeV)	0.104 b
4	$n + C \rightarrow He + Be$ - 5.71 MeV	0.048 b
5	$n + C \rightarrow n + 3\alpha$ - 7.26 MeV	0.210 b
6	$n + C \rightarrow p + B$ - 12.59 MeV	0.100 b

Table 5.3. 1 The interactions between neutrons and the nuclei in liquid scintillators — protons and carbon. σ_R is the reaction cross section. The data are from the code by Cecil *et al.*[9]

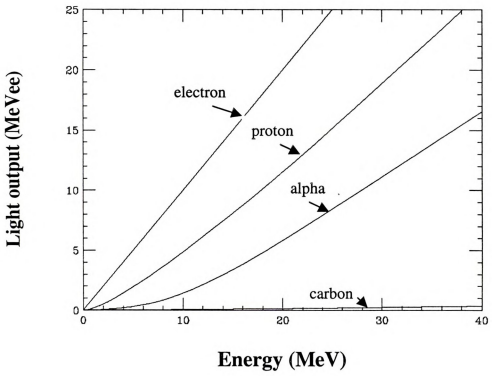

Figure 5.3. 1 The light response for electrons, protons, alphas and carbon nuclei in liquid scintillators. 1-MeVee is equal to the light produced by a 1-MeV electron. The data are from Verbinski et al. [8].

the data from Verbinski *et al.* [53]. Although #2, n-^{12}C elastic scattering, has the largest cross section, it hardly contributes to neutron detection because of the very low light response for carbon nuclei. Similarly, #3 gives little contribution to cross-talk effects when the γ-rays escape the scintillator undetected. Even if a γ-ray produced in #3 is detected, it can be ruled out by n-γ discrimination. Process #5, which has a reaction threshold of 7.86 MeV, produces low-energy α-particles. Because of the low light output of these particles, #5 does not play an important role in neutron detection below 25 MeV.

In conclusion, among those processes with neutrons in the final states, n-p scattering is dominant for neutron detection if $E_n \leq 25$ MeV. Therefore, n-p scattering is also the primary source of cross-talk.

*5.3.2 **2-body kinematics***

Since n-p elastic scattering is the major contributor to cross-talk, the well-known 2-body kinematics, illustrated in Fig. 5.3.2, becomes our basis for neutron cross-talk identification. In this figure, n is the incident neutron, n′ is the scattered neutron, p is the recoil proton, and θ represents the neutron's scattering angle. If we assume $m_n = m_p$, energy and momentum conservation result in the following equations:

$$E_n' = E_n - E_p \qquad (5.1)$$

$$E_n' = E_n \times \cos^2\theta \qquad (5.2)$$

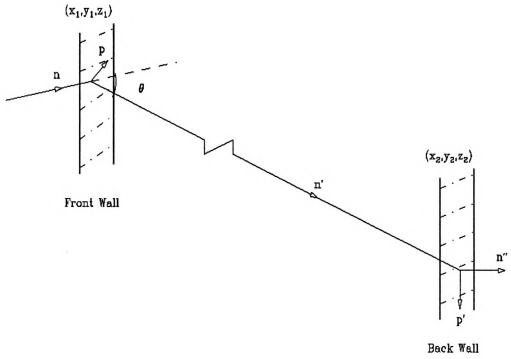

Figure 5.3. 2 An example of cross-talk between the front wall and the back wall. The neutron makes one signal in a cell of the front wall and another one in a cell of the back wall. The position of each scattering is expressed by (x,y,z). The scattering in the front wall follows the 2-body kinematics given by eqs. 1 and 2 in the text.

The above equations exhibit the correlation between neutron energy, proton energy and the scattering angle. If E_n and E_p are known, E_n' and $\cos\theta$ can be determined.

In the next three sections, we show how the 2-body kinematics engenders three signatures of cross-talk.

5.3.3 $(COS\theta)_c$-$(COS\theta)_m$ = 0 (signature #1 of cross-talk)

Figure 5.3.2 shows a typical cross-talk event between the front wall and the back wall. There are two scatterings detected in this case. For the first scattering, we measure by TOF the incoming neutron's energy — E_n, the light output of the recoil proton — L_p, and the position of the scattering — (x_1,y_1,z_1). These coordinates are defined in such a way that the x and y axes, vertical and horizontal, respectively, to the cells, are in the plane of a wall, and the z axis points from the neutron source to the walls. The neutron source also serves as the origin of the coordinates. If a neutron is detected in a certain cell, y_1 is given by the position of the cell's center, x_1 is given by the time difference of the signals at the ends of the cell, and z_1 is the distance between the source and the front wall. The recoil proton's energy E_p can be extracted from the light output in the NE-213 scintillator by using its light response function. The response function for charged particles was determined by fitting the light yield data of Verbinski *et al.* [53] with an empirical expression of the form:

$$L = a\cdot(1 - \exp(-b\cdot E^c)) + d\cdot E + f \qquad (5.3)$$

The light output L is in the unit MeVee (the light produced by an electron of 1 MeV), and E is in MeV. E denotes the energy of charged particles. The parameters — a, b, c, d, f — which give the best fit for protons, alpha particles and carbon nuclei, are listed in Table 5.3.2. After E_n and E_p are determined, we can calculate the scattered neutron's energy by energy conservation, $E_n' = E_n - E_p$. Then eq. (5.2) is used to obtain the value of COSθ. We call it the "calculated" COSθ, $(COS\theta)_c$.

$$(COS\theta)_c = (E_n' / E_n)^{1/2} \qquad (5.4)$$

For the second scattering, we determine its position — (x_2,y_2,z_2). From the position in the front wall, $\mathbf{u_1} = (x_1,y_1,z_1)$ and the position in the back wall, $\mathbf{u_2} = (x_2,y_2,z_2)$, we can obtain the "real" value of COSθ. We call it the "measured" COSθ, $(COS\theta)_m$.

$$\mathbf{u_{21}} = \mathbf{u_2} - \mathbf{u_1} \;\rightarrow\; (COS\theta)_m = \mathbf{u_1}\cdot\mathbf{u_{21}} / |\mathbf{u_1}|\,|\mathbf{u_{21}}| \qquad (5.5)$$

If the event is a cross-talk event, $(COS\theta)_c$ should equal $(COS\theta)_m$, i.e., $(COS\theta)_c$-$(COS\theta)_m$ should be zero. Due to the uncertainty in measuring all the quantities, e.g., energies and positions, the $(COS\theta)_c$-$(COS\theta)_m$ distribution function is not a δ-function at $(COS\theta)_c$-$(COS\theta)_m = 0$, but a peak with a width. The spread of the peak is related to the energy resolution and the position resolution of the detection system.

Unless cross-talk events are identified, we cannot tell cross-talk events from real 2-n events in which two neutrons from the source are detected. Shown in Fig. 5.3.3 is a real 2-n event between the front wall and the back wall. If we assume that this is a cross

Particles	a	b	c	d	f
p	-5.6375	0.115	0.838	0.7875	0.015
α(<5 MeV)	-6.1643	-0.001	2.2	0.01585	0.0
α(>5 MeV)	-5.2688	0.0872	1.22	0.543	0.0
C	0.0	0.0	0.0	0.017	0.0

Table 5.3. 2 The best parameters of the light response function $L=a\times(1-\exp(-b\times E^c)) + d\times E + f$ for protons, alpha particles and carbon nuclei.

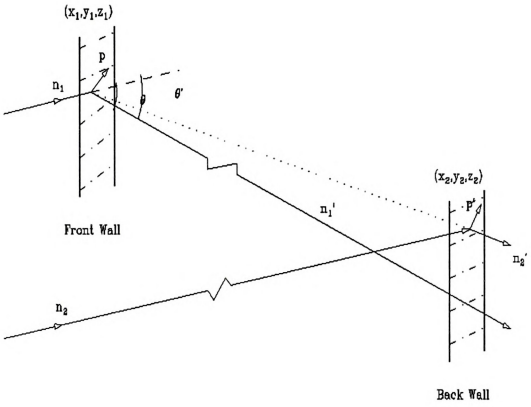

Figure 5.3. 3 An example of a real 2-n event between the front wall and the back wall. If we assume this is a cross-talk event, θ should be the neutron's scattering angle according to 2-body kinematics. However, the positions of the two scatterings give θ′. Unlike cross-talk events, the two angles are not correlated for real 2-n events.

talk event, we expect θ, which is calculated on the basis of 2-body kinematics, to be the neutron's scattering angle. However, the positions of the two interactions give θ′. The two angles are different because they are not correlated by 2-body kinematics. Since the cosine of θ gives $(COS\theta)_c$ and the cosine of θ′ gives $(COS\theta)_m$, $(COS\theta)_c$-$(COS\theta)_m$ is not equal to 0. So, for real 2-n events, $(COS\theta)_c$-$(COS\theta)_m$ won't form a peak at zero. Instead, $(COS\theta)_c$-$(COS\theta)_m$ should be distributed over the range allowed by the geometry of the neutron walls.

5.3.4 ΔT_c-ΔT_m = 0 (signature #2 of cross-talk)

In part (3), we established the first signature of cross-talk in terms of $(COS\theta)_c$-$(COS\theta)_m$. Similarly, in this part, we will establish the second signature of cross-talk from another aspect of the 2-body kinematics of n-p scattering. Referring to the example of cross-talk in Fig. 5.3.2, we calculate the scattered neutron's energy E_n' from the incident neutron energy E_n and the recoil proton energy E_p with eq. 5.1. From E_n', we calculate the velocity of the scattered neutron v_n'. L_{12} is the flight path of the scattered neutron between $\mathbf{u_1} = (x_1,y_1,z_1)$ in the front wall and $\mathbf{u_2} = (x_2,y_2,z_2)$ in the back wall. If it is a cross-talk event, determination of v_n' and L_{12} gives the flight time of the scattered neutron. We call it the "calculated" ΔT, ΔT_c. The following is the logic flow leading to ΔT_c:

$$\left.\begin{array}{l} E_n\,,\,E_p \rightarrow\ E_n' \rightarrow v_n' \\ \mathbf{u_1}\,,\,\mathbf{u_2} \rightarrow L_{12} = |\mathbf{u_1} - \mathbf{u_2}| \end{array}\right\} \Rightarrow \quad \Delta T_c = L_{12} / v_n' \qquad (5.6)$$

On the other hand, the actual time difference can be measured by taking the difference between the TOF of the first scattering, $(TOF)_1$, and that of the second scattering, $(TOF)_2$. We call it the "measured" ΔT, ΔT_m.

$$\Delta T_m = (TOF)_2 - (TOF)_1 \qquad (5.7)$$

For neutron cross-talk events, ΔT_c should be equal to ΔT_m. The ΔT_c-ΔT_m distribution function peaks at zero, but again, due to uncertainties of measurements, the peak has a finite width. Since the two scatterings in a real 2-n event are not correlated by 2-body kinematics, ΔT_c does not represent the time difference between them. Hence ΔT_c-ΔT_m tends to be random for real 2-n coincidences.

5.3.5 $E_p' \leq E_n'$ (signature #3 of cross-talk)

In a cross-talk event, the energy E_p' of the recoil proton in the back wall should be less than or equal to the energy E_n' of the neutron coming from the first scattering in the front wall. In a real 2-n event, that is not necessarily true because the two scatterings involve two different neutrons from the source. E_p' could be larger than E_n'. So, $E_p' \leq E_n'$ becomes the third signature of cross-talk.

We have introduced the three signatures of cross-talk between the front wall and the back wall. Cross-talk within one wall has all three signatures, too. But the first signature, $(COS\theta)_c$-$(COS\theta)_m$=0, is not used because the geometric configuration of the cells in one wall destroys our ability to determine $(COS\theta)_m$, as illustrated in Fig. 5.3.4.

5.3.6 Monte-Carlo Simulation

In order to check the signatures of cross-talk, a Monte-Carlo code has been written based on the code developed by R. A. Cecil *et al.* [54]. Our modifications of the code are listed below:

a. Implementation of measured neutron differential cross sections for n-p and n-C elastic scattering. The data were retrieved from the National Nuclear Data Center (NNDC). The energy dependence of the angular distributions was parameterized. Parameter interpolation is used in the code to get the differential cross section for continuous energy values.

b. Consideration of a neutron's reaction in the Pyrex glass cell. The Pyrex is composed of oxygen, silicon, boron, sodium and aluminum, and more than 80% of the material is oxygen and silicon. In order to simplify the simulation, B and Al are treated as O and Si respectively. Since the atomic mass number of Na is between those of O and Si, half Na is treated as O and half is treated as Si. All data, including total cross sections with O and Si and differential cross sections for elastic scattering with O and Si, are obtained from the NNDC.

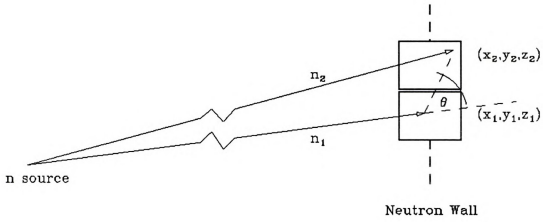

Figure 5.3. 4 Side view of two neutrons detected in neighboring cells. Because it is impossible to determine the exact positions where the neutrons scattered, θ can vary from almost 0° to 180°.

c. Input of the geometric configuration of the detection system. In the original code only one detector was treated. The modified code deals with 50 detectors.

d. Fitting of light response function. Parameters for different charged particles are in Table 5.3.2.

A study of neutron cross-talk was conducted with the code to simulate its effect on a measurement of the two neutrons from ^{11}Li breakup. ^{11}Li has two loosely bound halo neutrons. When ^{11}Li goes through a strong Coulomb field [10], it may absorb a virtual photon with an energy greater than the two-neutron separation energy of ^{11}Li, and hence break up into two neutrons and a ^{9}Li. The difference between the energy of the photon and the two-neutron separation energy is referred to as the decay energy. The two neutrons and ^{9}Li are assumed to share the decay energy according to the momentum distribution in 3-body phase space.

In the code, the two neutrons are traced as they go through the neutron walls. If both neutrons are detected, we have a real 2-neutron event. If only one of the neutrons is detected, but in two different cells, we have a cross-talk event. This simulation makes it possible for us to make a direct comparison between real coincidence events and cross-talk events. Furthermore, it can show the reliability of our method to identify cross-talk events from real 2-n events. The ^{11}Li beam energy we used in the code is 25 MeV/u. We chose 1.0 MeV as the ^{11}Li decay energy. The neutron walls are set at zero degrees relative to the beamline and perpendicular to it. The first wall is 5 meters from the source. The second wall is 1 meter behind the first one. The results of the simulation are

shown in Table 5.3.3 and Fig. 5.3.5. Table 5.3.3 gives the number of real 2-n events and cross-talk events detected by the neutron walls when one million ^{11}Li breakups occur. The events are categorized into the events between the two walls, the events within the front wall and the events within the back wall. In Fig. 5.3.5, Plot (a) gives $(COS\theta)_c$-$(COS\theta)_m$ distributions for the 2-neutron coincidence events between the two walls. The solid histogram is for all the 2-n events, both real and apparent, whereas the dashed histogram is for the real 2-n coincidences only. Their difference is the distribution for cross-talk events. The cross-talk events form a peak at zero, as we expected. Plot (b) gives ΔT_c-ΔT_m distributions for the 2-n events between the two walls and plot (c) gives ΔT_c-ΔT_m distributions for the 2-n events within one wall. As in plot (a), distributions for all the 2-n coincidence events and for the real 2-n coincidence events are plotted. Again, the peaks around zero are the result of cross-talk.

The spread of the peaks for the cross-talk events is due to the uncertainty of the measurements. The uncertainty parameters used in the code are: time resolution(σ_t) = 0.4 ns, position resolution(σ_p) = 5 cm, light collection uncertainty(σ_l) = 10% for a light output of 1.0 MeVee and the attenuation length in the NE-213 = 160 cm. Among the parameters, light collection uncertainty is due to the statistical fluctuation in the amount of light collected by the phototubes. It is proportional to $1/L^{1/2}$, where L, the light produced by charged particles, such as protons, alpha particles and carbon nuclei, is in units of MeVee. The asymmetry of the peaks in the ΔT_c-ΔT_m distributions for cross-talk events is due to neutron multiple scattering. Sometimes neutron scattering with C or H,

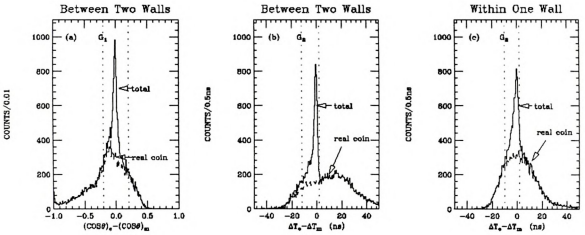

Figure 5.3. 5 The results of a Monte-Carlo simulation in which two neutrons from ^{11}Li breakup are detected by the neutron walls. Given by the solid histograms, "total" represents all the two-neutron events detected by the walls. Given by the dashed histograms, "real coin" represents the real two-neutron coincidences. G_1, G_2 are the gates used to reject the cross-talk events. (a) $(COS\theta)_c$-$(COS\theta)_m$ distribution for the events between the two walls. (b) ΔT_c-ΔT_m distribution for the events between the two walls. (c) ΔT_c-ΔT_m distribution for the events within either the front wall or the back wall.

Between the two walls	
Total 2-n events	27,390
Real events	20,985
Cross-talk events	6,405
Within the front wall	
Total 2-n events	16,194
Real events	13,132
Cross-talk events	3,062
Within the back wall	
Total 2-n events	10,865
Real events	8,335
Cross-talk events	2,530

Table 5.3. 3 Number of 2-n events detected by the neutron walls when one million ^{11}Li breakups were simulated.

especially with C, generates too little light to be detected. However the deflected neutron may generate enough light to be detected in the next scattering in the scintillator. Although multiple scattering can make $(COS\theta)_m$ either larger or smaller, multiple scattering always increases the neutron flight path, and hence can only increase ΔT_m. That is why the $(COS\theta)_c$-$(COS\theta)_m$ peak is symmetrical while the ΔT_c-ΔT_m is asymmetric, with a tail on the negative side.

The results of the simulation clearly show us the differences between cross-talk events and real 2-n events. Based on these differences, as well as $E_p' \leq E_n'$, cross-talk identification can be achieved.

5.3.7 Steps for neutron cross-talk identification

From the signatures described in sections *5.3-5.5*, we found that cross-talk events form a peak at zero in both the $(COS\theta)_c$-$(COS\theta)_m$ distribution and the ΔT_c-ΔT_m distribution, and they have the property that $E_p' \leq E_n'$. Therefore, we can reject cross-talk events by setting gates around zero on the two distributions and by requiring $E_p' \leq E_n'$. The setting of the gate should be determined by the spread of the distribution of the cross-talk events. For convenience of explanation, we denote G_1 as the gate on $(COS\theta)_c$-$(COS\theta)_m$ and G_2 as that on ΔT_c-ΔT_m, as indicated in Fig. 5.3.5. C_3 is the third condition that $E_p' \leq E_n'$. From the result of the ^{11}Li breakup simulation, we can see that there are some real 2-n events mixed with cross-talk events in the cross-talk region. When we reject cross-talk events, we cannot avoid losing some real 2-n coincidence events. In choosing

choosing gates, the goal, of course, is to reject most of the cross-talk events and keep most of the real 2-n events. It is important to realize that a 2-n event is considered a cross-talk event only if it is found in both of the gates G_1, G_2 and it satisfies C_3. For real 2-n events the three conditions are not correlated. Even so, some real 2-n events may satisfy all three conditions. For events within the front wall or within the back wall, only G_2 and C_3 are used (refer to section *5.5*).

Here are the three steps to tell if an event between the walls is a cross-talk event after G_1, G_2 are chosen and C_3 is considered.

(a) Calculate $(COS\theta)_c$-$(COS\theta)_m$. Is it within G_1?

(b) Calculate ΔT_c-ΔT_m. Is it within G_2?

(c) Calculate En′ and Ep′. Does it satisfy C_3?

Only if the answer is "yes" for all the three steps, is the event identified as a cross-talk event. For 2-n events within one wall, only the last two steps are used.

In the simulation for ^{11}Li breakup, the method was used to identify the cross-talk events. G_1 was set from -0.2 to 0.2 (Fig. 5.3.5). G_2 was set from -12 ns to 2 ns. The results of the simulation for 2-n events between the two walls are listed in table 5.3.4. In this particular simulation, we had 27,390 2-n events, of which 20,985 were real 2-n events and 6,405 were cross-talk events. There were 7,340 events satisfying G_1, G_2 and C_3, of which 5,013 were cross-talk events and 2,327 real events. By taking the 7,340 events out as cross-talk events, we rejected 78.3% of the cross-talk events and at the same

Real events	20,985
Cross-talk events	6,405
Total no. of events	27,390
Real events	
in G1	10,995
in G2	3,981
satisfy C3	10,931
in G1 and in G2	2,746
in G1 and in G2 and satisfy C3	2,327
retained real events	18,658
Cross-talk events	
in G1	5,904
in G2	5,474
satisfy C3	6,251
in G1 and in G2	5,118
in G1 and in G2 and satisfy C3	5,013
retained cross-talk events	1,392
% of identified cross-talk	**78.3%**
Loss of real events	**11.1%**
Cross-talk percentage of total 2-n events (before)	**23.4%**
Cross-talk percentage of total 2-n events (after)	**6.9%**

Table 5.3. 4 Results of the simulation of ^{11}Li breakup for 2-n events between the two walls. G1 and G2 are the gates set on $(COS\theta)_c$-$(COS\theta)_m$ and ΔT_c-ΔT_m distributions, respectively, shown in Fig. 5.3.5. C3 is the condition that $E_p' \leq E_n'$, explained in section 5.5. In experiments, all the 2-n events which fall in G1, G2 and satisfy C3 are rejected as cross-talk events.

time lost only 11.1% of the real 2-n events. This reduced the cross-talk impurity from 23.4% to 6.9%. Using G_2 and C_3, we also identified the cross-talk events within one wall. G_2 was set from -10 ns to 2 ns. Following the same procedure used for 2-n events between the two walls, we rejected 79.6% of the cross-talk events and lost 26.8% of the real 2-n events. The cross-talk impurity was reduced from 22.9% to 7.7%. Because only two conditions can be used for 2-n events within one wall, we lose more real events in this case than we do in the case for 2-n events between the two walls.

Since cross-talk identification depends on the three gates, the success of the method depends on how the gates are set. The gates depend on the spread of the $(COS\theta)_c$-$(COS\theta)_m$ and ΔT_c-ΔT_m distributions for cross-talk events. The spread is going to be different for different detection systems. For any system, there will always be the need for a software trade-off between size and purity of the event set. The higher the purity demanded, the greater the number of good events sacrificed. The choice is made by the experimenter.

5.4 Experiment

5.4.1 Setup

A test experiment was performed at the NSCL using the reaction:

$$^7Li + p \rightarrow n + {}^7Be - 1.64\ MeV \qquad (5.8)$$

In this reaction, only one high-energy neutron is produced. Therefore, all the 2-n events detected by the neutron walls were cross-talk events. The purpose of the experiment was

to check if our simulation code gives the right prediction, i.e. to see if the $(COS\theta)_c$-$(COS\theta)_m$ and ΔT_c-ΔT_m distributions for cross-talk events obtained from the experiment agree with those simulated by our computer codes. The experimental setup is shown in Fig. 5.4.1. The neutron walls were set at 35° relative to the beamline. Concrete blocks were placed between the downstream beam pipes and the neutron walls to shield the walls from neutrons produced by target-scattered protons striking the pipes. Neutrons were produced by bombarding a 0.5-mm ^{7}Li target with 29.8-MeV protons extracted from the K1200 cyclotron. Forty of the 50 glass cells were used in the experiment, but only 20 cells were analyzed due to problems with the pulse-shape-discrimination circuitry for the other 20 cells. Of the 20 working cells, there were 8 cells in the front wall, from no. 5 to no. 12, counting from the bottom. The other 12 cells were in the back wall from no. 9 to no. 20.

5.4.2 Data Analysis

Fig. 5.4.2 shows the neutron TOF spectrum for cell no. 7 in the front wall. The mean time of the two signals at the ends of the cell gives the start. The downscaled cyclotron radio frequency time gives the stop. Neutrons under the sharp peaks are from the ^{7}Li(p,n) reaction which goes to either the ground state or the first excited state of ^{7}Be. The two states have an energy difference of only 0.43 MeV. The resolution of the system is not able to distinguish between the two states. The energy of the neutrons under the

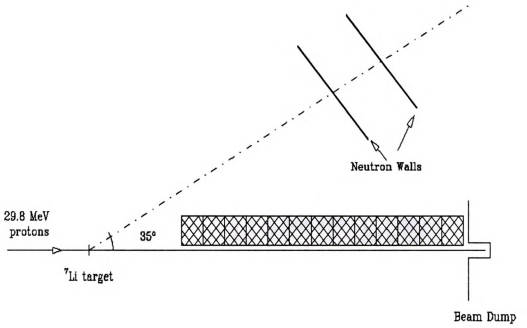

Figure 5.4. 1 Layout of the ^{7}Li(p,n) experiment. The front wall was placed 5 meters from the target, 35° relative to the beamline. The second wall was 1 meter behind the first one. The shaded area was a stock of concrete blocks

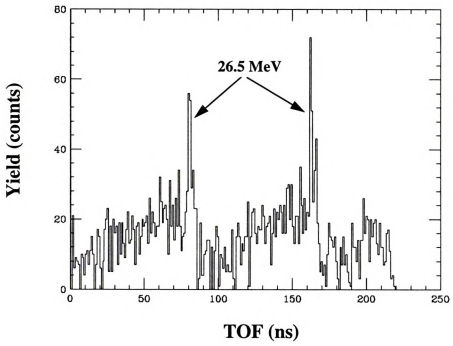

Figure 5.4. 2 Time-of-flight spectrum for neutrons detected in cell #7 in the ^{7}Li(p,n) experiment. The signal of cell #7 gave the start and the downscaled cyclotron radio frequency signal gave the stop. The sharp peaks are from neutrons produced in the reactions leading to either the ground state or the first excited state of ^{7}Be.

peaks can be determined from their reaction angles by 2-body kinematics. The energy loss of the protons in the target was 0.4 MeV. Using an average of 0.2 MeV, the energy of the neutrons under the sharp peaks detected in the front neutron wall ranges from 25.4 MeV to 27.3 MeV, depending on where the neutrons strike the wall, i.e., on the reaction angle. The neutrons outside the sharp peaks in Fig. 5.4.2 are predominantly from the reaction

$$^{7}Li + p \rightarrow n + {}^{3}He + {}^{4}He - 3.23\ MeV \qquad (5.9)$$

The 3-body final state makes the E_n spectrum a continuum. The energies of these neutrons were measured by TOF. Simulations were carried out only for the neutrons under the sharp peaks because their differential cross-sections were well measured and those neutrons follow simple 2-body kinematics.

Here is how we treat each cross-talk event.

(a) Check for neutron pulses by n-γ discrimination [32]. Reject any γ-ray or cosmic ray events.

(b) Determine the neutron scattering angle θ by the positions of the two scatterings. From the two positions, $(COS\theta)_m$ is determined.

(c) Determine the $^{7}Li(p,n)$ reaction angle by the position of the first scattering. From the reaction angle, the incident neutron energy E_n is calculated.

(d) Determine E_p, the energy of the recoil proton in the first scattering, using the geometric mean of the pulse heights from the phototubes at the ends of the cell. PH_l and

PH_r denote the pulse heights read out at the left and right ends of the cell, and PH_g denotes the geometric mean. Due to the light attenuation in the NE-213 scintillator, PH_l and PH_r are dependent upon the location of the interaction in the cell: $PH_l \propto I_o\exp(-x/\lambda)$ and $PH_r \propto I_o\exp(-(L-x)/\lambda)$, where I_o is the light intensity, x is the distance light travels from where it is produced to the left end of the cell, L is the length of the cell, λ is the light attenuation length in such the scintillator. PH_g is given by

$$PH_g = (PH_l \times PH_r)^{1/2} \propto I_o\exp(-L/2\lambda) \qquad (5.10)$$

Since L and λ are constants, PH_g is proportional to the light produced in the scintillator, and is independent of the location of the interaction in the cell. In order to determine the light production of protons in terms of MeVee, each cell was calibrated with the 2.38-MeV Compton edge of a ^{228}Th source and the 4.2-MeV Compton edge of a Pu-Be source. After the light output of each proton is determined, we use eq. 5.3 to extract the proton energy E_p.

(e) Calculate $(COS\theta)_c$ from eq. 5.4 with E_n and E_p obtained from (c) and (d).

(f) Determine ΔT_c from eq. 5.6 with E_n, E_p and the positions of the two scatterings.

(g) ΔT_m, the time difference between the scatterings, was measured in our experiment. In some experiments, $(TOF)_1$ and $(TOF)_2$, the TOFs of the first scattering and the second scattering, respectively, are measured. Then ΔT_m is obtained by subtracting $(TOF)_2$ from $(TOF)_1$ (eq. 5.7).

Following the procedure from (a) to (g), we get $(COS\theta)_c$-$(COS\theta)_m$ and ΔT_c-ΔT_m for each 2-n event.

5.4.3 Results

In Fig. 5.4.3, the $(COS\theta)_c$-$(COS\theta)_m$ and ΔT_c-ΔT_m distributions for those neutrons under the sharp peaks in Fig. 5.4.2 are plotted with the open symbols. The histograms are the results of our simulation. All the histograms are normalized according to the areas covered by the data points. Our simulation results are in good agreement with the experimental data. The data points in plot (a) are not exactly centered at zero, as the histogram is. The shift of 0.025 may be due to some error in the measurement of the proton energy. Using eqs. 1 and 2, we found that a systematic overestimation of 0.65 MeV in E_p could cause the 0.025 shift in the $(COS\theta)_c$-$(COS\theta)_m$ distribution. Two possible sources of this overestimate are an error of a few percent in the light response function [53] or in the proton beam energy. Otherwise, all the measured features of the cross-talk agree with the features in the simulation.

Fig. 5.4.4 shows that the distributions for all the neutron cross-talk events, those initiated by the 2-body reaction (eq. 5.8 and the sharp peaks in Fig. 5.4.2) and those initiated by 3-body reaction (eq. 5.9 and the continuum neutrons in Fig. 5.4.2), are similar but somewhat broader than those for the 2-body reaction alone.

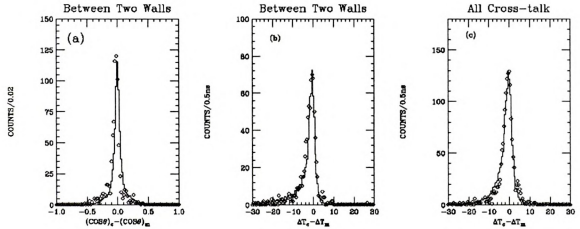

Figure 5.4. 3 Cross-talk distributions for the neutrons under the sharp peaks in Fig. 5.4.3 from the ^{7}Li(p,n) experiment. The experimental data are given by open symbols. The histograms are the results of our simulation. (a) $(COS\theta)_c$-$(COS\theta)_m$ distribution for the cross-talk events between the two walls. (b) ΔT_c-ΔT_m distribution for the same events in (a). (c) ΔT_c-ΔT_m distribution for all the cross-talk events.

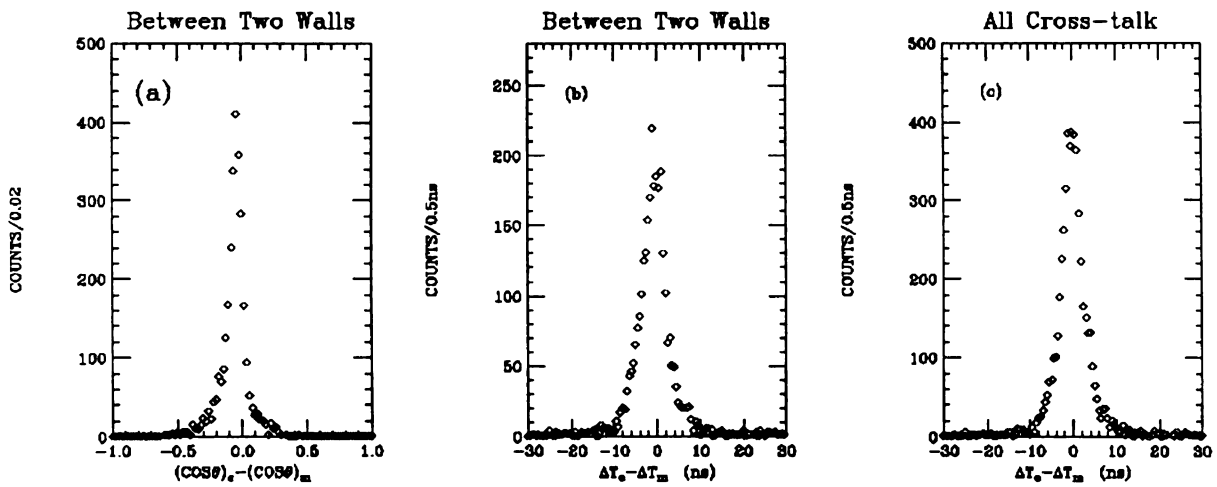

Figure 5.4. 4 Cross-talk distributions for all the neutrons from the ^{7}Li(p,n) experiment—those from the 2-body reaction (eq. 5.8) and those from the 3-body reaction (eq. 5.9). (a) $(COS\theta)_c$-$(COS\theta)_m$ distribution for the cross-talk events between the two walls. (b) ΔT_c-ΔT_m distribution for the same events in (a). (c) ΔT_c-ΔT_m distribution for all the cross-talk events.

5.5 Summary

A method has been introduced to identify the cross-talk events in multi-detector systems in the energy region up to 25 MeV. In this method, three signatures of cross-talk, $(COS\theta)_c$-$(COS\theta)_m$=0, ΔT_c-ΔT_m=0 and $E_p' \leq E_n'$, were established using the n-p elastic scattering kinematics. The three signatures were then studied by a Monte-Carlo simulation. Following the identification procedure presented in the paper, we rejected 79% of the neutron cross-talk events in a simulated ^{11}Li breakup experiment. The cross-talk effect was significantly reduced.

A ^{7}Li(p,n) experiment was performed to check our simulation code. The $(COS\theta)_c$-$(COS\theta)_m$ and ΔT_c-ΔT_m distributions from Monte-Carlo simulation were compared with experimental data. The consistency between the experimental data and the simulation results proves that neutron cross-talk identification can be achieved in 2-n coincidence experiments.

Our method is based on the 2-body kinematics. In principle, it can be applied to identify neutron cross-talk in any organic multi-detector system. How well it works depends on the specific configuration and the neutron energy.

APPENDICES

Appendix A: Calibration of Fragment Detectors

A.1. Neutron Walls

For a ^{6}He dissociation event detected in the experiment, the momenta of the neutrons and the ^{4}He had to be accurately measured. To determine a neutron's momentum, we have to know the velocity and the direction of the neutron. The velocity of a neutron was determined by dividing the travel distance, which is from the target to where it was detected in a cell of a neutron wall, by the time of flight (TOF) of the neutron. The direction of the neutron was determined from the position of the neutron on the wall and the position of the target. The latter was fixed and easily measured before the experiment.

A.1.1. Neutron TOF

A neutron is detected through the light generated in the interaction between the neutron and the scintillator material—Carbon and Hydrogen. The light is collected by both PMTs at the ends of one cell. The time signal is picked up from the anode of a PMT. In the experiment, the time difference between each PMT triggered by a neutron, and the scintillator bar triggered by a ^{4}He fragment was measured. Let T_L be the time difference between the left PMT (viewing from the target) and the scintillator bar, T_R be the time difference between the right PMT and the Scintillator bar. x is the distance from the detection spot to the left PMT. Then

$$T_L = \frac{x}{v} + \Delta TOF + c_1, \qquad \text{(A.1)}$$

where v is the velocity of light in the scintillator, ΔTOF is the time difference between the cell and the scintillator bar, c_1 is the constant of the electronic devices. Likewise,

$$T_R = \frac{l - x}{v} + \Delta TOF + c_2, \qquad \text{(A.2)}$$

where l is the length of the cell. As shown in eqs. A.1 and A.2, T_L and T_R are position dependent. On the other hand, if eq. A.2 is added to eq. A.1, the equation becomes

$$\frac{(T_L + T_R)}{2} = \frac{l}{2v} + \Delta TOF + \frac{c_1 + c_2}{2} = \Delta TOF + c, \qquad \text{(A.3)}$$

which is position independent because x is eliminated from the equation. In the experiment, time calibration was conducted with the γ rays which were produced when the primary beam ^{18}O stopped in the scintillator bars. The ^{18}O beam was used because it was the most intense beam in the experiment. Almost all the ^{18}O particles stopped in bar #9. What we are interested in are those γ rays which, produced in bar #9, were detected in the neutron walls later. When the $\frac{T_L + T_R}{2}$ spectrum is plotted for the coincidence events, a γ peak can be observed as shown in Fig. A.1. The γ peak corresponds the time for a γ ray to travel from bar #9 to the front neutron wall. The distance between the bar and the center of the front wall is 332 cm, which gives ΔTOF =11.1ns. Therefore, the γ peak becomes the reference time. The ΔTOF of any event was determined relative to the peak.

For a neutron coincidence event, ΔTOF is not the final TOF we are interested in because it only measures the difference between the time for the neutron to reach the neutron walls and the time for the fragment to reach the scintillator array. We are only

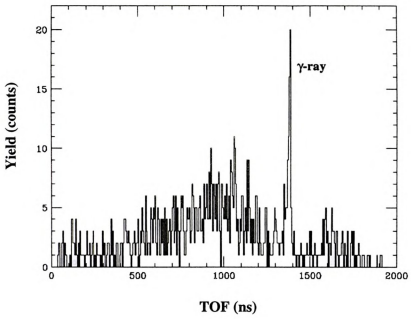

Figure A. 1 The time of flight (TOF) calibration. The γ rays, produced in scintillator bar #9 by a ^{18}O beam, were detected in the front neutron wall. The flight time for a γ ray between the bar and the front neutron wall is 11.1 ns.

interested in the absolute time of flight for the neutron, i.e. the neutron TOF from the target to the detection spot in the neuron walls—TOF_n from which neutron energy can be determined. The relation between TOF_n and ΔTOF is $\Delta TOF = TOF_n - TOF_f$, where TOF_f is the fragment TOF from the target to the scintillator array. The neutron TOF can be calculated with

$$TOF_n = \Delta TOF + TOF_f . \qquad \text{(A.4)}$$

In order to find TOF_f, we have to know the velocity of the ^{4}He fragment and its flight distance. The velocity of the ^{4}He was determined from the energy measured by the scintillator array in an event-by-event base. Because the ^{4}He fragment was deflected by the magnet used in the experiment, it seems that the flight distance depends on the trajectory of the fragment. It is possible to use the mapping result to find the trajectory of each ^{4}He, then the flight distance. However, the flight distance from the target to the scintillator array for the ^{4}He fragment in the experiment was found to be pretty much independent of the trajectory. The ^{4}He particles, with energies from 15 MeV/u to 30 MeV/u and entering the magnet at different positions, were sent through the magnet in a program written to track the trajectories of the charged particles. The flight paths, averaging 180.38 cm, range from 176 cm to 185 cm. If we use the average flight path for all the ^{4}He in the experiments, its contribution to the error of the neutron TOF is expected to be less than 1 ns.

A1.2 Neutron Position

When a neutron wall was placed in the N4 vault, every cell's position in the wall was fixed. The position of a cell was represented by the center of the cell. The position of a neutron in a cell is measured by taking the difference between T_L and T_R (referring to eqs. A.1 and A.2):

$$T_L - T_R = \frac{2x}{v} + \frac{l}{v} + c_1 - c_2 = \frac{2x}{v} + c \qquad \text{(A.5)}$$

So, $T_L - T_R$ is proportional to x. Shown in Fig. A.2 is a $T_L - T_R$ spectrum for a cell of the neutron walls. The data were collected with cosmic rays showering every cell evenly. The middle point of the spectrum corresponds to the physical center of the cell. The two shoulders correspond to the two ends of the cell. The length of the cell is divided by the channel number between the half height of the shoulders to obtain the conversion factor—from channel number to length.

A.2. Scintillator Bar Detectors

A.2.1. Energy calibration

Both ^{6}He beam and ^{4}He fragment stopped in the scintillator bars. For each charged particle detected, light was collected by the two PMTs at the ends of a bar. The geometric mean of the two signals was used to determine the energy of the particle (refer to eq. (5.10). However, the geometric mean is not proportional to the energy of charged particles but the intensity of the light output. Fox et al. measured the response of plastic detectors for a wide range of incident particles and energies [55]. The response function is

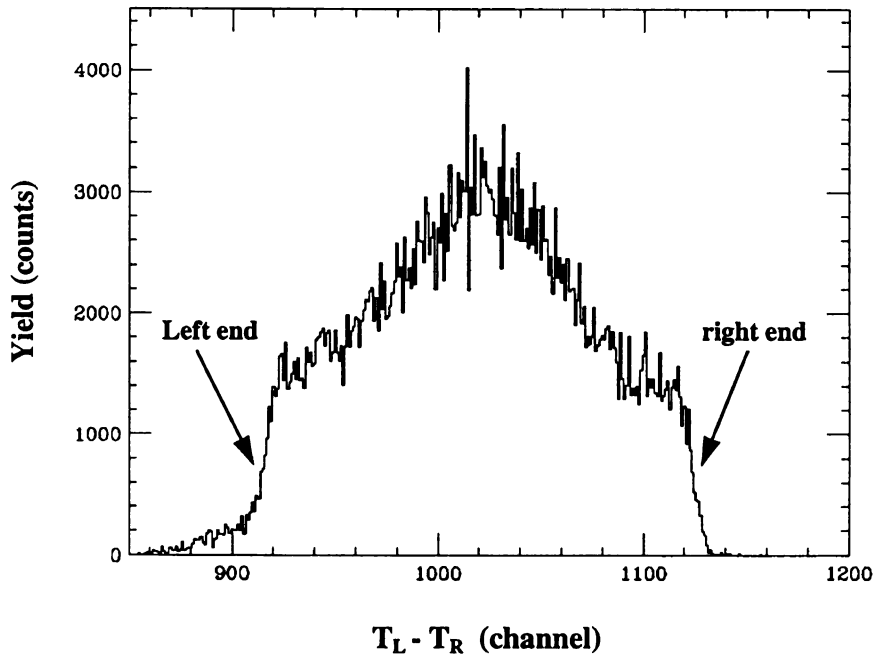

Figure A. 2 The position distribution of cell #1 of the front neutron wall. The two edges give the calibration points for the position of the cell.

$$L = S \bullet E - S \bullet kB \bullet \int_0^{T_0/a} \frac{\frac{dE}{dx}}{1 - kB\frac{dE}{dx}} dE - S \bullet \frac{kB}{2} \bullet \int_{T_0/a}^{E} \frac{(1+R)^2 \frac{dE}{dx}}{2 + kB(1+R)\frac{dE}{dx}} dE \qquad \text{(A.6)}$$

where $R = \ln\left(\frac{T_0}{I}\right) \Big/ \ln\left(\frac{a}{I} \bullet \frac{E}{A}\right)$. The fixed parameters are E—particle energy, $\frac{dE}{dx}$—energy loss, $a = \frac{4m_e}{m_0}$—nucleon rest mass, and I—ionization potential of the scintillator(≈ 0.048 keV for plastic scintillator). The free parameters are S—gain factor of the device, kB—quenching factor, and T_0—the electron kinetic energy cutoff. The three free parameters determined in the paper were used in the response function to convert fragment energy (in unit of MeV) to light output (in unit of MeVee) and vice verse. The scintillator bars were calibrated with two ^{4}He beams at 100 MeV and 80 MeV, and the 4.44-MeV γ ray from a Pb-Be source available at the NSCL. The two ^{4}He beams were chosen in such a way that most of the ^{4}He fragments in the experiment fell into the energy range given by the two beams. After losing energy in the Si detectors, the energies of two ^{4}He beams were reduced to 96.01 MeV and 75.3 MeV, respectively. The light outputs for the three calibration sources are 49.5 MeVee, 35.2 MeVee and 2.38 MeVee respectively. Fig. A.3 shows the light outputs of the three light sources versus the measured geometric means for bar #1. The slope gives the conversion factor. When a ^{4}He fragment detected, its geometric mean is converted into light output. Then, from eq. (5.10), the energy of the ^{4}He is determined.

With the field of the magnet set at the maximum, the 96.01 MeV ^{4}He could only reach bar #10, not the bars from bar #11 to #16. The field of the magnet was reduced for

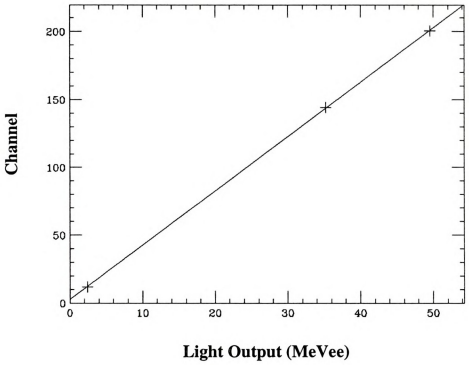

Figure A. 3 The energy calibration of scintillator bar #1. The three calibration points in the graph are from 2.61 MeV γ ray of a Pb-Be source, 80 MeV and 100 MeV ^{4}He beams, respectively.

the beam to reach the bars from bar #1 to bar #9. Calibration was done for the 10 bars with the three calibration sources. In order to calibrate the six bars from bar 11 to bar 16, a 10 MeV/u ^{6}Li beam was chosen to inter-calibrate the scintillator bars. The gains of the the six bars were matched to that of bar #1. To calculate the light output of fragment in these bars, the geometric mean is first scaled to that of bar 1, then the calibration parameters of bar 1 are used for the conversion.

A.2.2. Inter-bar time calibration

The neutron TOF is measured from the time difference between a cell, where a neutron is detected and a scintillator bar, where a fragment is detected. Since the time signals of the 16 scintillator bars were processed by difference channels of electronics, the TOF must be corrected for the time variance between the channels. The inter-bar time calibration was conducted by using a ^{60}Co source. The source was placed at the same position where the Si strip detectors were mounted. Because ^{60}Co emits two γ rays at a time—1.33 MeV and 1.17 MeV, Coincidence between the neutron walls and the individual scintillator bars can be produced. Since the flight time from the source to the bars is almost the same, the difference between the peak positions measures the time variance of the electronics.

A.3. Si Strip Detectors

Fig. 2.7 shows a sketch of the target and the Si strip detectors in the experiment. The two Si strip detectors were placed behind the target to detect charged particles. Each detector consists of 16 horizontal strips and 16 vertical strips. In principle, when a

charged particle penetrates a strip detector, a signal is picked up by one horizontal strip and one vertical strip. The location of the horizontal strip gives the y position of the particle, thereafter called "y strip", and the location of the vertical strip gives the x position of the particle, thereafter called "x strip". The direction of a charged particle is then determined from the measured x and y coordinates. One problem with the strip detectors is that there is cross talk between the neighboring strips. A cross-talk here means that the pulse of electrons generated by a charged particle striking one strip would induce smaller pulses in the neighboring strips. So, the strip that yields the maximum signal was used to determine direction and energy loss of the particle. The amplitude of signals in the cross talk strips was much less than the stricken strip. Another problem was that no. 8 x strip of detector 2 did not work. The cross-talk of the no. 8 with no. 7 and no. 9 x strips was used to determine if there was a charged particle striking no. 8 strip. If there is a particle striking no. 8 strip, a small cross-talk pulse can be found in no.7 and no. 8 strips. A gate is set on the these pulses from no. 7 and no. 9 strips. If an event is found in the gate of the no. 7 strip and in the gate of the no. 8 strip at the same time, the no. 8 x strip must be stricken by a particle.

Energy signals were read out for all the 64 strips of the two detectors. The y strips were used to measure the ΔE of the fragments in the experiment. To calibrate the ΔE of the strips, two ^{4}He beams at 20 MeV/u and 25 MeV/u, and two 9Li beams at the same energies were sent to the Si strip detectors. The energy losses of the beams in the detectors are 4.73 MeV, 3.91 MeV, 10.64 MeV and 8.78 MeV, respectively. In order to ensure that all the strips were stricken by the calibration beams, the last quadrupole in the

N4 vault was turned off so that the defocused beam can cover all the strips vertically. A steering dipole magnet in the beamline was adjusted to sweep the strip detectors horizontally. In this way, calibration on every y strip was conducted. The calibration for the no. 1 y strip of detector #1 is shown in Fig. A.4.

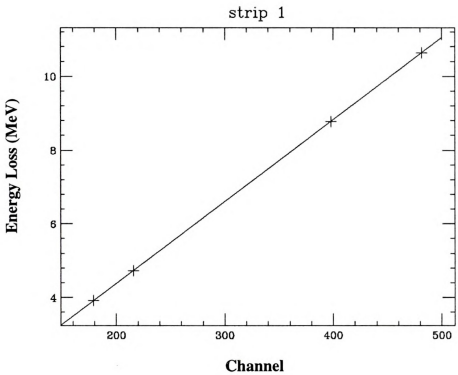

Figure A. 4 The energy calibration of strip #1 of Si detector #1. The four data points are from 20 MeV/u and 25 MeV/u ^{4}He, 20 MeV/u and 25 MeV/u ^{9}Li beams, respectively.

Appendix B: Electronics and Data Acquisition

B.1. Neutron Wall Electronics

All the information about a detected neutron is contained in the two electronic signals from the two PMTs at the ends of a cell. One signal is a positive pulse extracted from the last dynode and the other signal is a negative pulse from the anode. The schematics of the electronics for the neutron walls are shown in Fig. A.5. The dynode signal is inverted to a negative signal before it is sent into a constant fraction discriminator(CFD). The threshold of the CFD was set at 1 MeVee. The CFD generates a logic signal for the signals with pulse height greater than the threshold. The logic signal is split into three. (1) One is put into a Time-to-FERA converter (TFC) as an individual start. All the TFCs are stopped by the delayed OR logic between the fragment master signal and the neutron wall master signal. The output of each TFC is then digitized by a FERA (Fast Encoding and Readout ADC). Only those channels corresponding to the fired PMTs are read out. The measured time from the PMTs is used to obtain neutron's TOF and position. (2) One is sent to a scaler. (3) The third one is send to form a logic OR with the outputs of the other CFDs. The logic OR creates a gate signal for the FERAs and a trigger signal for the trigger logic to control the data acquisition system. The anode signal is put into the NSCL PSD circuit. There are four outputs from the circuit---"Fast", "Total", "Attenuated Fast" and "Attenuated Total", described in the n-γ discrimination section. "Total" and "Attenuated Total" were measured by FERAs, whereas "Fast" and "Attenuated Fast" were measured with ADC's due to the limited

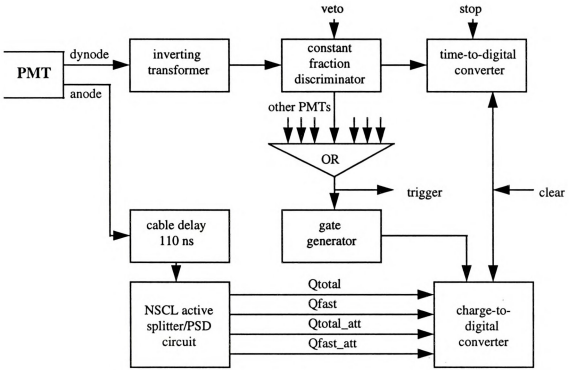

Figure B. 1 Schematics of the neutron wall electronics.

number of FERAs available in the lab. "Attenuated Total" is also used to determine the energy of the recoil proton involved in neutron detection. The energy of the recoil proton is needed to perform cross-talk identification (refer to Part II of the thesis).

B.2. Fragment Detector Electronics

The two signals from a PMT on a scintillator bar was handled the same way as those from a PMT on a scintillator cell of the neutron walls except that there is no n-γ discrimination circuit. It is not necessary for a n-γ discrimination because the light produced by the fragments are much greater than those produced by γ rays. The anode signal was directly processed by an ADC.

The schematics of the electronics for the Si strip detectors are shown in Fig. A.6. The signals from horizontal and vertical strips were sent to a preamplifier built for the S800 spectrometer at the NSCL. As shown in the figure, the horizontal signals are only processed by the quad shapers for their pulse height. The pulse height was measured by a Philip ADC. The vertical signals were put to a quad shaper made at MSU. The slow output of the quad shaper was used for the pulse height measurement, and the fast output was sent to a CFD for timing.

B.3. Trigger Logic

B.3.1. Fragment Trigger

The fragment trigger logic is shown in Fig. A.7. The scintillator master signal is created by the OR of the CFDs for the 16 scintillator bars. The OR signal is used for

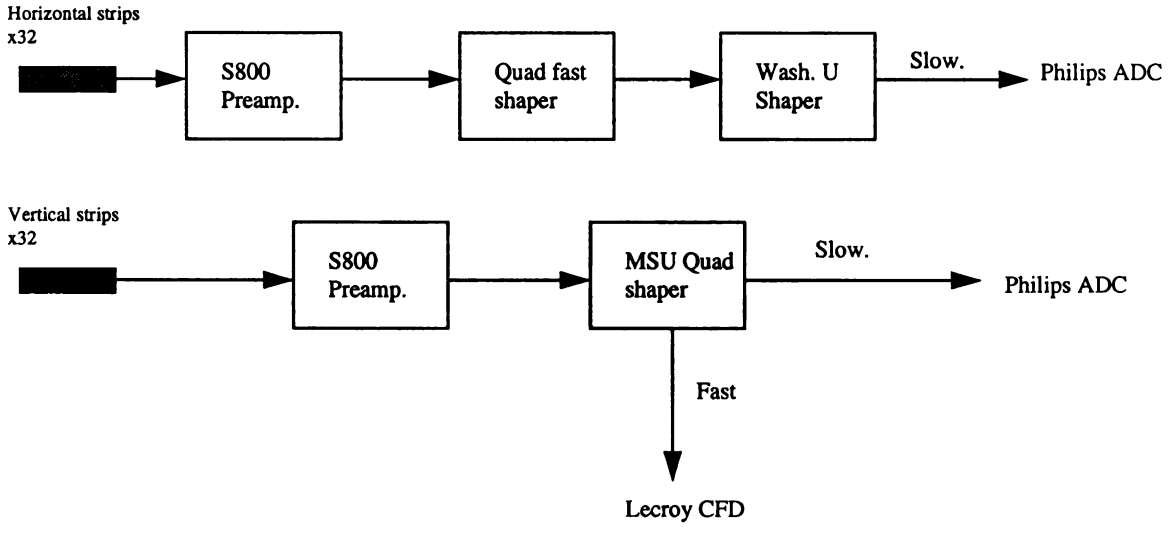

Figure B. 2 Schematics for the Si strip detector electronics.

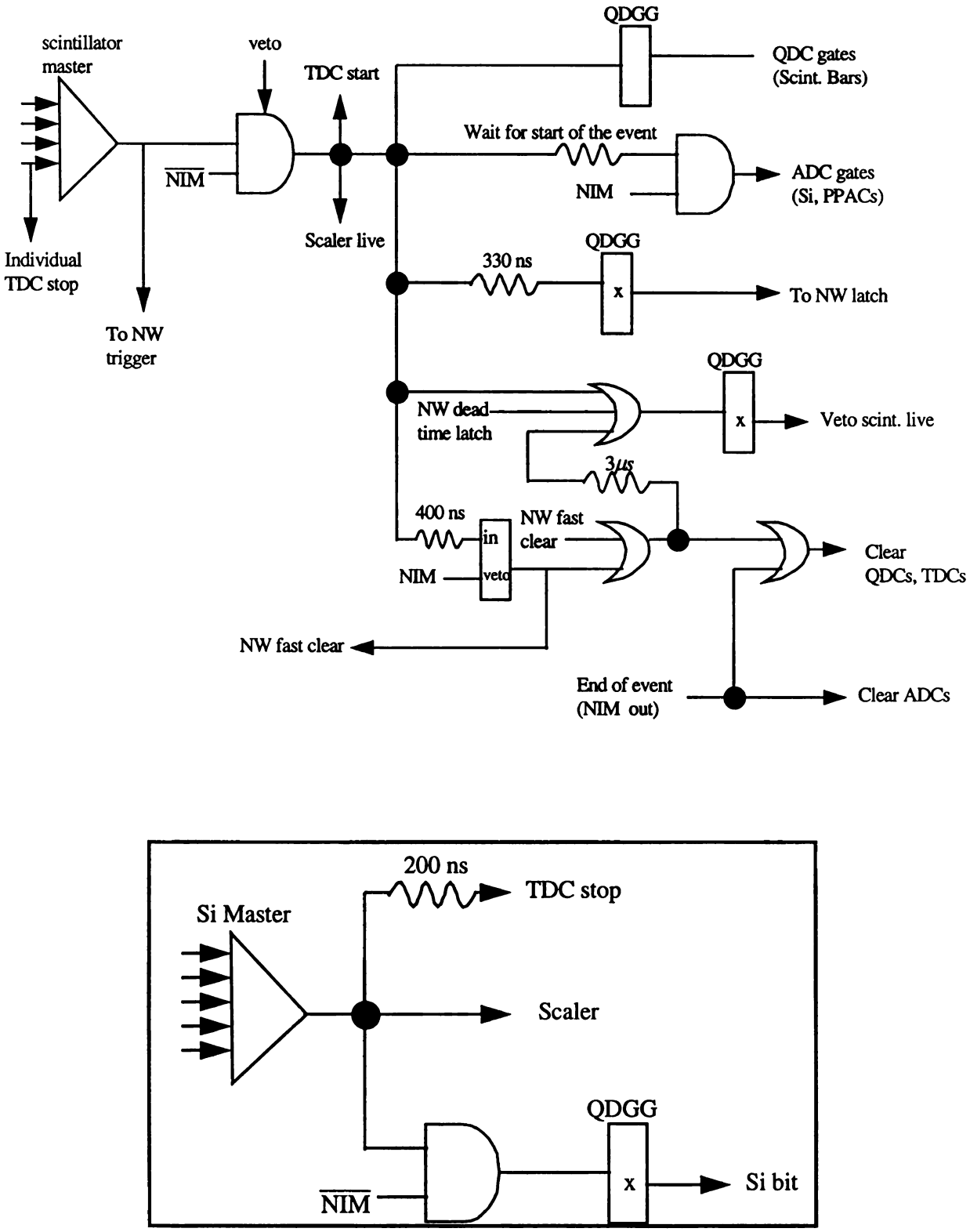

Figure B. 3 The fragment trigger logic. The scintillator trigger logic is on the top. The Si trigger is in the box on the bottom.

master trigger, which will be described later. It is also used to make the scintillator master live signal after an AND operation with a computer not busy signal ($\overline{NIM}$). The master live signal is used for the following logic: (1) It is processed by a quad delayed gate generate(QDGG) to produce a gate for the QDCs of the scintillator bars. (2) It creates a gate for the Si detectors. (3) It starts the TDCs for the scintillator bars. The TDCs are stopped by individual PMTs on the bars. (4) It is delayed 330 ns to latch the neutron walls so that the neutron walls won't be disturbed by an event coming shortly after the previous event. We used 330 ns to ensure enough time is left for the neutrons, produced with the charged fragment, to reach and fire the neutron walls. (5) The OR logic between the master live, the neutron wall dead time signal and the delayed clear signal is used to veto scintillator live so it is also not disturbed when an event is processed. (6) If the computer is still doing nothing after 400 ns, the master live clears all the electronic modules (QDC, TDC, etc.) and wait for the next event to come.

The Si master signal is produced by the OR of the 32 vertical strips. After delayed 200 ns, it serves as the TDC stop. The TDC is started by the neutron wall master signal. The time difference was supposed to measure the neutron TOF. Due to poor time signals, the Si master signal was not used for the measurement. It is sent to a Bit Register (BR) to represent a Si single event. Being a passive bit, the Si master was not used to trigger the data acquisition. Si data were read out whenever a scintillator bar was fired.

B.3.2. Master Trigger Logic

The logic of the master trigger for the experiment is very similar to the one described in [56]. In an experiment like this, we measure three types of events. The first

type is neutron wall singles events in which only the neutron walls are fired. The second type is fragment singles events in which only the scintillator array is fired. The third type is coincidence events in which both the neutron walls and the scintillator array are fired within 250 ns. The coincidence period is chosen so that the slowest neutrons can reach the neutron walls. The three types of events are represented by three bit—bits 1, 2 and 3 in the Bit Register. So computer starts reading data whenever a logic signal for one of the three types triggers the data acquisition system. Because the number of singles events overwhelms that of coincidence events, the singles events were downscaled by 500. If a singles event does not pass the downscaler, a fast clear signal is generated to clear all the electronic modules. By doing so, the dead time of the electronics was greatly reduced. Other than the three bits for the three types of events, each scintillator bar uses one bit in the Bit Register so that when a fragment is detected, a computer is directed to read out the data from the scintillator bar, which detects the fragment.

Appendix C: Cross-talk Simualtion Programs

I have written a group of simulation programs for the cross-talk in the neutron walls. All the programs are located under the directory:

USER_LOAN2:[NEUTRON.EFF]

in the computer network at the National Superconducting Cyclotron Laboratory (NSCL). The names of the programs and what they do are given below.

WALLGPN_LI7.FOR	Calculate the $(\cos\theta)_c$-$(\cos\theta)_m$ and $(\Delta T)_c$-$(\Delta T)_m$ distributions of the cross-talk events between the two walls. The neutrons are from the ^{7}Li(p, n) reaction. (Fig.
WALLGTOF_LI7.FOR	Calculate the $(\Delta T)_c$-$(\Delta T)_m$ distribution of the cross-talk events between the two neutron walls and within one wall. The neutrons are from the ^{7}Li(p, n) reaction.
WALLGNN_LI11.FOR	Calculate the $(\cos\theta)_c$-$(\cos\theta)_m$ and $(\Delta T)_c$-$(\Delta T)_m$ distributions of the cross-talk events between the two walls. The neutrons are from the ^{11}Li breakup: $^{11}\text{Li} \rightarrow {}^9\text{Li} + n + n$. The simulation uses the 3-body phase space model.
WALLGTOF_LI11.FOR	Calculate the $(\Delta T)_c$-$(\Delta T)_m$ distribution of cross-talk events between the two neutron walls and within one wall. The neutrons are from the ^{11}Li breakup: $^{11}\text{Li} \rightarrow {}^9\text{Li} + n + n$. The simulation uses the 3-body phase space model.

All the subroutines used in the four programs are stored in a program called WALLSUB.FOR. To run any one of the four main programs, one has to use a command file and an input file. The input file name is the same for all the programs. It is called WALLGS.INP. The command files has the same names as those of the four main programs except that the extension of the command files is COM, e.g. WALLGNN_LI11.COM. To run program WALLGNN_LI11.FOR, one has to modify WALLGS.INP according to his or her own specifications (beam energy, wall

configuration, etc.), then run WALLGNN_LI11.COM. The input parameters one may want to change are listed below,

1. The positions of the two walls (inches)
2. The threshold for the cells (MeVee)
3. The average decay energy in the 11Li simulations (MeV).
4. Beam energy (MeV)
5. Time of Flight resolution (ns)
6. Fragment energy resolution (%)
7. Attenuation length in the scintillator (inches)
8. The gates for cross-talk identification. (Refer to Fig. 5.3.5)

These input parameters can be easily located in the file WALLGS.INP because they are labeled. The outputs of the programs are the simulation results shown in Fig. 5.3.5 and Fig. 5.4.3. The programs can be adapted to do cross-talk simulations for any neutron source and for any neutron detector configuration. Sally Gaff at the NSCL has successfully adapted the programs for her thesis experiment. I would like to say, Good Luck, to anyone who likes to explore the programs.

Bibliography

[1] I. Tanihata et al., Physics Letters B160 (1985) 380

[2] I. Tanihata et al., Physics Review Letters 55 (1985) 2676

[3] T. Kobayashi et al., Physics Review Letters 60 (1988) 2599

[4] P.G. Hansen et al., Europhys. Lett. 4(4) (1987)

[5] I. Tanihata et al., Nuclear Physics A478 (1988) 795c

[6] I. Tanihata et al., Nuclear Physics A522 (1991) 275c

[7] T. Kobayashi et al., Physics Letters B232 (1989) 51

[8] T. Kobayashi et al., Proc. 1st Int. Conf. on Radioactive Nuclear Beam (1989) 325

[9] T. Kobayashi et al., Nuclear Physics A553 (1993) 465c

[10] D. Sackett et al., Physics Review C48 (1993) 118

[11] M.V. Zhukov Physics Reports 231 (1993) 151

[12] F. Ajzenberg-Selove Nuclear Physics A490 (1988) 1

[13] A. A. Korsheninnikov, T. Kobayashi, Nuclear Physics A567 (1994) 97

[14] L.V. Chulkov et al., Physics Review Letters (1997) 201

[15] T. Kobayashi et al., Nuclear Physics A538 (1992) 343c

[16] D.P. Balamuth et al., Physics Review Letters 72 (1994) 2355

[17] R. E. Warner et al., Physical Review C54 (1996) 1700

[18] C.A. Bertulani et al., Nuclear Physics A480 (1988) 615

[19] Y. Suzuki, Physics Review C38 (1988) 410

[20] Y. Suzuki, Physics Review C41 (1990) 736

[21] Y. Suzuki, Nuclear Physics A528 (1991) 395

[22] K. Ikeda et al., Nuclear Physics A538 (1992) 355c

[23] B.V. Danilin et al., Radioactive Nuclear Beam 1991: section 3 186

[24] M.V. Zhukov et al., Radioactive Nuclear Beam 1991: section 3 192

[25] B.V. Danilin et al., Physics Letters B302 (1993) 129

[26] A. Csoto et al., Physics Review C48 (1993) 165

[27] Y. Suzuki et al., Nuclear Physics A567 (1994) 957

[28] S. Funada et al., Nuclear Physics A575 (1994) 93

[29] Y. Skuragi et al., Nuclear Physics A588 (1995) 65c

[30] L. S. Ferreira et al., Physics Letters B316 (1993) 23

[31] C.A. Bertulani et al., Physics Reports 163 (1988) 299

[32] P.D. Zecher et al., Nucl. Instr. and Meth. A401 (1997) 329

[33] Burle, Photomultiplier Handbook, 1980

[34] Hamamatsu, Photomultiplier Tubes

[35] R. E. Warner et al., Physical Review C 55 (1997) 298

[36] G. Bertsch et al., Physical Review C 42 (1992) 758

[37] Private communication with R. E. Warner, 1998

[38] Glenn F. Knoll, Radiation Detection And Measurement, Second Edition, Chapter 8

[39] I. Tanihata, Physics Letters B 289 (1992) 261-266

[40] F. Barranco et al., Physics Letters B 319 (1993) 387-392

[41] Private communication with F. Barranco

[42] R. Serber, Physics Review 72 (1947) 1008

[43] C.A. Bertulani, Physics Review C 46 (1992) 2638

[44] I. Tanihata et al., Physics Letters B 206 (1988) 592

[45] John M. Blatt and Victor F. Weisskopf, *Theoretical Nuclear Physics*, (1952), page 361

[46] A. Pushkin et al., J. Phys. G: Nucl. Part. Phys. 22 (1996) L95-L98

[47] A. Goldharber, Physics Letters B 53 (1974) 306

[48] L. Lüdemann et al., Nucl. Instr. and Meth. A334 (1993) 495

[49] P. Désesquelles et al., Nucl. Instr. and Meth. A307 (1991) 366

[50] A. V. Kuznetsov et al., Nucl. Instr. and Meth. A346 (1994) 259

[51] M. Cronqvist et al., Nucl. Instr. and Meth. A317 (1992) 273

[52] R. Ghetti et al., Nucl. Instr. and Meth. A317 (1992) 273

[53] V. V. Verbinski et al., Nucl. Instr. and Meth. 65 (1968) 8

[54] R. A. Cecil et al., Nucl. Instr. and Meth. 161 (1979) 439

[55] Fox et al., Nucl. Instr. and Meth. A374 (1996) 63

[56] Thesis by P.D. Zecher, 1996